AEROSOL-BASED ULTRAFINE MATERIAL DEPOSITION FOR MICROELECTRONICS

A Dissertation
Submitted to the Graduate Faculty
of the
North Dakota State University
of Agriculture and Applied Science

By

Justin Michael Hoey

In Partial Fulfillment of the Requirements
for the Degree of
DOCTOR OF PHILOSOPHY

Major Department:
Mechanical Engineering and Applied Mechanics

October 2012

Fargo, North Dakota

North Dakota State University

Graduate School

Title

Aerosol-Based Ultrafine Material

Deposition for Microelectronics

By

Justin Michael Hoey

The Supervisory Committee certifies that this disquisition complies with North Dakota State University's regulations and meets the accepted standards for the degree of

DOCTOR OF PHILOSOPHY

SUPERVISORY COMMITTEE:

Dr. Iskander Akhatov
Chair

Dr. Zakaria Mahmud

Dr. Fardad Azarmi

Dr. Orven Swenson

Approved:

11/7/2012
Date

Dr. Alan Kallmeyer
Department Chair

ABSTRACT

Aerosol-based direct-write refers to the additive process of printing CAD/CAM features from an apparatus which creates a liquid or solid aerosol beam. Direct-write technologies are poised to become useful tools in the microelectronics industry for rapid prototyping of components such as interconnects, sensors and thin film transistors (TFTs), with new applications for aerosol direct-write being rapidly conceived. This research aims to review direct-write technologies, with an emphasis on aerosol based systems. The different currently available state-of-the-art systems such as Aerosol Jet™ CAB-DW™, MCS and aerodynamic lenses are described. A review and analysis of the physics behind the fluid-particle interactions including Stokes and Saffman force, experimental observations and how a full understanding of theory and experiments can lead to new technology such as nozzle designs are presented. Finally, the applications of aerosol direct-write for microelectronics are discussed in detail including the printing of RFID antennas, contacts and active material for TFTs, the top metallization layer for solar cells, and interconnects for circuitry.

ACKNOWLEDGMENTS

First, I would like to thank my lead advisor, Dr. Iskander Akhatov, for his motivation and patience throughout this process. I am also thankful for my committee members Dr. Orven Swenson, Dr. Zakaria Mahmud, and Dr. Fardad Azarmi. In addition, this research would not be possible without the support of the Vice President for Research Creative Activities and Technology Transfer, Dr. Phil Boudjouk, CNSE Director Mark Lande and Associate Director Aaron Reinholz. The assistance and support from Dr. Doug Schulz and Dr. Larry Pederson are also recognized.

This work was done in conjunction with my colleagues who also defended topics which I discuss in this paper, I would like to thank those colleagues in our past and present aerosol research team: Jacob Fink, Artur Lutfurakhmanov, Mike Robinson, and Sourin Bhattacharya. Assistance from the following people is also gratefully acknowledged: Dr. Wayne Reitz, Dr. Douglas Chrisey, Eric Jarabek, Shane Stafslien, Shannon Viestenz, Dr. Andrei Vedernikov, Aaron Halvorsen, Dustin Vaselaar, Kris Braaten, Mike Maassel, Mike Reich, Osman Ghandour, Paul Drzaic, Dr. Valery Marinov, Adeyl Khan, Bob Gilbertson, Drew Thompson, Matthew Robinson, Jason Daugs, Dr. Greg McCarthy, Dr. Sijin Han, Dr. Xuliang Dai, Scott Payne, Rob Sailer, Matthew Page, and Dr. Qi Wang. Without their assistance and others whom I could have forgotten, this work would not be possible.

Last and most importantly, I want to thank my wife, Kim; and daughters, Elise, Lauren, and Sophia, for always being there. My wife has as much patience as anyone could ever have, and her support and love are never forgotten. They have stuck by me even when I am not home to be there. The past seven years' work has been difficult at times with late nights and early mornings, but in the end it has been worth it.

This work was based on research sponsored by the Defense Microelectronics Activity (DMEA) and the Department of Energy (DOE) under Agreement Numbers H94003-11-2-1102, and DE-FG36-08GO88160, respectively. The views and conclusions contained herein are those of the author and should not be interpreted as necessarily representing the official policies or endorsements, either expressed or implied of the Defense Microelectronics Activity or Department of Energy.

TABLE OF CONTENTS

LIST OF TABLES

LIST OF FIGURES

LIST OF SYMBOLS

a	Particle radius
A, A', B, E	Constants for Cunningham Correction
C_D	Drag coefficient
C_g	Speed of sound of the fluid
C_L	Coefficient of lift
C_{LSaf}	Coefficient of lift due to Saffman force
c_M	Added mass coefficient
d, D	Diameter
$\vec{e}_x, \vec{e}_r, e_y$	Direction vectors in the axial and radial direction
F	Force acting on particle
F_{Ba}	Basset force
F_{Gr}	Buoyancy force
F_L	Lift force
F_{Ma}	Magnus force
F_{Ps}	Pressure gradient force
F_{sa}	Saffman force
F_{St}	Stokes force
$F_{StokesCc}$	Stokes force w/ Cunningham correction
F_{Vm}	Virtual mass force
$\mathbf{g}$	Gravity acceleration vector
G	Stokes correction coefficient

h	Film thickness
H	Saffman force correction coefficient
K	Dimensionless parameter
Kn, Kn_p	Particle Knudsen number
L	Length of the nozzle, characteristic length
M_p	Particle mach number
Oh	Ohnesorge Number
m, m_p	Mass of particle
Q	Volume flow rate
r	Radial position of the particle
R	Outer radius of the nozzle
R_o	Initial radius of the nozzle
R_g	Specific gas constant
Re_f	Reynolds number of the fluid
Re_p	Reynolds number of the particle relative to the fluid
Re_Ω	Particle rotational Reynolds number
St	Stokes number
t	Time
U	Average velocity
u, u_p	Instantaneous x-velocity of the fluid and particle respectively
u_{max}	Maximum initial velocity (at the centerline) of the fluid
v, v_p	Instantaneous r-velocity of the fluid and particle respectively

$\mathbf{v}_p$	Instantaneous vector velocity of the particle
We	Weber number
x	Axial position of particle
α	Coefficient for Reynolds number
α_{Sa}	Saffman coefficient
ΔP	Change in pressure
ε	Ratio of Reynolds numbers
ε_{Ba}	Ratio of Basset force to Stokes force
ε_{Ma}	Ratio of Magnus force to Stokes force
ε_{Sa}	Ratio of Saffman force to Stokes force
μ_f	Dynamic viscosity of the fluid
v	Kinematic viscosity
ρ_f	Density of the fluid
ρ_p	Density of the particle
σ	Surface tension
τ	Time coefficient
τ_l	Particle coupling parameter
τ_μ	Stokes relaxation time
ω	Fluid vorticity
Ω	Particle angular velocity

1. INTRODUCTION

This dissertation is a compilation of the work of several people over the past seven years. Dr. Iskander Akhatov is the lead advisor for this project, with Dr. Orven Swenson and Dr. Zakaria Mahmud as co-advisors. At CNSE, Dr. Doug Schulz was my supervisor for the projects until January 2012. The results presented in this dissertation started from the work completed previously in my master's thesis where the first aerosol beam width measurements and analytical model for aerosol particles were determined. CAB-DW was discovered at this point, but was not included in my thesis. I had help from several other people for both the theoretical and experimental sections after the initial experiments with CAB-DW. The main sections of this work are summarized in Figure 1 below. Jacob Fink was responsible for printing top contacts on solar cells. Artur Lutfurakhmanov was responsible for the refinement of aerosol modeling and obtaining theoretical beam width measurements. Mike Robinson was responsible for the small particle sizing algorithm and experimental measurements of aerosol beam widths using both laser scattering and shadowgraphy. Sourin Bhattacharya was responsible for theoretical modeling of the micro cold spray system and preliminary experimental results printing with this tool. I was responsible for coordinating this effort and worked daily with everyone involved to ensure that the correct work was being performed. Much of the printing results for transistors, solar cells, RFID tags, and interconnects was accomplished by me, or under my direction.

Direct-write printing is an additive technology used to controllably deposit features onto samples in patterns defined by computer-aided design / computer-aided manufacturing (CAD/CAM) software allowing rapid prototyping of various geometries without the use of lithography [1, 2]. In 2008, Hon et al. [2] reviewed this field and categorized direct-write into four main categories. The first category is “flow-based direct write” where technologies such as nScript and MicroPen employ a micro-dispensing system with a needle or orifice to continuously deposit features as small as 25 μm at speeds up to 300 mm/s. Flow rates in the nL/s range are typical and flow-based direct write is capable of printing materials with a viscosity from 0.5 to 10^6 cP which allows deposition of a variety of ink compositions.

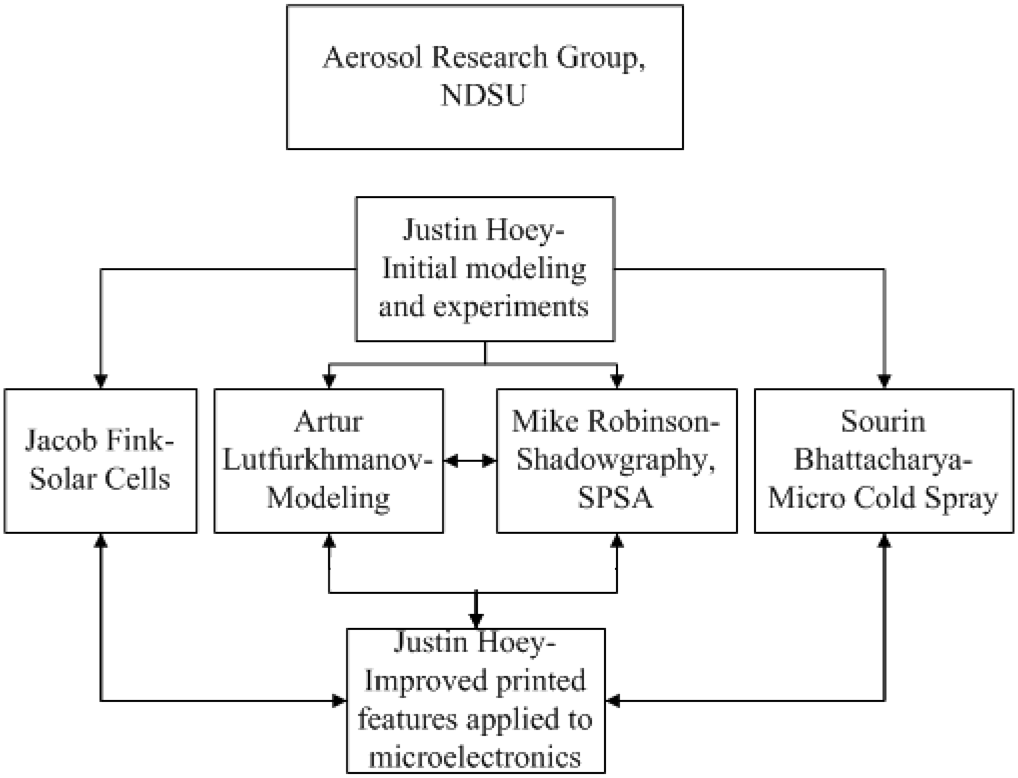

Figure 1. Diagram of Aerosol Research Group graduate student members.

The second category is “energy beam based direct write” and includes several technologies that use high-power lasers to transform and/or propel material onto a substrate. The laser-based systems include laser enhanced electroless plating (LEEP), matrix-assisted pulsed laser evaporation- direct write (MAPLE-DW), laser engineered net shaping (LENS) [3], laser-guided direct write (LGDW) [4], and Mesoscribe™ Technologies [5]. While the details for all of these approaches is beyond the scope of this review, as an example, we briefly describe MAPLE-DW which is a process that uses a pulsed UV laser to forward transfer a thin film of material from a transparent "ribbon" to a substrate. Interaction of the laser with the solvent component of the "ribbon" causes rapid evaporation whereby the irradiated portion is ejected from the ribbon and transported ~100 μm where it is deposited onto the substrate [1]. The areal dimension of the deposit is similar in size to laser area with a common diameter around 30 μm [6]. Film thicknesses from 1 to 20 μm are commonly observed when ribbons ~25 μm are employed [1]. This process requires specialized inks that have appropriate viscosity and UV absorption. Minimum resolution of the as-deposited lines are limited by the laser spot size but printed features with line widths down to 2 μm can be realized by laser-trimming the patterns [6]. Included in this category are also non-laser based approaches such as focused ion beam (FIB) direct-write. This method uses gallium ion bombardment with precursor gases to deposit features as small as 80 nm at volumetric print rates of 0.05 $\mu m^3/s$ [2].

"Tip-based direct write" is the third category and includes dip pen nanolithography (DPN), nano-fountain pen (NFP) and capillary-based liquid micro-droplet deposition [7]. DPN utilizes an atomic force microscope (AFM) tip to deposit films onto a substrate. After the AFM probe is dipped in a liquid, the tip is brought into contact with the substrate where the liquid flows onto the substrate as the AFM moves in a desired pattern with nanoscale resolution. NFP is a variation of DPN where liquid is dispensed through a hollow tip which is in contact with the substrate. This method has been scaled to multiple tips (up to 12) while stilling maintaining sub-100 nm resolution. Capillary-based liquid micro-droplet deposition was recently developed where the application of pressure into a capillary causes a liquid meniscus to form at the outlet [7]. Touching the substrate with the liquid meniscus (not the capillary) and subsequent capillary retraction gives liquid deposition on the substrate where the size of the deposit may be as small as 10% of the capillary inner diameter with dimensions as small as 32 μm observed for a 300 μm capillary. Substitution of a nano-capillary for the micro-capillary in this approach should allow nano-droplet features that maintain a resolution similar to that already demonstrated by DPN and NFP.

The fourth category is termed “droplet-based direct write”. Perhaps the most widely investigated droplet-based DW method is ink-jet where thermal, piezoelectric, hydrodynamic, electrostatic and acoustic energies produce small droplets of liquid that are ejected from a nozzle. Both continuous inkjet (CIJ) and drop-on-demand (DOD) versions are available. Resolution down to <20 μm has been realized with ink-jet and the non-contact approach is scalable (hundreds to thousands of nozzles in a single head) for high-throughput operations. Ink-jet is very sensitive to the characteristics of the printing ink because only a limited viscosity range is atomizable, and nozzles can become easily clogged if the ink is too volatile, but certain volatility is required for correct drying once the ink is deposited. The nozzle to substrate distance must be precisely controlled which complicated printing over non-planar substrates [2].

Aerosol based direct-write (A-DW) is a subset of droplet-based direct write. Two such methods that employ liquid feed are Aerosol Jet^{TM} and CAB-DW^{TM} (collimated aerosol beam-direct write) and were developed by Optomec and North Dakota State University (NDSU), respectively [8, 9]. Aerosol Jet and CAB-DW use a focused aerosol spray to deposit material with sub-10 μm resolution. An aerosol may be defined as a suspension of fine liquid or solid particles in a gas. One method that employs a solid feed is micro-cold spray (MCS) where ductile metal particles of material are accelerated to near or above sonic velocities through a focusing nozzle and deposited onto a substrate [10, 11]. MCS is similar to Aerosol Jet and CAB-DW but the deposited lines exhibit conductivities near the bulk value without a post-deposition thermal treatment. The previous techniques worked well for mesoscopic particles but are not designed for nanoparticles. A focusing technique developed by researchers at the University of Minnesota uses a set of aerodynamic lenses under vacuum conditions to focus nanocrystal agglomerates and deposit them on a substrate [12-15]. Examples of this technique for direct-write applications such as for microelectromechanical systems (MEMS) are minimal, but depositions of traces as small as 35 μm wide were reported.

2. AEROSOL PRINT TECHNOLOGY

2.1. Aerosol Jet – Single Nozzle with Liquid Aerosol

Aerosol direct-write is a process where an aerosol beam is concentrated and directed toward a substrate to produce desired surface features (e.g., dots or lines) without using masks or post-patterning (i.e., laser trimming). Aerosol spray has been used for decades by the paint industry for thin and thick coatings. The ability to focus the aerosol spray to small (<100 μm) dimensions gives beams of material and substantiates the term direct-write. The first A-DW method to be introduced to the community was Aerosol Jet^{TM}. Aerosol Jet was formerly referred to as M^{3}D (maskless mesoscale materials deposition) and was developed by Optomec [16] under the Defense Advanced Research Projects Agency (DARPA) Mesoscopic Integrated Conformal Electronics (MICE) program. The commercially available system is designed to print traces from 10 μm to 5 mm in width at translation speeds up to 200 mm/s. Liquid ink viscosities between 0.5 and 2500 cP are typically employed. The deposition of materials using Aerosol Jet is illustrated in Figure 2.

The deposition process begins with atomization of a precursor liquid ink into 1 to 5 μm diameter droplets with either an ultrasonic (commonly 1.6 – 2.4 MHz) or pneumatic atomizer. These droplets are then entrained in a carrier gas and transported to a deposition head where an annular flow of sheath gas is added. The sheath gas indirectly acts as a focusing mechanism by occupying the outer portion of the flow tube. This causes the aerosol to be limited to the center of the flow in a manner that is proportional to the volume the sheath gas. If a pneumatic atomizer is used, a virtual impactor is placed immediately before the deposition head. This device concentrates the aerosol by removing excess gas flow, and decreases the polydispersity of the aerosol by removing very small (<1 µm) particles.

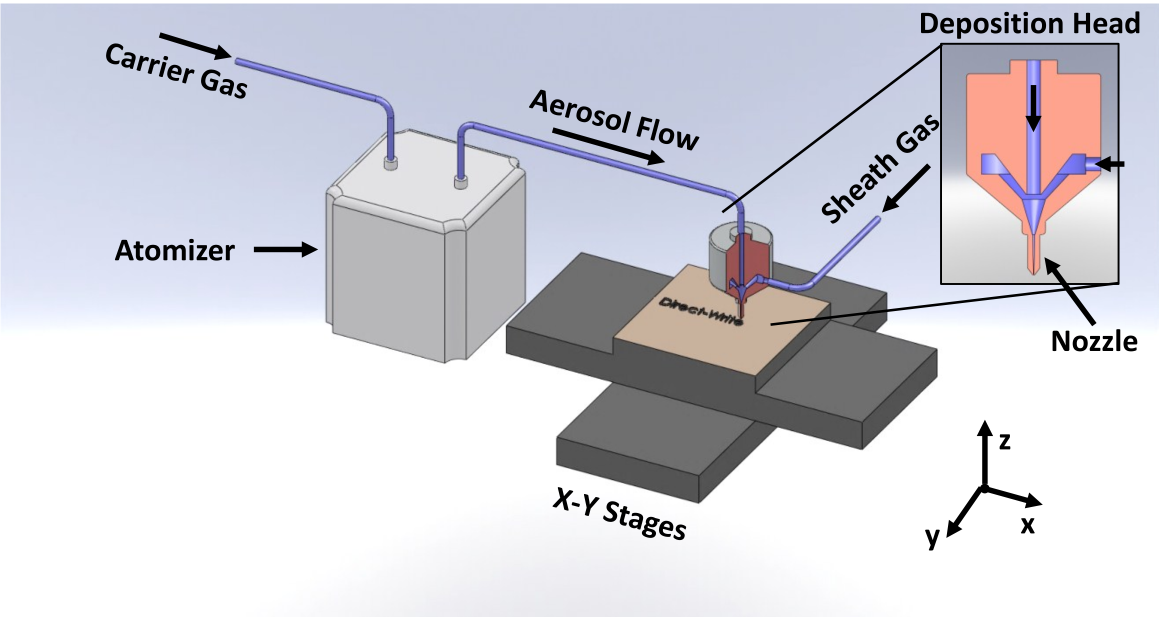

Figure 2. Diagram of Aerosol Jet system, reprinted from Hoey et al. [17].

After the deposition head, the aerosol is further focused inside a converging nozzle about 2 cm long with an exit diameter between 50 and 300 µm. The delivery process is continuous in that the aerosol and gas flow are not cycled on/off when deposition requires termination (e.g., at the end of a line). Rather, a shutter arm blocks the aerosol flow while the substrate is translated to the next prescribed location as per the CAD/CAM program. The aerosol exits the nozzle at a velocity of 10 to 100 m/s and impacts a sample while maintaining a nozzle-to-substrate (stand-off) distance of 1 to 5 mm. This large range of stand-off distance simplifies printing over irregular substrates or other device components such as interlayer dielectrics. A 40-nozzle Aerosol Jet system is now available for parallel processing where the top metallization layer on 15× 15 cm^2 solar cells can be printed in less than three seconds [2]. Aerosol Jet is capable of producing high quality features, but yet requires some effort to remove excess overspray and to preclude nozzle clogging.

2.2. Aerodynamic Lenses with Liquid Aerosol

A new A-DW system designed for printing nanoparticles which uses aerodynamic lens for focusing was developed by Qi et al [15]. The deposition process of this system, represented schematically in Figure 3, begins with the pneumatic atomization of a suspension of CdSe/ZnS core/shell nanocrystals in hexane. The aerosol is focused through aerodynamic lenses and directed into an evacuated chamber and onto a substrate that is translated with an x-y stage. Microtowers and microlines 158 µm tall by 27 µm wide and 2.9 µm tall by 7 µm wide were deposited onto sapphire, glass and silicon substrates with examples shown in Figure 4.

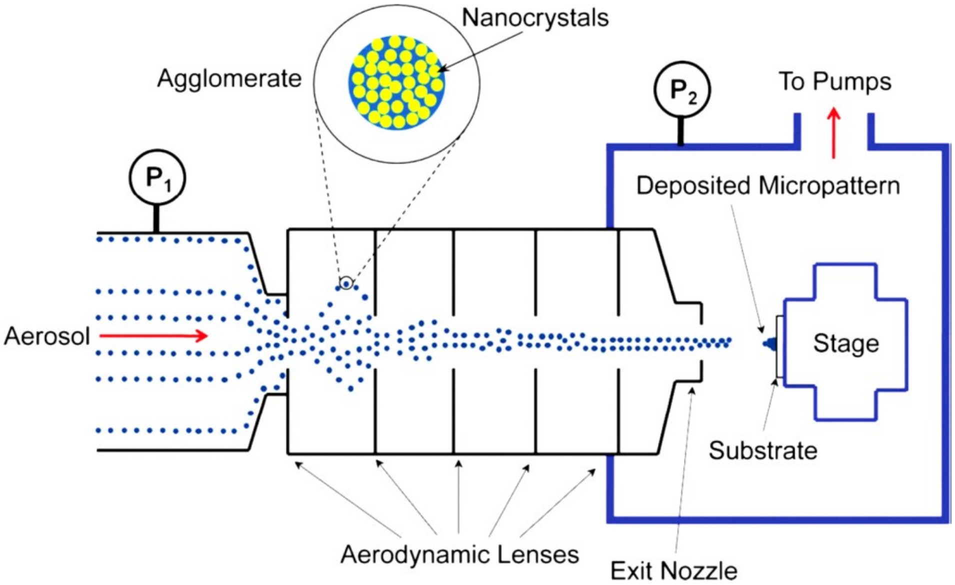

Figure 3. Schematic of A-DW focused particle beam deposition system, from Qi et al. [15], Aerosol Science and Technology, Copyright 2010, Mount Laurel, NJ. Reprinted with permission.

The microlines were printed at a translation speed of 10 μm/s, much lower than Aerosol Jet and CAB-DW, but this system may still be valuable because unlike Aerosol Jet and CAB-DW, nanoparticles can be successfully focused. In addition, the system is reliable and inexpensive using standard aerosol lenses without the need for a sheath gas. The system however will have challenges in commercialization due to the low deposition rate and that printing is required to be performed in an evacuated system. Such evacuated systems are however commonly used in microelectronics fabrication [15].

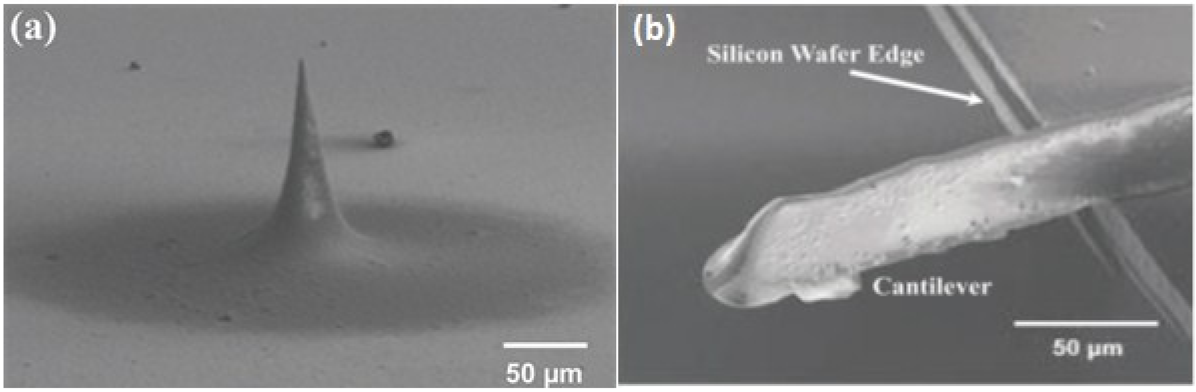

Figure 4. SEM image of CdSe/ZnS core/shell nanocrystal based features printed using aerodynamic lenses; a) microtower, b) microline, from Qi et al. [15], Aerosol Science and Technology, Copyright 2010, Mount Laurel, NJ. Reprinted with permission.

2.3. Atomization Methods

One major challenge with any aerosol print system is the atomization process. Although it may be easy to atomize many materials, the process of focusing aerosol particles for A-DW requires a monodisperse aerosol with uniform properties over long periods of time for good print quality. The ultrasonic techniques mentioned previously for A-DW applications produce a relatively mono-disperse aerosol, but have a limited ability to atomize viscous materials, and suffer from long-term changes in atomization due to factors such as ink drying, and heat. Other manufacturers such as Sono-Tek [18] and Sonaer Ultrasonics [19] have developed ultrasonic horn aerosol generators which are capable of creating aerosol particles with mean droplet diameter as small as 13 µm and 11.8 µm, respectively, but have a Gaussian droplet size distribution. Sono-Tek's atomization system was even developed into an A-DW system using their atomizer termed MicroMist™ which is able to spray features as thin as 400 µm when coupled to a precision translation system [18]. Tsai et al [20] developed a Fourier horn atomizer built from silicon which is capable of producing near-monodisperse particles with a droplet diameter of 7.0 µm. Ju et al[21] and Qi et al [22] describe a surface acoustic wave (SAW) atomizer capable of producing micron-sized droplets similar to what is required for direct-write applications. More detail into the physics behind these atomizers is beyond the scope of this paper but has been reviewed by Friend and Yeo [23]. Overcoming challenges related to any atomization process are still ongoing, with future developments of more monodisperse aerosol generation techniques poised to greatly impact all A-DW processes.

2.4. Materials for Atomization

For any A-DW technology, the printing materials are of great importance. For MCS micron-sized powder is sufficient. For Aerosol Jet, and CAB-DW the deposition materials are slightly more complicated. The inks must be atomizable, and provide necessary print characteristics such as minimal overspray, good substrate adhesion, and transformable to the desired final characteristics (i.e., low resistivity, continuous, stable) using methods compatible with the substrate. Kim and Han [24] review briefly the attributes required for A-DW inks and some examples of commercial suppliers. Many inks require a high sintering temperature (400 °C) in order to achieve near-bulk conductivity. This temperature is much too high for flexible polymeric substrates which are damaged at temperatures above 150 °C. Some manufacturers produce inks with lower sintering temperatures (<100 °C) for flexible applications while still maintaining a reasonable conductivity. Conductive inks are available commercially through several manufacturers including: Cima Nanotech (St. Paul, Minnesota USA), NanoMas (Endicott, NY USA), UT Dots Inc. (Champaign, IL USA), Applied Nanotech (Austin, TX USA), Novacentrix (Austin, TX USA), Cabot Corporation (Boston, MA USA), Harima Chemicals (Osaka, Japan), Advanced Nano Products (Korea), and P.V. Nanocell (Migdal Ha'Emek, Israel). Many of the inks produced are silver or copper based and are designed for inkjet or screen printing applications but can be reduced with solvents to an appropriate viscosity for A-DW. The correct ink for each application must be selected based on the aforementioned qualities. In many circumstances, the specific ink formulation is determined in a trial-and-error process to develop the best overall printed features which balance print quality against the physical and electrical performance.

2.5. Review of Applications of Aerosol Direct-Write

2.5.1. Printed Passives and Conductive Traces

A-DW technologies are still maturing and the application of these to electronics has not been fully established. There are, however, abundant examples in literature of devices with one to all components being A-DW printed. The ability to print using a non-contact, rapid prototyping tool is especially beneficial in the development phase of technology where the time and costs associated with masks are the limiting factor. In addition, the non-contact high aspect-ratio characteristics possible for features printed with A-DW may prove useful in certain niche markets such as solar cells. All A-DW technologies are capable of printing straight traces which may be amenable for interconnects and vias in simple circuitry. Examples of applications of A-DW are quite prevalent, with advantages of using A-DW (Aerosol Jet specifically) described by King and Renn [25] as follows: firstly, reduced time for product development due to maskless approach; secondly, lower costs associated with mask setup for initial small production runs; and, thirdly, greater material utilization which reduces costs and is more environmentally friendly. They also describe one specific application for 3D interconnects where the large stand-off distance makes it possible to print traces over objects such as an alumina cube as illustrated in Figure 5.

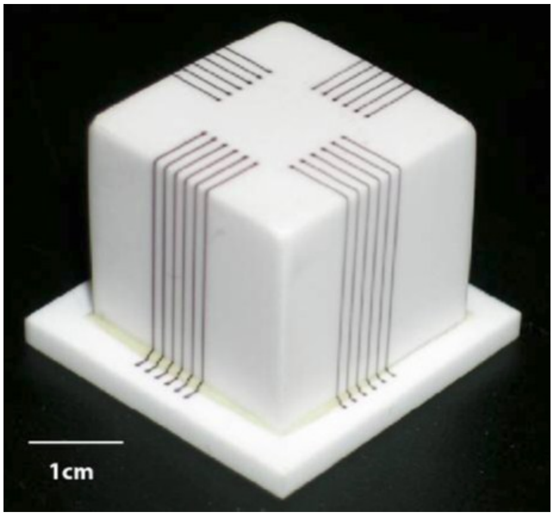

Figure 5. Aerosol Jet printed Ag traces, 150 µm wide, on an alumina cube, from King and Renn [25], Copyright 2009 Optomec. Reprinted with permission.

Aerosol Jet was used to print conducting silver traces on plastic and printed circuit boards (PCBs) for use in an all direct-written chemisensor for the detection of nerve gas

[26]. In this design, a polymer/carbon black composite was spray coated over sets of interdigitated traces on a PCB board. The silver traces were 20 – 50 μm wide, 8 – 10 μm thick and had a conductivity of 4-12 μΩ-cm after sintering at 200 °C. The composite consisted of a swelling co-polymer such as ethylene/vinyl acetate and styrene/butadiene block copolymer with 5-20% carbon black added for increased conductivity. The polymer would swell causing a change in resistivity. The chemisensors can be seen in Figure 6. The sensors were tested with a nerve gas simulant dimethylmethyl phosphonate (DMMP). Results of the test conclude that the sensors do indeed work as intended, are reliable, and prove the viability of direct-written traces for gas chemisensors.

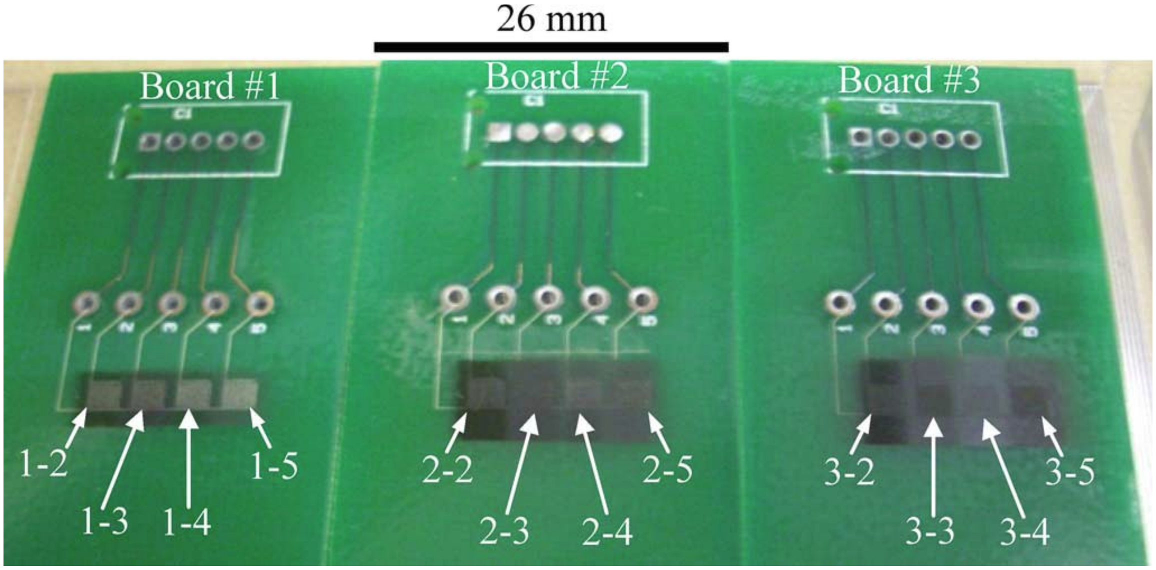

Figure 6. Optical micrograph of all-direct-written chemisensors for the detection of nerve gas, reprinted from Marinov et al. [26], Copyright 2007 IEEE.

Other applications of Aerosol Jet include a technique developed by Marinov et al. [26] who developed what they term Enhanced M^{3}D. This process has two steps, first a trench is laser machined into the substrate; second, a metal ink is direct-written into the trench. This technique may be beneficial for applications especially sensitive to overspray inherent in Aerosol Jet such as for radio frequency identification (RFID) tags because the trench defines the shape of the trace thereby decreasing edge effects and overspray which can be deleterious for high frequency transmission. Silver coplanar waveguides with and without the laser machined trench were prepared to test the improvement in the enhanced approach. Results of the test were promising with dc resistivity decreasing from 9.2 to 4.3 μΩ-cm and AC losses at 6 GHz decreasing from 0.33 dB/mm to 0.02 dB/mm for the waveguide without and with a laser machined trench. These results show that this two-step technique produces results typical to commercial devices where a loss in the range of 0.005 to 0.03 dB/mm is common. Enhanced M^3D is more expensive due to the two-step process, but considering a more than one decade improvement in losses, it may still be viable.

Maiwald et al [27] reported the creation of strain gauges for non-destructive testing using Aerosol Jet. The devices are a multi-layer structure utilizing a printed polymer isolation layer, 2 μm thick, below a silver Aerosol Jet printed strain gauge, with 1 – 3 μm thick traces, and printed encapsulation. The device on an aluminum surface is shown in Figure 7, where the total size of the sensor is only approximately 7 mm × 3 mm. The silver nanoparticle ink used was procured from Advanced Nano Products Inc. and produced metallic traces with up to 70 % bulk conductivity at a sintering temperature of 350 °C. Experimental results show that the strain gauges work as expected, with a reliable sensor signal after repeated cycling. Aerosol Jet is beneficial in that it offers the ability to rapidly print strain gauges in arbitrary locations in a small form factor.

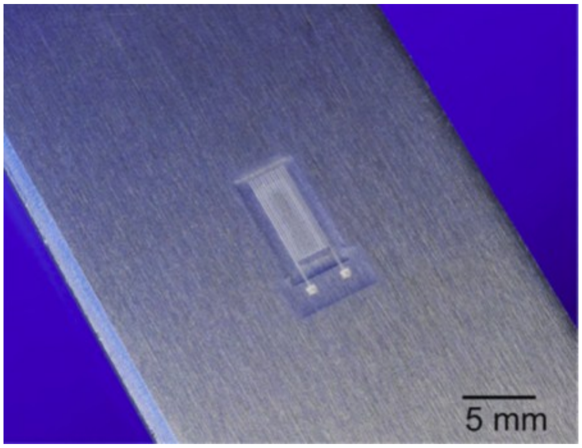

Figure 7. All Aerosol Jet printed strain gauge on aluminum substrate with polymer isolation and encapsulation, reprinted from Maiwald et al. [27], Copyright 2010, with permission from Elsevier.

2.5.2. Printed Metallization Layer for Solar Cells

Van Hest et al. [28, 29] utilized metal burn-through inks designed for the Si_3N_4 anti-reflection coating (ARC) on solar cells. They printed metal inks, based on a combination of silver, nickel and copper, under ambient and inert atmospheres with trace widths of approximately 50 µm. In addition to metal inks, they are currently investigating silicon dopant containing conductive inks, laser sintering of Aerosol Jet printed traces, and printed interdigitated back contact (IBC) cells. If more information about conductive inks for solar cells is desired, a review of printed inorganic solar cells, and the available inks for conductive traces containing metalorganic, nanoparticle, and glass frit for example is written by that same group at NREL (Habas et al) [30].

Researchers at Fraunhofer ISE [31-33] devised a front metallization scheme in which the front side metallization layer is deposited with Aerosol Jet, cured, and followed with a light induced plating (LIP) of silver. The LIP process preferentially electroplates silver onto the Aerosol Jet printed traces when the solar cell is under illumination due to the potential on the metal. A final line width of 50 µm and height of 10 µm can be achieved with a 25 – 30 µm wide by 1 µm high Aerosol Jet printed seed layer. This method reduced the series resistance loss normally resulting from the greater than bulk resistivity of printed silver traces by plating silver onto the contact thereby reducing the effective bulk resistivity [32]. Seed layer traces as thin as 14 µm could be achieved with a metalorganic ink, but with poor edge definition as illustrated in Figure 8a [33]. An SEM image of the finished trace on a solar cell with the seed layer shown in orange can be seen in Figure 8b [32], notice that the majority of the volume of the trace is plated silver. The procedure used by Fraunhofer greatly reduces the complexity of solar cell manufacturing as compared to a photolithographically defined metallization layer and may see commercial application. An improvement to the Aerosol Jet with LIP method was reported by Drew et al. [31] where laser chemical processing (LCP) was used to simultaneously form selective heavily doped emitters and burn through the SiO_2 ARC layer before Aerosol Jet printing. Minimum contact resistance achieved with Aerosol Jet was 0.99 mΩ-cm^2, much greater than that achieved with evaporated Ti/Pd/Ag contacts (~0.15 mΩ-cm^2), but low enough to be used for 1-sun illumination [31]. Without LCP treatment, minimum contact resistance was 2 mΩ-cm^2 [32]. This method is another example of the innovations possible with A-DW technologies combined with other techniques.

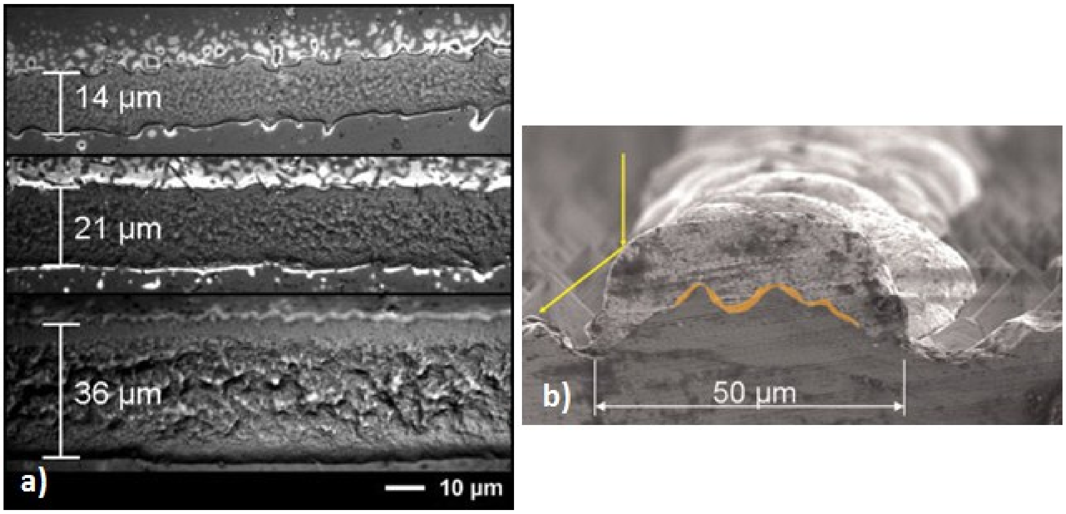

Figure 8. Aerosol Jet printed Ag traces for solar cells; a) optical image prior to LIP, reprinted from Mette et al. [33], Copyright 2007, with permission from John Wiley & Sons LTD. (b) SEM image of cross section of Aerosol Jet printed trace with LIP. Aerosol Jet printed seed layer is highlighted in orange, reprinted from Horteis and Glunz [32], Copyright 2008, with permission from John Wiley & Sons LTD.

2.5.3. Printed Actives

Folgar et al [34] produced multilayer structures using ceramic-based inks printed with Aerosol Jet to form capacitors. 3D structures were formed through the use of a combination of Aerosol Jet and selective laser sintering (SLS). Their work is additional evidence in the ability to use A-DW systems for multilayer components. More complicated multi-layer devices were built by Ha et al. [35] and Cho et al. [36] who used Aerosol Jet for TFTs with printed CNT actives. The source and drain were made via photolithography, while the rest of the device was printed. The active layer was printed using an aqueous dispersion of CNTs, the dielectric was a printed ion gel, and the gate was printed PEDOT:PSS. A diagram and image of the device is shown below in Figure 9a and b. This device is impressive in that the performance (i.e., mobility, switching speed) was improved from 200 µs to 50 µs when compared to other printed devices in literature even at a supply voltage below 3V [35, 37, 38]. In Ha's work, the TFT had a 50 µm × 400 µm length and width, respectively. Jones et al. [39], Vaillancourt et al. [40] and King and Renn [25] each printed a similar CNT-based TFT using Aerosol Jet where features as fine as 10 µm with channel lengths of 100 µm are afforded [41]. An image of the TFT is shown in Figure 9c. This TFT had the silver nanoparticle-based source, drain and gate contact along with the CNT active layer, ion gel dielectric and PEDOT gate produced by Aerosol Jet.

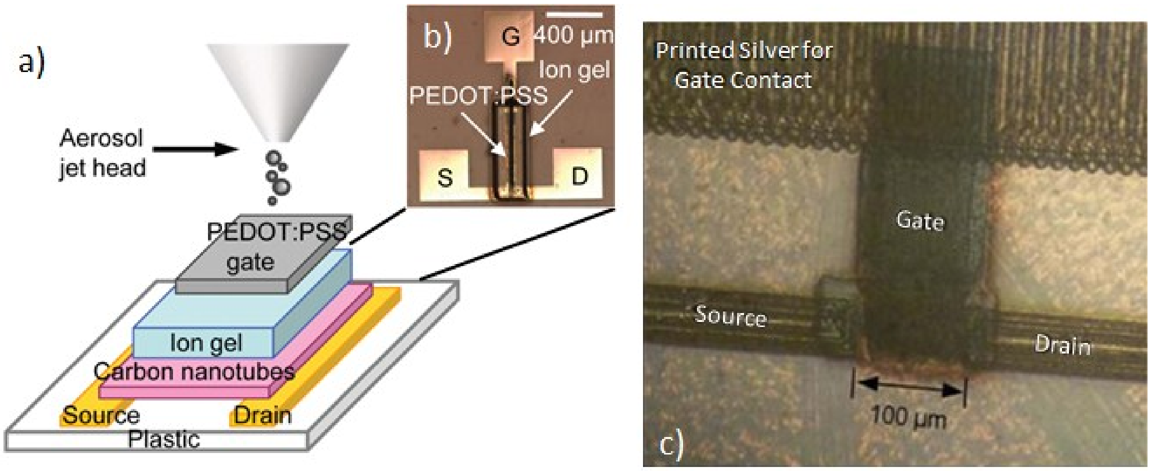

Figure 9. a) Schematic representation of an Aerosol Jet printed CNT based TFT. Source and drain were lithographically patterned while active (CNT), dielectric (ion gel), and gate (PEDOT:PSS) were made with Aerosol Jet. b) image of patterned TFT [35]. Copyright 2010 American Chemical Society. c) Image of CNT based TFT with silver contacts produced by Aerosol Jet, spincoated CNT film, ion gel dielectric and PEDOT:PSS gate, reprinted from King and Renn, and Jones et al. [25, 39]. Copyright 2010, with permission from Optomec and Elsevier, respectively.

3. PHYSICS OF AEROSOLS

3.1. Sum of Forces on Aerosols

A fundamental understanding of the physics of the aerosol fluid interaction is the foundation to improved deposition characteristics (i.e., focus, collimation, line width, reduced overspray) for all A-DW methods. Indeed, such insight can lead to novel technologies as illustrated by CAB-DW and MCS. Modeling of aerosol-fluid interactions is not new, with models dating back to Stokes' work in 1851. The movement of aerosol particles can be determined by these aforementioned forces applied to Newton's 2nd law where force equals mass times acceleration as shown below:

$$\frac{4}{3}\pi a^3 \rho_p \frac{d\mathbf{v}_p}{dt} = \sum \mathbf{F}, \tag{1}$$

where a is the particle radius, ρ_p is the particle density, $\mathbf{v}_p$ is the velocity vector of the particle, $\sum \mathbf{F}$ is the sum of all forces acting on the aerosol particle. Many forces acting on a particle in a fluid have been derived, but in general seven forces are commonly used for modeling of the fluid-particle interaction of aerosols:

$$\sum \mathbf{F} = \mathbf{F}_{St} + \mathbf{F}_{Ba} + \mathbf{F}_{Vm} + \mathbf{F}_{Ps} + \mathbf{F}_{Gr} + \mathbf{F}_{Ma} + \mathbf{F}_{Sa}, \tag{2}$$

where $\mathbf{F}_{St}$ is Stokes force (steady viscous drag force), $\mathbf{F}_{Ba}$ is Basset force (non-steady viscous drag force), $\mathbf{F}_{Vm}$ is the virtual mass force (inertia of fluid surrounding particle added to particle), $\mathbf{F}_{Ps}$ is the pressure gradient force, $\mathbf{F}_{Gr}$ is the buoyancy force caused by gravity, $\mathbf{F}_{Ma}$ is the Magnus lift force due to particle rotation, and $\mathbf{F}_{Sa}$ is the Saffman lift force on a particle with local shear flow [8, 42-50]. It is understood that there are several other forces which may act on aerosol particles in certain circumstances including Brownian diffusion, thermophoresis, diffusiophoresis, photophoresis, electromagnetic radiation pressure, acoustic pressure, electrostatic and van der Waals [51]. For the applications discussed here, impact of the forces on the aerosol particles is minimal as they are not due to fluid-particle interactions and hence are out of the scope of this review.

Sir George Gabriel Stokes [52] developed the first theoretical model for the forces acting on spherical aerosol particles in a viscous fluid under laminar flow conditions. Stokes solved the equations of motion (Navier-Stokes) for laminar flow around a cylinder and sphere, and integrated the forces applied to the surface of the body. Stokes found the force on a particle, $\mathbf{F}_{St}$:

$$\mathbf{F}_{St} = 6\pi a \mu_f (\mathbf{v} - \mathbf{v}_p), \tag{3}$$

where μ_f is the fluid viscosity and $\left(\mathbf{v} - \mathbf{v}_p\right)$ is the fluid velocity relative to the moving particle [53-55].

The Basset force is defined as [44, 45, 47]:

$$\mathbf{F}_{Ba} = 6a^2 \sqrt{\pi \mu_f \rho_f} \int_0^t \left(\frac{d\mathbf{v}/dt - d\mathbf{v}_p/dt}{\sqrt{t-\tau}} \right) d\tau, \tag{4}$$

where ρ_f is the density of the fluid.

Assuming a simple model with constant acceleration, Chao Zhu and Liang-Shih Fan in the CRC Handbook of Fluid Dynamics [56] mentioned that the ratio of the Basset force to the Stokes force looks as follows:

$$\varepsilon_{Ba} = \frac{|\mathbf{F}_{Ba}|}{|\mathbf{F}_{St}|} = \sqrt{\frac{18}{\pi}\frac{\rho_f}{\rho_p}\frac{\tau_\mu}{t}} \tag{5}$$

where τ_μ is the Stokes relaxation time: $\tau_\mu = \dfrac{2a^2\rho_p}{9\mu_f}$

Marshall [46] found that the ratio of the Basset force to the drag force can be expressed as

$$\frac{|\mathbf{F}_{Ba}|}{|\mathbf{F}_{St}|} \cong \mathrm{Re}_p^{1/2} << 1, \tag{6}$$

where Re_p is the Reynolds number of the particle with respect to the fluid:

$$\mathrm{Re}_p \equiv \frac{2a\rho_f|\mathbf{v}-\mathbf{v}_p|}{\mu_f}. \tag{7}$$

The virtual mass force, $\mathbf{F}_{Vm}$, is given by [42, 46]:

$$\mathbf{F}_{Vm} = -c_M \frac{\rho_f}{\rho_p} m \left(\frac{d\mathbf{v}}{dt} - \frac{d\mathbf{v}_p}{dt} \right), \tag{8}$$

where m is the mass of the particle, and c_M is the added mass coefficient, which is equal to 0.5 for a sphere. The pressure gradient force, $\mathbf{F}_{Ps}$, due to the acceleration of the external flow past the particle, is calculated by the following equation [42, 46]:

$$\mathbf{F}_{Ps} = m \frac{\rho_f}{\rho_p} \frac{D\mathbf{v}}{Dt}, \tag{9}$$

where D/Dt denotes the rate of change with time following a fluid particle, such that

$$\frac{D\mathbf{v}}{Dt} = \frac{d\mathbf{v}}{dt} - \left[\left(\mathbf{v}_p - \mathbf{v} \right) \cdot \nabla \right] \mathbf{v}. \tag{10}$$

The buoyancy force, $\mathbf{F}_{Gr}$, due to gravity is equal to

$$\mathbf{F}_{Gr} = m \left(1 - \frac{\rho_f}{\rho_p} \right) \mathbf{g}, \tag{11}$$

where $\mathbf{g}$ is the acceleration vector due to gravity.

Magnus force, $\mathbf{F}_{Ma}$, is present if the particle is in rotation with respect to the surrounding fluid, and is given by [44, 46]:

$$\mathbf{F}_{Ma} = -\frac{3}{4} m \frac{\rho_f}{\rho_p} \left(\frac{1}{2} \boldsymbol{\omega} - \boldsymbol{\Omega} \right) \times \left(\mathbf{v}_p - \mathbf{v} \right), \tag{12}$$

where $\boldsymbol{\omega}$ is the vorticity of the fluid surrounding the particle and $\boldsymbol{\Omega}$ is the angular rate of rotation of the particle. Based on the analysis given in [56], it can be noted that the ratio of Magnus force to Stokes force is equal to:

$$\varepsilon_{Ma} = \frac{\left|\mathbf{F}_{Ma}\right|}{\left|\mathbf{F}_{St}\right|} = \frac{a^2 \rho_f \left| \frac{1}{2} \boldsymbol{\omega} - \boldsymbol{\Omega} \right|}{6 \mu_f}, \tag{13}$$

Assuming that the fluid flow is non-rotational and the aerosol particle rotates due to local shear of the carrier flow, $\left| \frac{1}{2} \boldsymbol{\omega} - \boldsymbol{\Omega} \right| \approx \left| \frac{\partial u}{\partial y} \right| \approx \frac{U}{R}$, this ratio of Magnus force to Stokes force can be further simplified to

$$\varepsilon_{Ma} \cong \frac{a^2 \rho_f U}{6 \mu_f R}, \tag{14}$$

where u is the gas axial velocity component, U is the mean velocity of the fluid flow through the capillary, and R is the radius of the capillary. Therefore, the ratio ε_{Ma} is about 10^{-3}, assuming aerosol particles of 1 μm diameter moving in nitrogen at standard conditions with mean velocity of 50 m/s through a capillary of 100 μm radius.

Saffman force, $\mathbf{F}_{Sa}$, is a lift force applied to aerosol particles in a simple laminar shear flow (Poiseuille flow) and was developed by P.G. Saffman in 1965 [49]. The lift is proportional to the rate of shear and the magnitude of the relative velocity of the particle with respect to the fluid:

$$\mathbf{F}_{Sa} = 6.46\, a^2 \left(u - u_p\right)\sqrt{\rho_f \mu_f \left|\frac{\partial u}{\partial y}\right|}\, sign\left(\frac{\partial u}{\partial y}\right)\mathbf{e}_y \quad , \tag{15}$$

where the value 6.46 is a constant from numerical integration determined in the addendum of Saffman [49], u is the gas axial velocity component, and u_p is the particle axial velocity component .

A detailed estimation of the ratio between the Saffman force and the Stokes force in aerosol focusing was given in [8] where Akhatov et al. calculated that:

$$\varepsilon_{Sa} = \frac{\left|\mathbf{F}_{Sa}\right|}{\left|\mathbf{F}_{St}\right|} \approx 0.3\frac{a}{R}\sqrt{\mathrm{Re}_c}\ ,\ \mathrm{Re}_c = \frac{2R\,U\,\rho_f}{\mu_f} \tag{16}$$

Based on their analysis, it was found that ε_{Sa} was about 0.05. Similar results for the ratio of the Saffman force to the Stokes drag force are given by Chao Zhu and Liang-Shih Fan in the Handbook of Fluid Dynamics [56]:

$$\varepsilon_{Sa} = \frac{|\mathbf{F}_{Sa}|}{|\mathbf{F}_{St}|} = \frac{6.46a}{6\pi}\sqrt{\frac{\rho_f}{\mu_f}\left|\frac{\partial(u-u_p)}{\partial y}\right|} \tag{17}$$

where the simplified form of the Saffman to Stokes force ratio can be presented by the equation below assuming simple shear flow:

$$\varepsilon_{Sa} = \frac{|\mathbf{F}_{Sa}|}{|\mathbf{F}_{St}|} = \frac{6.46}{12\pi}\sqrt{\mathrm{Re}_p}\ ,\ \mathrm{Re}_p = \frac{2a\,\rho_f|\mathbf{v}-\mathbf{v}_p|}{\mu_f} \tag{18}$$

The forces acting on the aerosol particles are only important if they are appreciable as compared to Stokes force. For the analysis of aerosol particles of 0.5 – 5 µm, gravity force is not appreciable. Marshall found that the Basset force may be ignored [46]. Crowe et al. [44] found that the pressure gradient force, virtual mass force, and Basset force may also be ignored. Akhatov et al. agrees with this elimination of forces and summarizes that the two most significant forces are Stokes and Saffman [8].

3.2. Stokes Correction Factor for Rarefied Gases

The Stokes drag force assumes a linear dependence of the force on the relative velocity of the particle to the fluid (lag). A linear dependence is applicable for many particle-fluid combinations but experimental deviations in certain situations such as in rarified flows needed to be addressed if the particle size is small (< 0.5 µm) . Several models for the lag, including those by Cunningham [57] and a more revised model by Carlson and Hoglund [58] that take into account the gas slip on the particle surface due to gas rarefication (based on Knudsen number) and the magnitude of the relative velocity of the particles with respect to the fluid, have been devised.

Cunningham [57], related the variation in Stokes force to the Knudsen number by

$$F_{StokesCc} = \frac{F_{Stokes}}{1 + A'Kn}, \tag{19}$$

where Kn is the particle Knudsen number (mean free path / diameter), and A' a non-dimensional coefficient. In this model, Stokes force has less of an effect as Kn increases due to the slip of the fluid on the particle surface.

Knudsen and Weber [59] discovered that Equation (19) is only valid for very small Kn. To incorporate large variances in Kn, three additional parameters were included to generate the Stokes-Cunningham equation:

$$F_{StokesCc} = \frac{F_{Stokes}}{1 + Kn_p\left(A + Be^{-E/Kn_p}\right)}, \tag{20}$$

where A, B, and E are constants determined experimentally [54, 60].

Table 1 gives a sampling of the many experimental values for the parameters in the Cunningham slip correction factor. Many of the correction factors are based on the oil drop experiments by Millikan [55] where the slip on 0.3 μm oil droplets in air was evaluated. The drift velocity of the particles was measured and used to determine the slip correction factors.

Table 1. Stokes-Cunningham Slip Correction Factors, reprinted from Li and Wang [54] http://link.aps.org/doi/10.1103/PhysRevE.68.061206, and Allen and Raabe [61], Copyright 2003 and 1982, with permission from American Physical Society and Elsevier, respectively.

Author, Year	Mean free path (μm)	A	B	E	A+B
Knudsen and Weber, 1911 [59]	0.09417	0.772	0.40	1.63	1.172
Millikan, 1923 [55]	0.09417	0.864	0.29	1.25	1.154
Langmuir, 1942 [62]	0.133	0.62	0.22	2.20	0.84
Davies, 1945 [63]	0.066	1.257	0.40	1.10	1.657
DeMarcus and Thomas, 1952 [64]	0.0655	1.25	0.44	1.09	1.690
Reif, 1958 [65]	0.0652	1.26	0.45	1.08	1.710
Fuchs, 1964 [66]	0.0653	1.246	0.42	0.87	1.666
Dahneke et al., 1982 [67]	0.066	1.234	0.414	0.87	1.648
Allen and Raabe, 1982 [61]	0.0673	1.155	0.471	0.596	1.626
Buckley and Loyalka, 1989 [68]	---	1.099	0.518	0.425	1.617

3.3. Stokes Correction for Reynolds and Mach Numbers

Stokes drag force acting on a spherical particle, Equation (3), was derived for low Reynolds numbers ($\mathrm{Re}_p << 1$), therefore, if considering the flows of spherical particles with broad range of Reynolds numbers, the Stokes equation should be revised, these corrections are especially critical in modeling applications such as MCS. Clift et al. [69] summarized all empirical and semi-empirical drag corrections C_D for different ranges of Reynolds number in

Table 2 where Stokes force is related to C_D according to Equation (21) as follows:

$$\mathbf{F}_{St} = \frac{\pi}{2} C_D \rho_f a^2 (\mathbf{v} - \mathbf{v}_p)^2 , \tag{21}$$

Clift et al. also investigated the drag coefficient correction for Stokes force in the case of solid particles of arbitrary shape (spheroids, disks, cylinders, etc.) and ellipsoidal fluid particles [69], but the dependency of the drag force on the particle shape is beyond the scope of this review paper. In general, corrections to Stokes force are not only dependent on the particle shape, orientation to the flow, and Reynolds number, but also on Mach number and the turbulence level of the fluid. Carlson and Hoglund [58] devised an improved empirical correction factor based on the particle Reynolds number, Re_p, and the Mach number, M_p, according to Equation (22) as follows:

$$G = \left(1 + \frac{1}{6}\mathrm{Re}_p^{2/3}\right)\left(1 + e^{-\frac{0.427}{M_p^{4.63}}}\right) , \tag{22}$$

where the relative Mach number of the particle compared to the fluid is

$$M_p = \frac{\left|\mathbf{v} - \mathbf{v}_p\right|}{C_g}, \text{ and } \mathbf{F}_{St} = 6\pi a \mu_f G(\mathbf{v} - \mathbf{v}_p) \tag{23}$$

and C_g is the speed of sound of the gas.

Table 2. Summary of literature for drag coefficients at different Reynolds numbers, reprinted from Clift et al. [69], Copyright 1978, with permission from Elsevier.

Author(s)	Reynolds Number	C_D
Schiller and Nauman	$\mathrm{Re}_p < 800$	$\frac{24}{\mathrm{Re}_p}\left(1+0.15\,\mathrm{Re}_p^{0.687}\right)$
Lapple	$\mathrm{Re}_p < 1000$	$\frac{24}{\mathrm{Re}_p}\left(1+0.125\,\mathrm{Re}_p^{0.72}\right)$
Langmuir and Blodgett	$1 < \mathrm{Re}_p < 100$	$\frac{24}{\mathrm{Re}_p}\left(1+0.197\,\mathrm{Re}_p^{0.63}+2.6\times10^{-4}\,\mathrm{Re}_p^{1.38}\right)$
Allen	$2 < \mathrm{Re}_p < 500$	$10\,\mathrm{Re}_p^{-1/2}$
Allen	$1 < \mathrm{Re}_p < 1000$	$30\,\mathrm{Re}_p^{-0.625}$
Gilbert et al.	$0.2 < \mathrm{Re}_p < 2000$	$0.48+28\,\mathrm{Re}_p^{-0.85}$
Kurten et al.	$0.1 < \mathrm{Re}_p < 4000$	$0.28+\frac{6}{\mathrm{Re}_p^{0.5}}+\frac{21}{\mathrm{Re}_p}$
Abraham	$\mathrm{Re}_p < 6000$	$0.2924\left(1+9.06\,\mathrm{Re}_p^{-0.5}\right)^2$
Ihme et al.	$\mathrm{Re}_p < 10^4$	$0.36+\frac{5.48}{\mathrm{Re}_p^{0.573}}+\frac{24}{\mathrm{Re}_p}$
Rumpf	$\mathrm{Re}_p < 10$	$2+\frac{24}{\mathrm{Re}_p}$
Rumpf	$\mathrm{Re}_p < 100$	$1+\frac{24}{\mathrm{Re}_p}$
Rumpf	$\mathrm{Re}_p < 10^5$	$0.5+\frac{24}{\mathrm{Re}_p}$
Clift and Gauvin	$\mathrm{Re}_p < 3\times10^5$	$\frac{24}{\mathrm{Re}_p}\left(1+0.15\,\mathrm{Re}_p^{0.687}\right)+\frac{0.42}{1+4.25\times10^4\,\mathrm{Re}_p^{-1.16}}$
Brauer	$\mathrm{Re}_p < 3\times10^5$	$0.4+\frac{4}{\mathrm{Re}_p^{0.5}}+\frac{24}{\mathrm{Re}_p}$
Tanaka and Iinoya	$\mathrm{Re}_p < 7\times10^5$	$\log_{10} G = a_1 w^2 + a_2 w + a_3,\ w=\log_{10}\mathrm{Re}_p$

The correction factor of Carlson and Hoglund [58] is similar to that of Schiller and Nauman [70], but with a Mach number correction included for flow compressibility. The constants are also nearly identical with 1/6 replacing 0.15, and 2/3 replacing 0.687. An even more improved equation has been collected by Wang et al. [71] using the work of [49, 58, 66, 72] which accounts for all of the previously mentioned correction factors:

$$G = \frac{\left(1+\frac{1}{6}\mathrm{Re}_p^{2/3}\right)\left(1+e^{-\frac{0.427}{M_p^{4.63}}-\frac{3}{\mathrm{Re}_p^{0.88}}}\right)}{1+Kn_p\left(2.57+0.68e^{\frac{-1.86}{Kn_p}}\right)} \tag{24}$$

The correction from Schiller and Naumann [70] has been used extensively by several researchers including Wang et al [73] and Kuan and Schwarz [74] who used it to model gas-particle interactions in vertical ducts. Wang and Osiptsov [75] used the correction of Carlson and Hoglund [58] to model the movement of particles in the laminar region near a wall in a dusty gas shock wave.

3.4. Saffman Force

It was first noted by Poiseuille [76] that blood cells had a tendency to stay away from blood vessel walls. Segré and Silberberg [77] noticed that spheres in Poiseuille flow would migrate to 0.6 radii from the centerline of the tube. This phenomenon cannot be explained by Stokes force of any variety and/or particle inertia. Rotational motion of the particles could cause a migration to the centerline due to Magnus force, but not away from the centerline because of the flow profile [78]. To explain the lateral migration of particles Saffman [49] first theoretically analyzed simple shear flow. It was determined that four conditions must be met for there to be an appreciable migration of the particles: 1) very small particle Reynolds numbers, 2) very small shear Reynolds number around the particles, 3) the ratio of the square root of the Reynolds number of the fluid over the Reynolds number of the particle much greater than one and 4) the rotational velocity of the particle must be small [49]. The four conditions are described below:

$$\begin{aligned}&\mathrm{Re}_p=\frac{\left|u-u_p\right|2a\rho_f}{\mu_f}<<1,\quad \mathrm{Re}_f=\frac{\rho_f(2a)^2}{\mu_f}\left|\frac{\partial u}{\partial y}\right|<<1,\quad \varepsilon=\frac{\sqrt{\mathrm{Re}_f}}{\mathrm{Re}_p}>>1,\\ &\mathrm{Re}_\Omega=\frac{\Omega\rho_p(2a)^2}{\mu_f}<<1\end{aligned} \tag{25}$$

where Ω is the rotational velocity of the particle, and Re_Ω is the rotational Reynolds number of the particle. Saffman derived the force acting on the particles in a simple shear flow (laminar flow) and further developed the equation for the force in Poiseuille flow in a tube.

A diagram of the direction of Saffman force acting on a particle with a velocity less than that of the fluid can be seen in Figure 10. Notice that the particle is forced towards increasing velocity. Saffman [49] force specified that the force is in the direction of increasing velocity for lagging particles, and decreasing velocity for leading particles. Also, the force acting on the particles is increased with an increased fluid velocity gradient and fluid velocity relative to the particle. The direction of Saffman force was verified when compared to the results of Oliver [79]. Oliver found that settling particles in a downward flowing liquid would migrate towards the wall of the tube. Conversely, floating particles would migrate towards the axis in downward flowing liquid. This phenomenon can be explained by the effects of Saffman force.

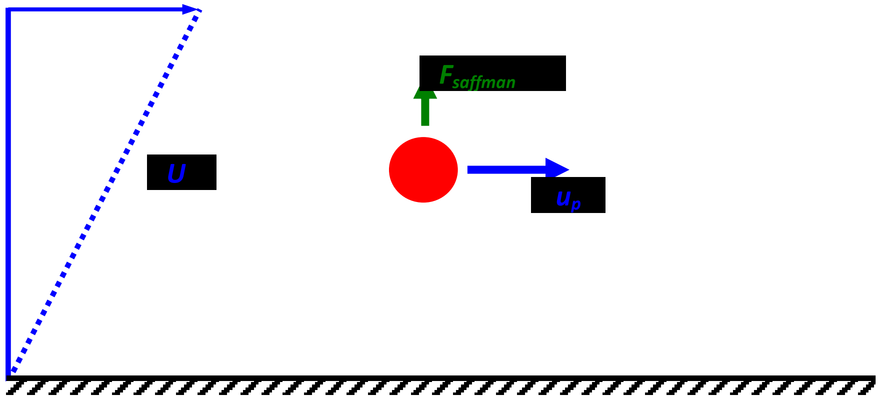

Figure 10. Schematic illustrating direction of Saffman force in shear flow, reprinted from Hoey et al. [17].

Until this point, Saffman force was only considered acting in a one-dimensional fashion. In reality a 2-dimensional generalization for Saffman would be more appropriate. A 2-dimensional flow equation for Saffman force was presented by Crowe et al. [44]:

$$\mathbf{F}_{Sa} = 6.46a^2 \sqrt{\frac{\mu \rho_f}{|\nabla \times \mathbf{v}|}} \left[(\mathbf{v} - \mathbf{v}_p) \times (\nabla \times \mathbf{v}) \right], \tag{26}$$

and further derived by Lutfurakhmanov [80] in his dissertation:

$$
\begin{aligned}
&\mathbf{F}_{Sa} = 6.46a^2\sqrt{\rho\mu}\times \\
&\sqrt{\left|-\frac{\partial u}{\partial x}\sin\alpha_{Sa}\cos\alpha_{Sa}+\frac{\partial u}{\partial y}\cos^2\alpha_{Sa}-\frac{\partial v}{\partial x}\sin^2\alpha_{Sa}+\frac{\partial v}{\partial y}\sin\alpha_{Sa}\cos\alpha_{Sa}\right|}\times \\
&Sign\left(-\frac{\partial u}{\partial x}\sin\alpha_{Sa}\cos\alpha_{Sa}+\frac{\partial u}{\partial y}\cos^2\alpha_{Sa}-\frac{\partial v}{\partial x}\sin^2\alpha_{Sa}+\frac{\partial v}{\partial y}\sin\alpha_{Sa}\cos\alpha_{Sa}\right)\times, \\
&\left[-\left(v-v_p\right)\mathbf{e}_x+\left(u-u_p\right)\mathbf{e}_y\right]
\end{aligned}
\tag{27}
$$

for two-dimensional modeling with $\alpha_{Sa} = \arctan\left(\frac{v-v_p}{u-u_p}\right)$.

3.5. Saffman Force Corrections

As with Stokes force, Saffman force requires corrections to be applicable in many situations such as larger Reynolds number. An equation to model the Saffman force under higher Reynolds numbers was devised by Mei [72]. The model is based on work performed by Dandy and Dwyer [81] who used a three-dimensional numerical simulation to model linear shear flow past a small sphere. It was noted that the shear force coefficient (Saffman force) was near constant for intermediate gas Reynolds numbers, and proportional to the square root of the gas Reynolds number for particle Reynolds numbers less than 40 as seen below:

$$
\begin{aligned}
&\frac{C_L}{C_{LSa}} = (1-0.3314\alpha^{1/2})e^{\frac{-\mathrm{Re}_p}{10}}+0.3314\alpha^{1/2}, \quad \mathrm{Re}_p \le 40 \\
&\frac{C_L}{C_{LSa}} = 0.0524(\alpha\,\mathrm{Re}_p)^{\frac{1}{2}}, \qquad \mathrm{Re}_p > 40
\end{aligned}
\tag{28}
$$

where the correction factors used for Saffman force are the coefficient of lift, C_L,

$$C_L = \frac{F_L}{\frac{1}{2}\rho_f \pi a^2 u^2}, \tag{29}$$

and α

$$\alpha = \frac{1}{2}\mathrm{Re}_p\,\varepsilon^2 \tag{30}$$

The correction from [72] used in [8, 71, 75, 82] can be further expressed

$$H = \begin{cases} 0.23434\left(1-e^{-0.1\mathrm{Re}_p}\right)\sqrt{\dfrac{\mathrm{Re}_f}{\mathrm{Re}_p}} + e^{-0.1\mathrm{Re}_p}, & \mathrm{Re}_p \le 40 \\ 0.0371\sqrt{\mathrm{Re}_f}, & \mathrm{Re}_p > 40 \end{cases}, \tag{31}$$

where Saffman force is then,

$$\mathbf{F}_{Sa} = 6.46\,H\,a^2\left(u-u_p\right)\sqrt{\rho_f\mu_f\left|\frac{\partial u}{\partial r}\right|}\,sign\left(\frac{\partial u}{\partial r}\right)\mathbf{e}_y \tag{32}$$

McLaughlin investigated the Saffman force correction for higher Reynolds numbers ($\mathrm{Re}_f, \mathrm{Re}_p$) in [83], and reported the correction data table in the case when $0.025 \le \varepsilon \le \infty$ ($\varepsilon = \sqrt{\mathrm{Re}_f}/\mathrm{Re}_p$). Mei in [72] further analyzed the McLaughlin tabular data for the range $0.1 \le \varepsilon \le 20$ and proposed to use the following function to fit the correction data:

$$\frac{C_L}{C_{LSa}} = 0.443 \times 0.6765[1 + \tanh(2.5\log_{10} \varepsilon + 0.191)]\{0.667 + \tanh[6(\varepsilon - 0.32)]\} \quad (33)$$

A comparison of Saffman force and the correction factors proposed by Mei [72], along with work by Mclaughlin [83], can be seen in Figure 11. Notice that Saffman force is linear throughout the log-log plot. Mei's correction factor was close to Saffman for small Reynolds numbers. After a Reynolds number greater than approximately 5, the correlation departed from Saffman force. The ability to use Mei's correlation allowed for much greater Reynolds numbers for Saffman force. In fact, Reynolds numbers as high as 1000-1100 have been used [84].

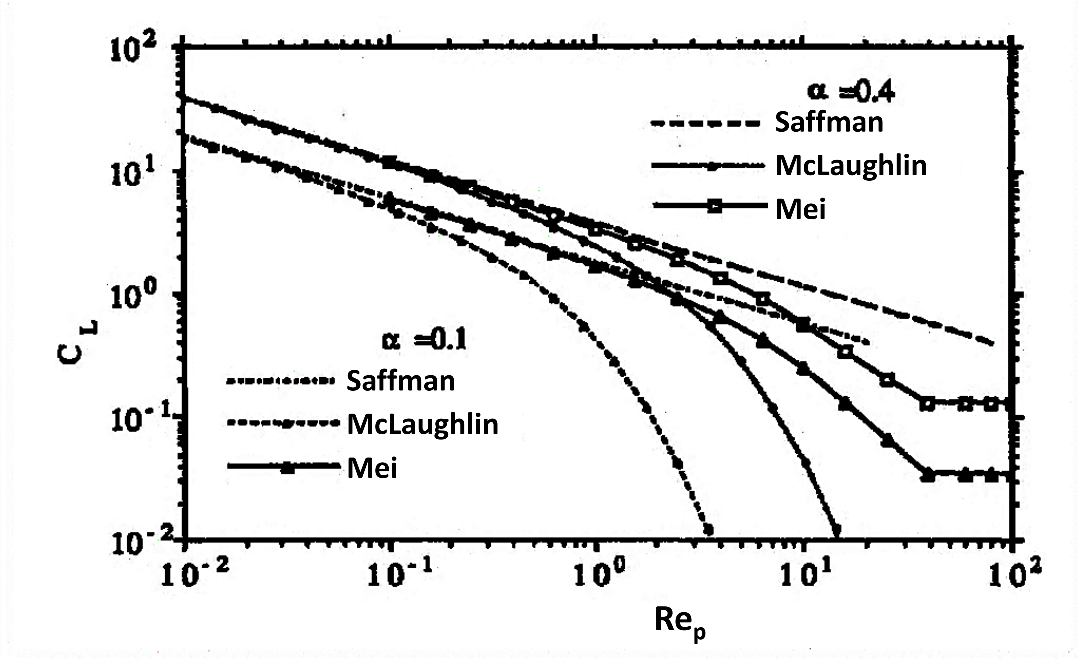

Figure 11. Graph of shear coefficient vs. Reynolds number based on the analyses of Mei [72], McLaughlin [83], and Saffman [49], reprinted from Mei [72], Copyright 1992, with permission from Elsevier.

3.6. Theoretical Application of Forces

3.6.1. Stokes Force

Aerosol focusing has been extensively studied in supersonic jets with very large Reynolds numbers. Much of the research has been provided by Cheng and Dahneke [85], Dahneke et al [67], and Fernandez de la Mora and Riesco-Chueca [53]. It was assumed by these experimenters that particle focusing occurs strictly due to inertial effects and Stokes force, where one would infer that Saffman force is not applicable.

Fernandez De La Mora and Riesco-Chueca [53, 86] found that the focusing of the particles depended on the Stokes number which relates the amount of coupling that the particles have with the fluid by a characteristic time, τ_μ, divided by a characteristic length, τ_L:

$$St = \frac{\tau_\mu}{\tau_L}, \quad \tau_\mu = \frac{2a^2\rho_p}{9\mu_f}, \quad \tau_L = \frac{L}{U}, \tag{34}$$

where L is the fluid characteristic length scale, and Stokes number is calculated as follows:

$$St = \frac{2\rho_p a^2 U}{9\mu_f L}. \tag{35}$$

It should be noted that larger Stokes numbers correlate to particles which have less of a tendency to follow the flow. It was found (Israel and Friedlander [87], Israel and Whang [88], Stoffels [89], Sinha et al. [90], Estes et al. [91], Kievit et al. [92], Reents et al. [93], Mallina et al. [60], and Li and Wang [54]) that focusing of particles in a nozzle is mainly dictated by the Stokes number which is in agreement with Fernandez De La Mora and Riesco-Chueca [53, 86]. The focal point distance from the exit of the nozzle, x_f , as seen in Figure 12 depends on the Stokes number, and the initial seeded radial position, r_o [94]. The focal point moves towards infinity as the Stokes number reaches a critical Stokes number S^* (approximately 1).

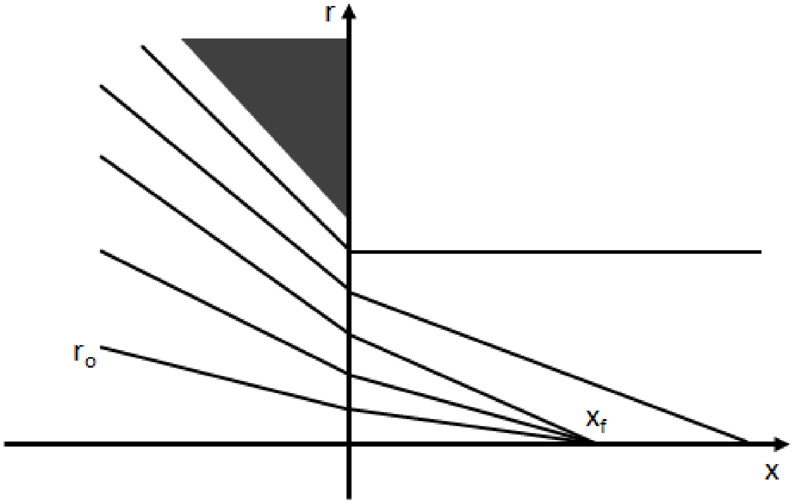

Figure 12. Diagram of particles at initial seeded radius, r_o , exiting nozzle and focused at a distance, x_f , from the nozzle (after [53]), reprinted from Hoey et al. [17].

Rao et al [94] conducted his experiment with moderate Reynolds numbers (3 to 1000) and noticed that the focusing effects under flows in the viscous regime may actually be greater than those of potential flows. This understanding came about with only Stokes force considered acting on the particles. Mallina et al. [60] describes the focusing mechanisms applicable to nozzles and capillaries where focusing can be predicted by the Stokes number, with a Cunningham correction factor. A diagram of the aerosol focusing through a nozzle of 500 µm diameter can be seen in Figure 13. Notice that larger particles focus at increasing distances from the nozzles, up until a critical diameter where focusing no longer occurs. In this case, all particles were seeded at 0.1 R_o, where R_o is initial radius of the capillary. A similar experiment was done for a capillary of 500 µm in diameter and 32 cm in length by Cheng and Dahneke [85].

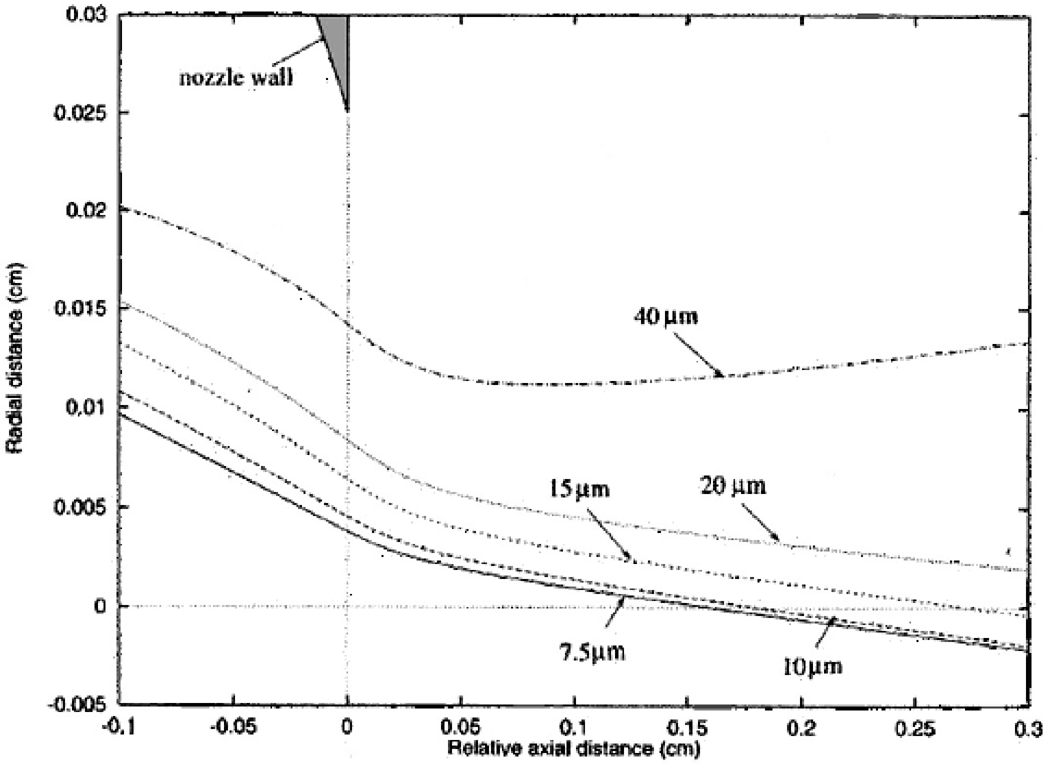

Figure 13. Diagram of trajectories for 7.5-40 µm diameter particles exiting a 500 µm nozzle, reprinted from Mallina et al. [60], Copyright 1999, with permission from Elsevier.

Liu et al. [95, 96], Di Fonzo et al. [97], Wang and McMurry [98], and several others designed aerodynamic lens systems that collimate aerosol beams using a series of thin plates. Many of the systems were designed for low pressure and particles in the nanometer range. Modeling of the aerosol particles was done using only Stokes force where it was found that a continuum approximation was only applicable for $Kn < 0.1$. Wang and McMurry [98] later designed a computer program which determines the correct parameters for an aerodynamic lens system. Parameters such as flow rate, pressure, diameter of the lenses, and spacing between lenses were optimized to provide a collimated aerosol stream of polydisperse particle. The program used values obtained by numerical simulations of the flow of aerosol particles through the lens system. A diagram of an example lens system is shown in Figure 14. Typical values for the flow rate, pressure, length between nozzles, and nozzle diameters are 100 sccm, 93-600 Pa, 10-20 mm, and 1.26-3.2 mm, respectively. There are usually 3 to 5 lenses, but as many as 10 have been commonly used. Particle sizes range from 3-250 nm, but particles as large as 3 μm have been used in lens systems by others [98, 99].

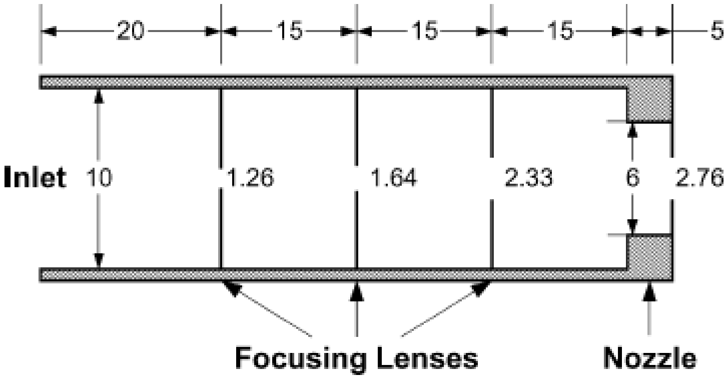

Figure 14. Schematic of aerodynamic lens system for focusing aerosol particles (dimensions in mm), from Wang et al. [99], Aerosol Science and Technology, Copyright 2005, Mount Laurel, NJ. Reprinted with permission.

Rao et al. [94] noticed that focusing of particles is reduced due to a "geometric aberration effect." The effect is caused by particles which are seeded into the nozzle at varying radii. The particles focused at different locations along the axis, causing a dull focal point. Focusing was improved by seeding the aerosol particles closer to the axis with a clean air sheath gas. For Rao's experiments, a 50% sheath gas was used to aid in achieving a focus of less than 2% of the nozzle diameter. These results were accomplished with a thin-plate nozzle with a diameter on the order of 1mm. Renn et al [100] modeled the focusing of aerosol particles through a 100 μm nozzle with variable sheath gas using only Stokes force and particle inertia. They proposed that the focusing of aerosol particles is dependent on the particles' Stokes number. Particles with high Stokes numbers, which in this case are particles around 1 μm in diameter and larger, would converge and deposit on a substrate. Particles less than 1 μm in diameter will follow the flow streamlines and not deposit on the substrate. Good evidence that a focusing mechanism was missing came from Renn et al. [16], where the beamwidth of aerosol particles exiting a 100 μm nozzle was compared to a simulation. In this case, the actual focusing was much better than the predicted focusing with particle beams focused to 5-10X smaller than the nozzle diameter [4].

3.6.2. Saffman Force

Most research using Saffman force is for applications of particles flowing over a flat plate, or in a long capillary. We have however included Saffman force in modeling of aerosol focusing for direct-write applications [8, 82]. Lipatov et al. [84, 101] described a situation similar to Oliver's [79], where it was found that heavy particles in a down flow tube would migrate towards the wall. In up flow conditions the opposite occurred, and the particles migrated towards the tube axis. Lipatov et al. [101] experimentally validated the effects of Saffman force using ducts in a wind tunnel. Ducts ranged from 3 to 10 mm in diameter and 10 to 25 cm in length. Monodisperse Lycopodium spores with a radius of 16 µm were used as the aerosol particles. Flow velocities ranged from 0.4 to 1.5 m/s. The particle deposition coefficients for down flow and up flow P_d and P_u, respectively, were calculated experimentally and analytically using Saffman force. It was found that P_d ranged from 15-30% while P_u was less than 3. The large deviance of P_d and P_u is explained with Saffman force.

To model dust particles in the laminar region following a shock wave in coal mines, Wang and Osiptsov [75] and Wang et al [71] included both Stokes and Saffman forces. It was shown that Magnus force is not relevant in this situation because the particles' angular velocities were near the same order of magnitude as the velocity in the direction perpendicular to the wall. Saffman force was calculated with the correction factor used by Mei et al [72] in Equation Set (28). Stokes force was calculated using Equation (22). It was noticed that a lateral migration of particles from a wall, caused localized accumulations away from the wall. A Lagrangian approach to determining velocities was used in [71, 75] with two-way coupling of the particles and the fluid under high particle concentrations in [71]. Hwang [102] used Saffman force in a similar situation with a weak shock wave in a dust deposit. It was determined that after the shock wave, a velocity gradient and subsequent force acting on the dust particles perpendicular to the velocity gradient were created.

Numerical calculations using a computational fluid dynamics (CFD) program, which takes into account Saffman force, have been studied by Kuan and Schwarz [74] and

El-Batsh [103]. Kuan and Schwarz studied coal dust of 40-80 μm mean diameter in vertical ducts used for coal-fired power plants. Particle tracking was accomplished using the Lagrangian approach. El-Batsh used Saffman force to model near-wall interaction of aerosol particles with a turbine cascade in turbulent flow. Barton [104] used Saffman force in a model which developed a fourth-order Runge-Kutta method to solve the equations of motion for flow of particles over a "backward-facing step." The model included Stokes drag force, gravity, virtual mass, pressure, and Basset force (history integral). It was determined that particles followed the streamlines for low Stokes number, and overshot the streamlines for higher Stokes numbers where the effects of Saffman force increased as the particle Stokes number increased due to an increasing relative velocity (lag) of the particles.

There is literature which describes the modeling of aerosol particles in a nozzle (micro-capillary) using variations of Stokes force and particle inertia without Saffman force by de la Mora and others [53, 54, 60, 98, 100]. Saffman force is used primarily along unbounded walls and long tubes or capillaries by Wang and Mei [71, 72, 75] for example. The inclusion of Saffman force on the focusing of aerosol particles through a nozzle may be necessary for a more complete model as we have described in [8, 82] Stokes force, Saffman force, and particle inertia were required to describe the focusing of aerosol particles emanating from a micro-capillary.

4. COMPUTATIONAL MODELING OF AEROSOLS IN FLOWS

This section contains excerpts from a journal publication by Akhatov et al. in the Journal of Aerosol Science [82].

4.1. Constant Diameter Capillary

The simplest implementation of the aforementioned forces on the trajectories of aerosol particles is in the simulation of Poiseuille flow in a constant diameter capillary. In this case, the velocity distribution *u*(r) in a constant diameter capillary can be determined using Poiseuille's Law (published in 1836), when the flow is considered laminar (*Re*<2100), and with non-slip boundary conditions on the wall. The maximum velocity is determined using volume conservation and geometry. It is also known that the maximum velocity is twice the average velocity of the flow. The velocity distribution using this criterion with *r* as the radial coordinate, *R* as the radius of the nozzle at an arbitrary point *x,* and R_o as the final radius is seen below:

$$\begin{aligned} u &= u_{\max}\left[1-\left(\frac{r}{R}\right)^2\right] \\ u_{\max} &= \frac{1}{4\mu_f}\frac{\Delta p}{L}\left(R^2-r^2\right) \\ u_{\max} &\cong \frac{2Q}{\pi R_o^2} \end{aligned} \tag{36}$$

or non-dimensionalized to the initial radius R_o, and initial maximum velocity u_{max} with the equation set:

$$\bar{r} = \frac{r}{R_o}, \quad \bar{u} = \frac{u}{u_{\max}} \rightarrow$$
$$\bar{u} = (1 - \bar{r}^2), \quad \frac{\partial \bar{u}}{\partial \bar{r}} = -2\bar{r} \tag{37}$$

The velocity in the radial direction is neglected in these equations because the radial velocities are zero for constant radius capillaries. The equations are non-dimensionalized to obtain results that are comparable for various scales of geometries. Using this flow geometry with equations of motion from Newton's 2nd law gives the trajectory of particles. The velocities *u* and *v*, are found using the Eulerian analysis of the flow field. The position and velocity of the particles are analyzed with a Lagrangian approach. The equations of motion are solved using Matlab with a 4th order Runge-Kutta method.

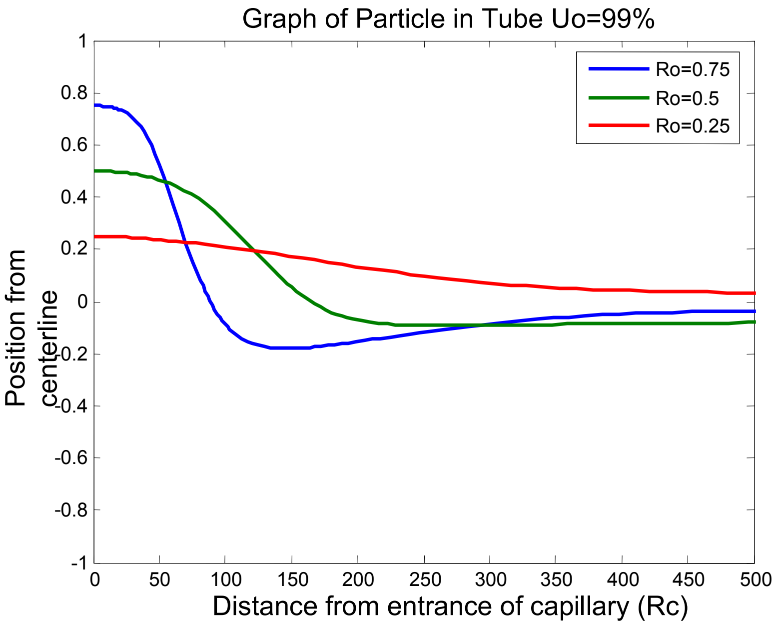

Figure 15. Graph of aerosol particle in 100 μm diameter capillary, with u_{max}= 100 m/s, and initial particle velocity, U_o, 99% of fluid velocity.

A picture of the analysis using the equations of motion can be seen in Figure 15, which displays a graph of three 1 μm radius particles in a capillary beginning at non-dimensionalized radii of 0.75, 0.5, and 0.25. The initial velocity of the particles is 99% of the local fluid velocity for each respective particle. Fluid flow rate is 40 ccm (u_{max} = 100 m/s), using N_2 with density of 1.16 kg/m^3. It can be seen that there is a natural inclination of the particles to move towards the centerline which is caused solely by Saffman force.

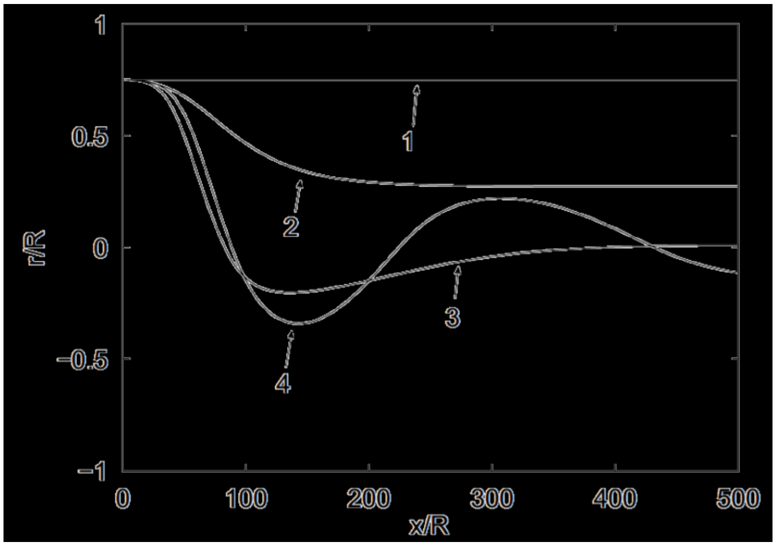

Figure 16. Trajectories of particles of difference size in a micro-capillary of radius R = 50 μm starting at the same initial position $r_p(0)/R$ = 0.75; ρ_p = 2000 kg/m3; μ = 1.67 × 10−5 Ns/m^2, ρ= 1.16 kg/m^3 (nitrogen); u_{max} = 100m/s; (1) a = 0.25 μm; (2) a = 0.5 μm; (3) a = 1 μm; (4) a = 1.5 μm, reprinted from Akhatov et al. [82], Copyright 2008, with permission from Elsevier.

Particles of larger size are more affected by Saffman force as illustrated in Figure 16 where particles of size: 1) a = 0.25 μm, 2) a = 0.5 μm, 3) a = 1 μm, and 4) a = 1.5 μm are focused in a 40 ccm N_2 flow with u_{max} = 100 m/s. In this case, the particles of larger diameter focus to the centerline much faster than small particles.

4.2. Linearly Converging Capillary

In the case of a slowly converging micro- capillary, such that its radius changes linearly with its length rather than constant diameter

$$R(x) = R_1 - \frac{R_1 - R_2}{L} x \tag{38}$$

Here R_1, R_2 are capillary radii at the beginning and at the end, respectively. For estimation purposes the micro-capillary has radii R_1 = 400 μm and R_2 = 50 μm with carrier nitrogen average gas flow of u = 50 m/s. To make calculations as simple as possible, we are assuming here a parabolic Poiseuille velocity distribution in every capillary cross-section. Indeed, if the radius of the micro-capillary slowly decreases, the inertial effects in both the radial and the longitudinal directions can be neglected when (Batchelor, [105]):

$$\left(\frac{R_1 - R_2}{L}\right)\frac{\bar{u}D\rho}{\mu} \langle\langle 1 \tag{39}$$

Using the inlet and outlet radii of the micro-capillary and the viscosity and density of nitrogen, a minimum length of approximately 10 cm is needed to satisfy the inequality from Equation (39). This length is larger than the length of the micro-capillary that is being modeled in this section and used in the experiments to be presented in the next sections, so there is some inherent error due to the inertial forces. More advanced CFD modeling of the gas flow in such a faster converging micro-capillary is needed.

In this case, the parabolic gas velocity distribution presented in the Equation (36) holds with the slight modification

$$u = u_{\max}(x)\left(1 - \frac{r^2}{R(x)^2}\right), \quad u_{\max}(x) = \frac{2Q}{\pi R^2(x)} \tag{40}$$

where Q is the volumetric gas flow rate through the micro-capillary. The streamlines are not exactly unidirectional but are inclined to the axis at a small angle, as shown in Fig. 5. In addition to the axial component of velocity, u, as presented in the Equation (40) there is a radial component, v such that

$$\mathbf{v} = u\mathbf{e}_x + v\mathbf{e}_r, \quad v = -\tan(\alpha)u, \quad \tan(\alpha) = \left(1 - \frac{R_2}{R_1}\right)\frac{R_1}{L}\frac{r}{R(x)} \tag{41}$$

Figure 17 depicts the additions of the radial-velocities to a 100 μm linearly converging, 19.05 mm long capillary. The particles' trajectories look very realistic, except past the end of the tip where only particle inertia is incorporated into the simulation. Notice that the particles do not impact the nozzle wall. Figure 18 is a comparison of the trajectories of aerosol particles with and without Saffman force. It can be seen that the convergence of the particles without Saffman force is at a greater distance from the exit than with Saffman force. The focal distance is 3.4 mm from the end of the tip if only Stokes force is considered. In this simulation, Saffman force is strong enough to focus the particles to 0.1 mm past the nozzle. The very short focal distance seems artificial, but is very dependent on the particle size.

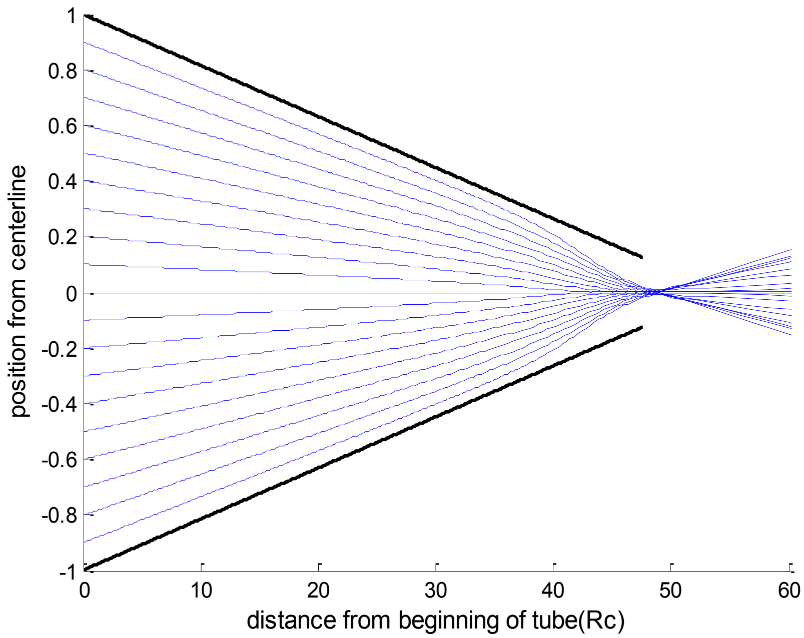

Figure 17. Particles in tip with r-velocity. The parameters used are as follows: The tip outlet diameter, R_f, is 100 µm, and the inlet diameter, R_o, is 800 µm with a length of 19.05 mm. Fluid flow rate is $1.25x10^{-6}$ m^3/s. U_m is 4.97 m/s.

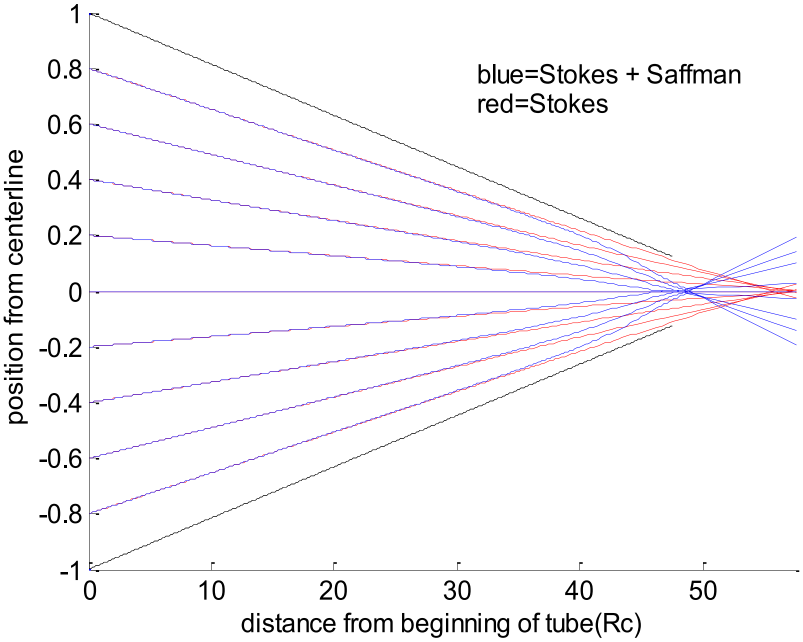

Figure 18. Comparison of trajectories with and without Saffman force. The parameters used are as follows: The tip outlet diameter, R_f, is 100 µm, and the inlet diameter, R_o, is 800 µm with a length of 19.05 mm. Fluid flow rate is $1.25x10^{-6}$ m^3/s. U_m is 4.97 m/s.

4.3. CFD and Analytical Simulation

The previous modeling used an analytical approach to calculate the fluid velocity distribution inside the nozzle, and then calculated the aerosol particle trajectories using that velocity distribution. That simulation was limited to slowly varying nozzle geometries and was not capable of simulating the fluid flow outside the nozzle. To overcome these limitations, a commercial computation fluid dynamics (CFD) software is employed. This simulation with ANSYS CFX, using a finite element scheme calculated the fluid velocity, pressure, temperature, and other physical parameters which can then be used as a library for implementation of the forces acting on aerosol particles. Artur Lutfurakhmanov spent much of his research efforts simulating the fluid flows and aerosol particle trajectories using ANSYS CFX and Matlab, respectively, and has since defended his dissertation [80].

Modeling using ANSYS first requires the use of a defined geometry and a mesh for the locations of the nodes. This is done using ICEM CFD, where axisymmetric flow is considered with a rotation of 5° about the axis. An example geometry for simulation using a linearly converging nozzle with a plenum is shown in Figure 19. For this modeling, boundary conditions must also be set, which occurs in the main ANSYS program. The inlet conditions are set by pressure, mass flow rate, or velocity, and the wall of the nozzle is considered a no-slip condition. The exit of the nozzle is not an appropriate place to put the boundary conditions, and so a plenum of appropriate size (~5 mm length) is added to the simulation. The edges of the plenum are considered openings and a static pressure is set for boundary conditions.

One method to improve upon the velocity distribution inside a converging nozzle was developed by our group [43] and uses a semi-analytical approach with a Taylor's series expansion to simulate the fluid velocity. This fluid velocity along with Poiseuille flow and CFD simulation results are shown below in Figure 20. Results show that there is good agreement between the ANSYS CFX results and that of the semi-analytical approach.

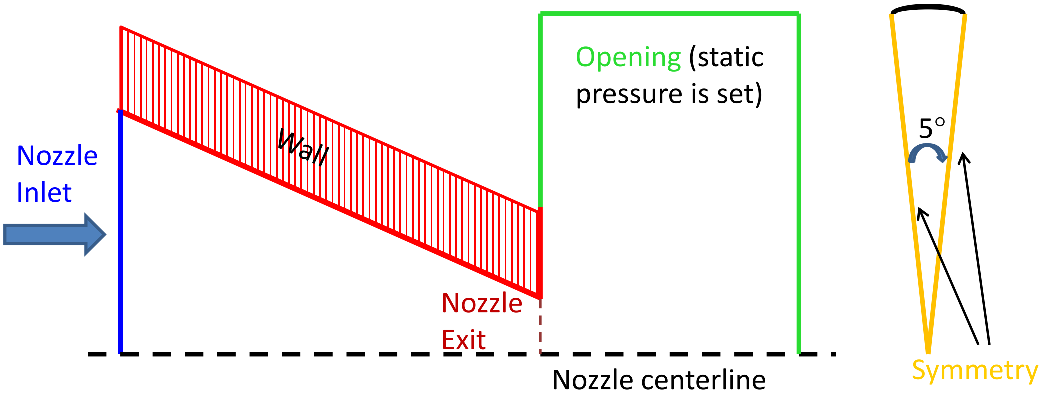

Figure 19. Geometry and boundary conditions for a linearly converging nozzle simulation, reprinted from Lutfurakhmanov [80].

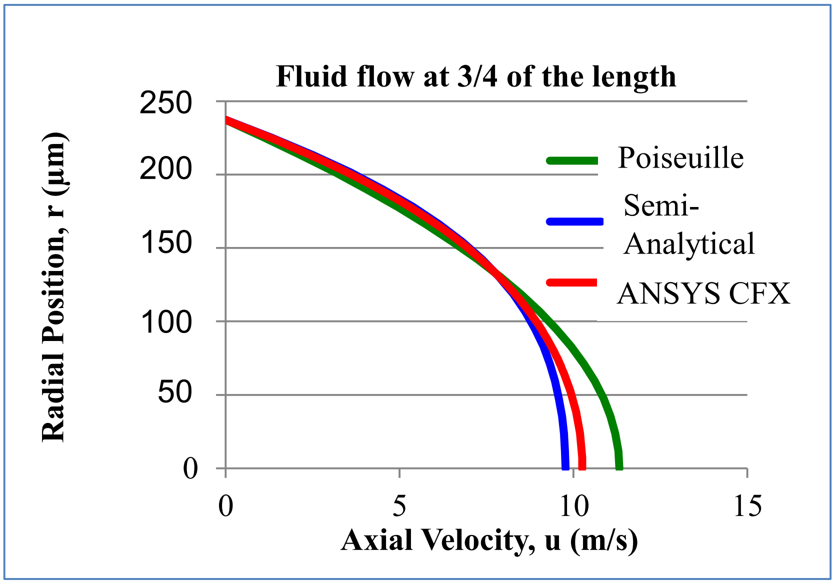

Figure 20. Fluid flow comparison in linearly converging nozzle for Poiseuille flow, Semi-analytical flow, and ANSYS CFX, reprinted from Lutfurakhmanov [80].

The velocity of the aerosol particles as they are traversing through a nozzle is also a valuable comparison to determine if both the analytical model and that of ANSYS CFX are in good agreement. Shown in Figure 21 is such a comparison where components of the gas and particle with the semi-analytical model and ANSYS (cfx) are compared using a) the axial velocity and b) the radial velocity. Results are in good agreement, as such, for future calculations, only the ANSYS fluid flow field results will be used. These results should be more robust for analysis and allow for arbitrary shaped nozzles.

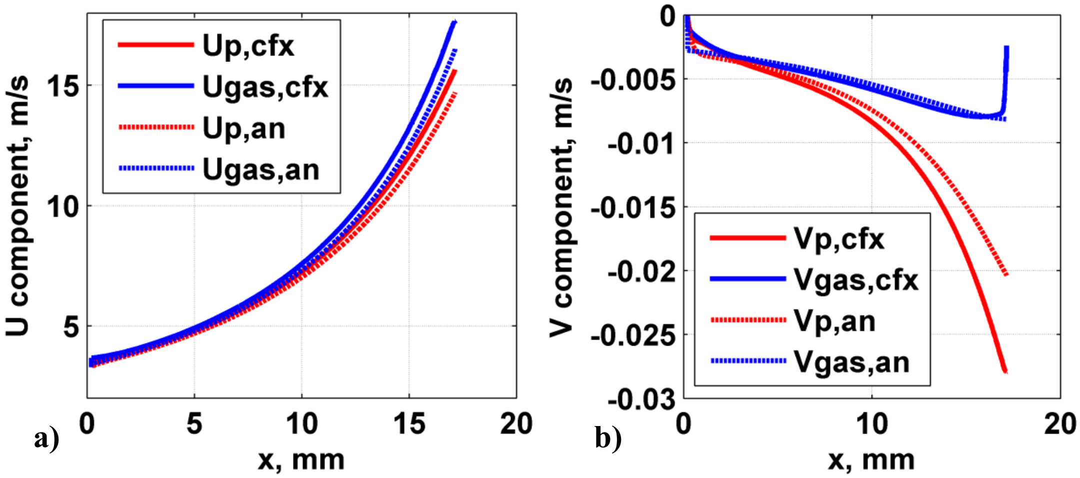

Figure 21. Comparison of ANSYS CFX and semi-analytical fluid and gas velocities of a particle traversing a linearly converging nozzle; a) axial velocity, b) radial velocity, reprinted from Lutfurakhmanov [80].

Simulation of aerosol particles using CFD modeling results in much more realistic trajectories of aerosol particles as compared to the simulation which relied only on an analytical approach. One such simulation using a 200 μm linearly converging nozzle, 19.05 mm long with 3.8 μm silica particles is shown below in Figure 22a where only Stokes forces is used, and Figure 22b where both Stokes and Saffman force are applied to the aerosol particles. One can see that Saffman force has a dramatic effect on the focusing of the aerosol particles creating a focal point after the nozzle exit, while the particles have no focus when only Stokes force is included.

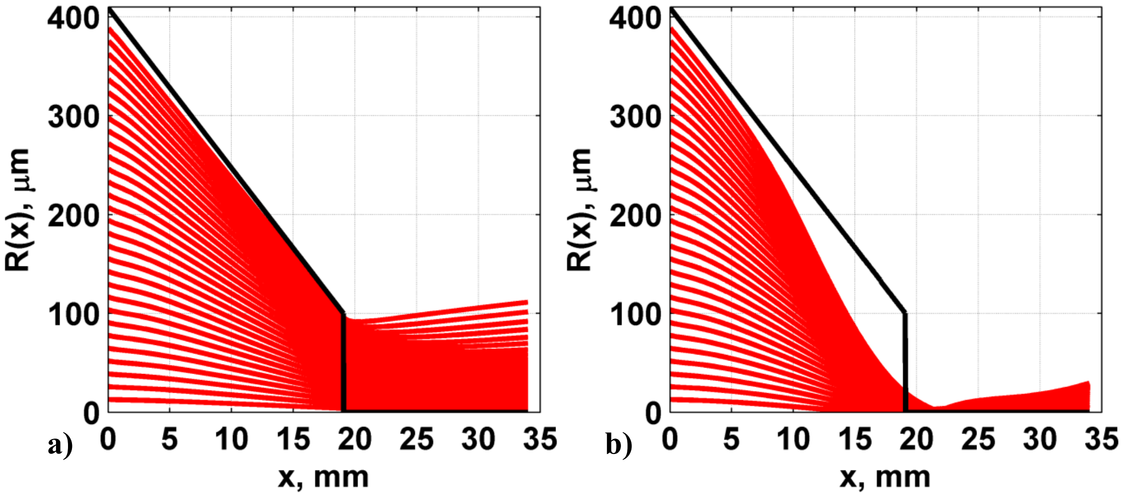

Figure 22. Simulation of 3.8 μm silica aerosol particles flowing through a 200 μm linearly converging nozzle with a) Stokes force, and b) Stokes and Saffman force, reprinted from Lutfurakhmanov [80].

5. EXPERIMENTAL VALIDATION OF AEROSOL PHYSICS

The theoretical modeling of the fluid-particle interactions of aerosols is an invaluable tool in predicting the focusing of aerosol particles. The accuracy of the models and subsequent predictions must be verified by experimental observations before a complete understanding of the physics of aerosols and ensuing improvement in A-DW techniques are realized. Much work is published on methods of quantifying aerosol focusing indirectly by measuring the width of deposits on a substrate. Rao et al [94] and Mallina et al [60] for example used a greased substrate to capture aerosol particles and approximate the beam width. Fuerstenau et al [86] and Akhatov et al [82] directly measured the aerosol beam width by imaging the scattered light from aerosol particles exiting an orifice and nozzle, respectively. Much like the deposited line on greased plates, the images obtained from the scattered light create a histogram of the aerosol particle locations during the image integration time where information about individual particle trajectories and how focusing occurs for these particles is not directly known.

5.1. Measurement of Nozzle Geometry

Ceramic nozzles were used for much of the printing using Aerosol Jet. These nozzles are available from CoorsTek (formerly Gaiser Tool). Commonly available nozzles include 100, 150, 200, and 300 μm outlet diameters, and lengths of 11.1 mm and 19.05 mm. The outside diameter of the nozzle is 1/16 in. but the inlet diameter and the internal geometry are not specified. To determine the actual geometry, a 100 μm nozzle was ground in half using a polishing wheel. It can be seen from the microscope pictures in Figure 23 that the nozzle has a decreasing diameter of approximately 800 μm to 100 μm.

More information was necessary to accurately model the geometry of the walls inside the nozzle, but a rough approximation of a linearly decreasing nozzle as shown in Figure 24 was thought to be a reasonable assumption.

Figure 23. Ceramic 100 µm nozzle cross section. The geometry of a 100-µm nozzle can be seen above. This figure displays different cross sections of the nozzle at different magnifications. The scale can be seen on the picture. The inlet to the nozzle is on the left, while the outlet is on the right.

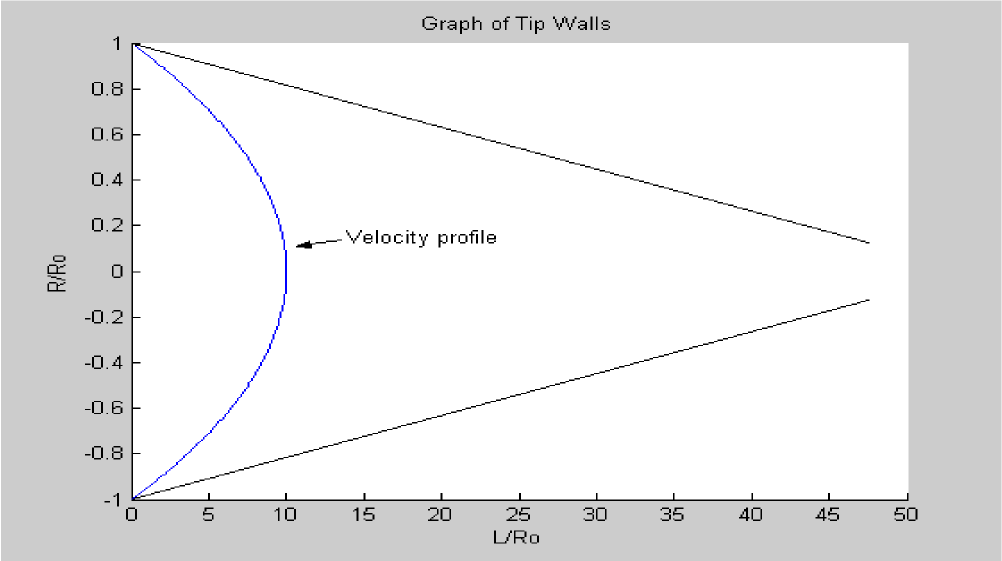

Figure 24. Linearly converging geometry assumed for initial experiments using ceramic nozzles. Velocity profile inside nozzle. Initial Poiseuillian velocity profile is displayed in blue.

To obtain the nozzle geometry more accurately, the ceramic nozzles were visualized with a Dage XD7600NT x-ray imaging system. The main advantage of this imaging system is that it has the ability to visualize the details of the internal structure of the nozzle without destroying it. The first image is seen below in Figure 25 where the rough structure of the nozzle can be easily visualized. In this figure, the near-linear geometry of the nozzle is clearly visible, with a decreasing diameter towards the exit of the nozzle. In Figure 26, the geometry at the exit of the nozzle can be determined. Notice that the nozzle is not perfectly linear at the immediate exit. Rather, the nozzle has a short straight section followed by a chamfer leading to the exit of the nozzle.

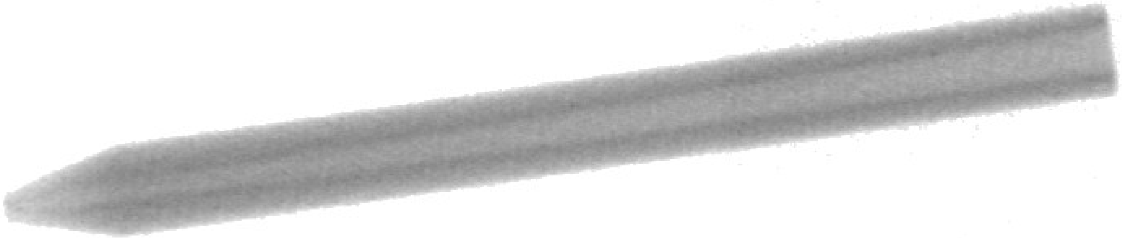

Figure 25. X-ray image of 100-μm nozzle, reprinted from Akhatov et al. [8], Copyright 2008, with permission from Springer.

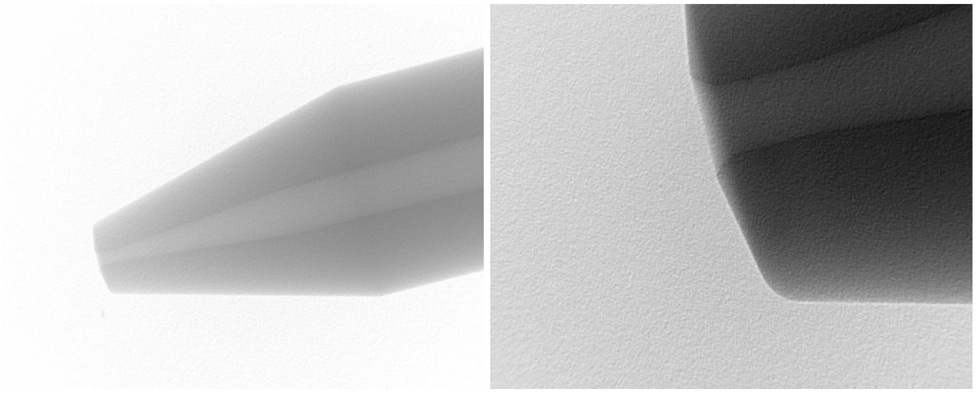

Figure 26. X-ray imaging of exit of 100-μm nozzle, reprinted from Akhatov et al. [8], Copyright 2008, with permission from Springer.

After thorough analysis of the x-ray images, it was determined that the nozzle was in-fact not linearly converging as was previously assumed, rather the nozzle consists of a slowly converging geometry followed by a more abrupt convergence near the end of the nozzle. The short straight section and chamfer still exists as first thought. The geometry assumed for a 100 μm nozzle is shown in Figure 27, where 1 μm silica particles (red) and 1.5 μm liquid particles are shown.

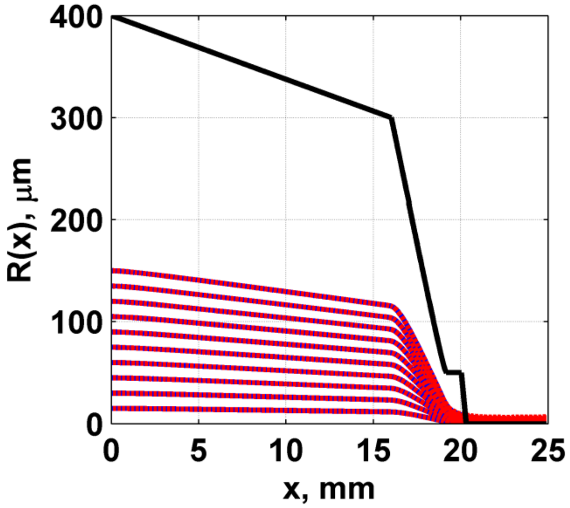

Figure 27. Nozzle geometry for 100 μm ceramic nozzle with 1μm silica particles (red), and 1.5 μm liquid aerosol particles (blue), reprinted from Lutfurakhmanov [80].

During normal operation, the nozzles can become clogged with ink. This is especially prevalent in the 100 μm nozzle. Clogging generally occurs near the exit, creating a plug in the nozzle. The clogging of a 100 μm nozzle is apparent in Figure 28. Clogging is especially prevalent when sub-optimal flow parameters are used.

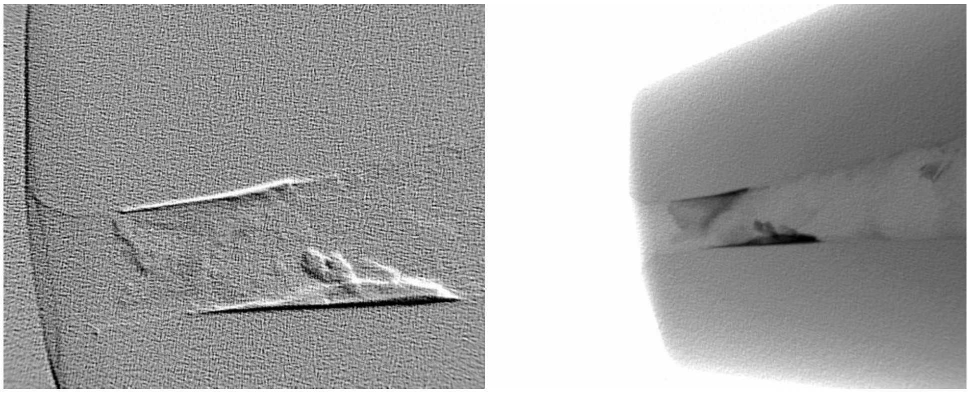

Figure 28. X-ray image of a 100-μm clogged nozzle.

The ceramic nozzles mentioned above were easily obtainable, but lacked a simple geometry for modeling. Different nozzle geometries could however be obtained using a wire Electric Discharge Machined (EDM) tungsten carbide nozzle. Nozzles of linearly converging shape or constant diameter can be made easily with this tool. One specific nozzle made had a length of 19.05 mm, outside diameter of 1.49 mm, inlet diameter of 820 μm, and outlet diameter of 220 μm. Other nozzles were made and will be briefly described in section 5.5.

5.2. Aerosols for Characterization

To accurately characterize the features of aerosol beams, one must know the size of the aerosol particles. Initial experiments used liquid aerosols as described in section 2.4, but a more controllable particle size would allow for simpler characterization of the aerosol beams. Near-monodisperse silica particles from Cospheric Inc. (Santa Barbara, CA), with particle sizes of 3.8 μm, 1.15 μm, 0.62 μm and coefficient of variation less than 10% were sourced. These particles are near-spherical and have a density of 1,800 kg/m^3. An SEM image of the 3.8 μm particles along with a histogram of particle size is shown in Figure 29. The particles in this image were deposited on double-sided carbon tape and are somewhat submerged into the tape. Mean particle size was measured to be 3.81±0.22 μm. The distribution shows what appears to be a bimodal distribution, so both the mean particle size and distribution will be taken from the manufacturers specifications.

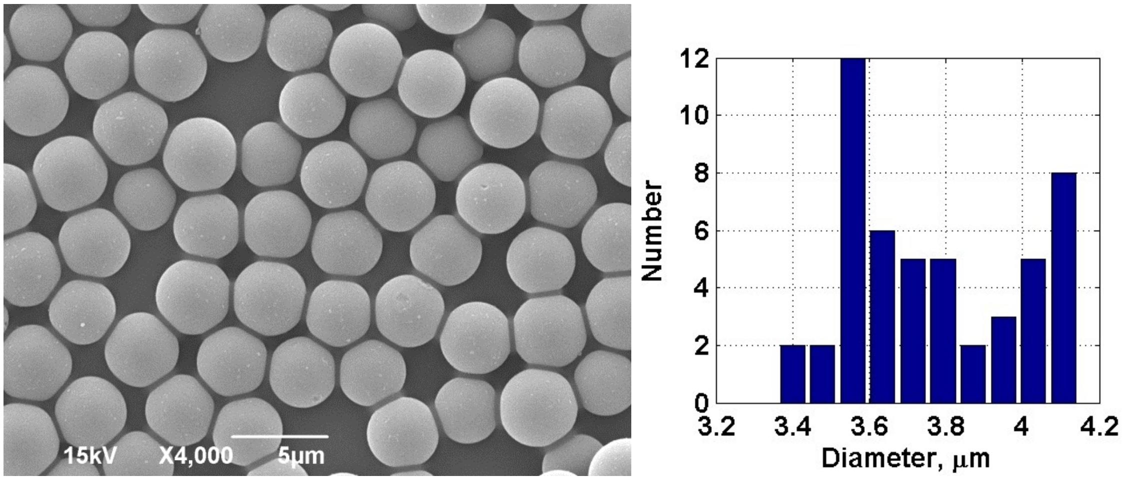

Figure 29. SEM image of 3.8 μm silica particles, and histogram of particle size.

To aerosolize these particles, a low flow rate powder feeder is needed. The powder feeder is shown below in Figure 30. Agitation is achieved in two ways 1) by using an electromagnetic solenoid driven by an oscillating circuit, and 2) high velocity gas flow by a 75 μm nozzle. Gas enters through a center tube, Figure 30, and is accelerated through the nozzle and then impinges on the powder (loadings as small as 150 mg) which is sitting in a small reservoir in the bottom of the container. The powder is aerosolized and exits coaxially through the side of the system. Experiments have shown that gas flow rates as low as 30 ccm have provided sufficient aerosolization.

5.3. Mie Scattering for Aerosol Beam Widths

The first method to view aerosol particles is by using Mie scattering. This section outlines this first set of experiments done using liquid aerosols which was published in the

Journal of Aerosol Science in 2008 [82]. The aerosol particle focusing in the micro-capillary can be quantified by the width of the aerosol beam after exiting the capillary without monitoring the trajectories of individual particles. The aerosol beam leaving the micro-capillary was visualized using scattered laser light imaged with an Olympus BX60M microscope as depicted in Figure 31. The micro-capillary was rigidly held in place using a 3-axis linear micro-positioner (Newport SDS65 linear stages), mounted to the microscope. The micro-positioner made focusing on the aerosol stream simple and provided distance measurements from the capillary exit. Long-working distance objectives, with magnifications of 50× and 100×, allowed focusing on an aerosol stream as small as ~2 μm. A diode pumped solid state (DPSS) 532 nm frequency doubled Nd:YAG laser with a maximum output of <200 mW was directed perpendicularly through the aerosol beam near the capillary end and then into a Kentek ABD-2NP laser beam dump.

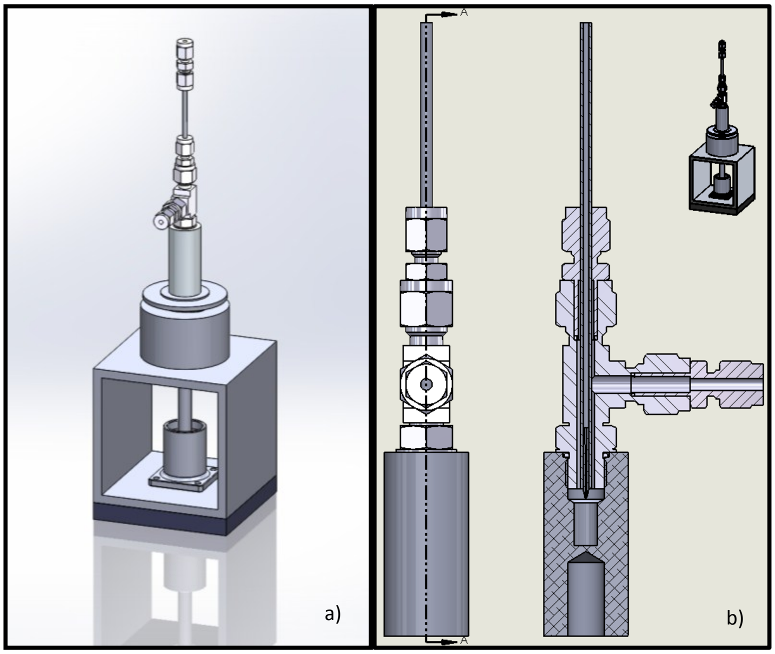

Figure 30. Diagram of solid powder atomizer; a) overview, b) cross section, reprinted from Robinson [106].

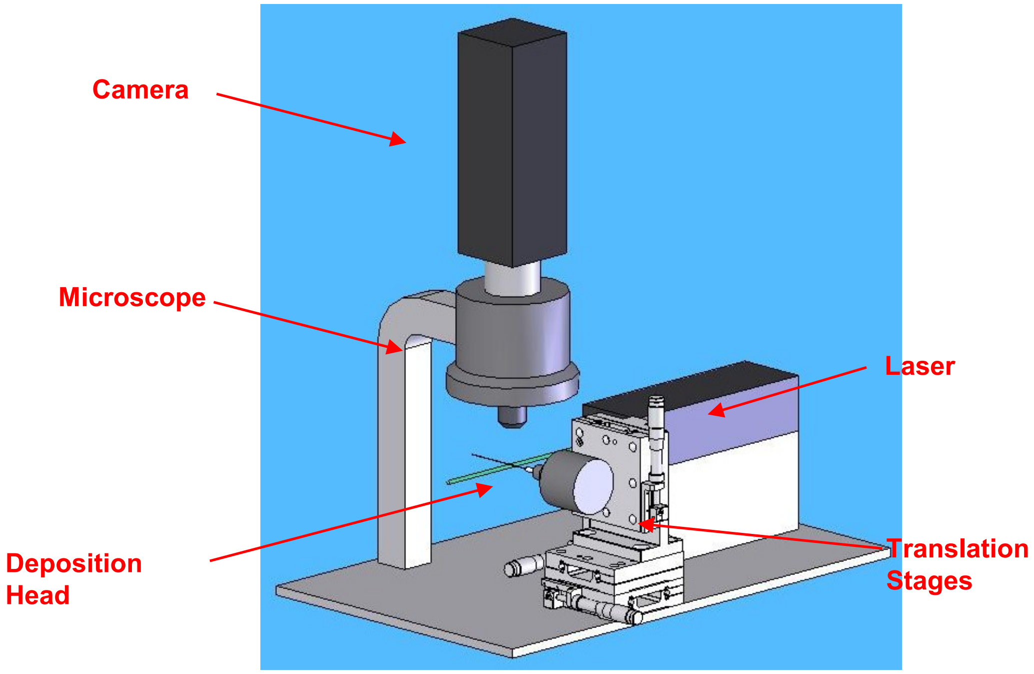

Figure 31. Diagram of first experimental apparatus for visualization of the aerosol beam exiting a micro-capillary using Mie scattering, reprinted from Akhatov et al. [82], Copyright 2008, with permission from Elsevier.

The beamwidth was determined at 0.25 mm intervals from the capillary exit. A total of nine repetitions were carried out on different days to determine the beamwidth deviation due to time variability. Data was taken via a Sony ExWave HAD CCD camera which records 640X480 pixel pictures. The pictures were then transferred to MATLAB where they were normalized and the beamwidth measured using full-width-at-half-max intensity. The beamwidth at ten different pixel locations around the center of each picture were determined, and the average of these ten was taken as the beam width at that respective distance.

A picture of the aerosol beam emanating from the micro-capillary is shown in Figure 32 which qualitatively shows the focusing of the aerosol beam. Figure 33 is a higher magnification picture of the particle stream near its focus at 1.75 mm from the nozzle exit where the beam width is only 5 µm wide with a standard deviation of 2.1 µm.

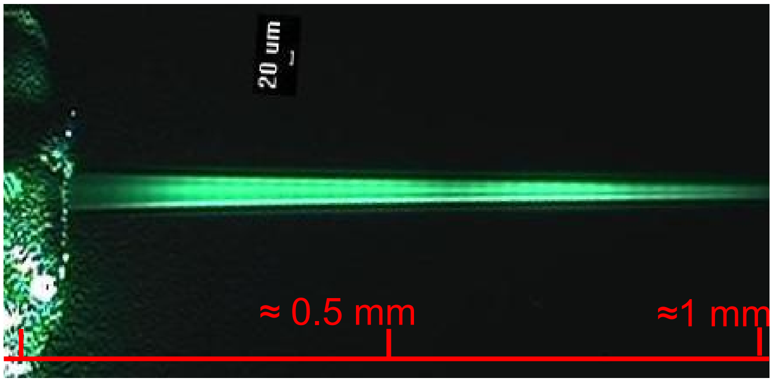

Figure 32. Laser-illuminated aerosol beam exiting a 100 µm micro-capillary, reprinted from Akhatov et al. [82], Copyright 2008, with permission from Elsevier.

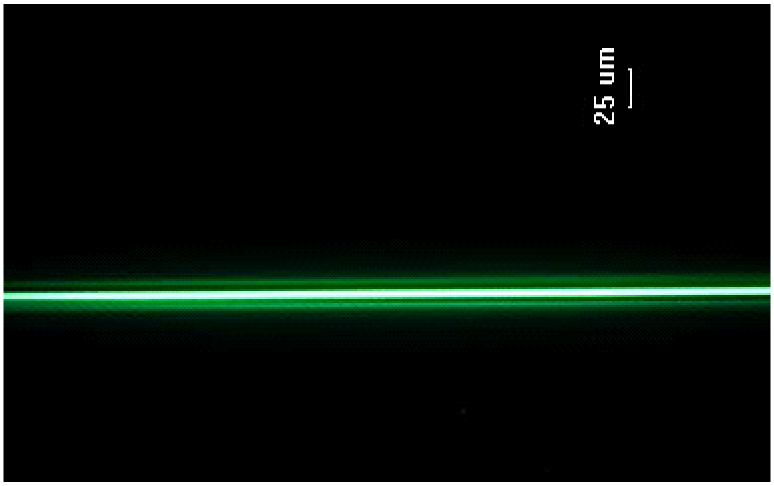

Figure 33. Aerosol beam 1.75 mm from the end of a 100 µm micro-capillary (approximate FWHM beam width is 5 µm), reprinted from Akhatov et al. [82], Copyright 2008, with permission from Elsevier.

Both a 200 µm and 100 µm ceramic nozzle were briefly analyzed at a given flow rate. The flow rate was as follows: 100 µm diameter- 30 ccm carrier flow, 10 ccm sheath flow; 200 µm diameter- 30 ccm carrier flow, 50 ccm sheath flow. These flow rates are common for the Aerosol Jet printing process. Beamwidth, for both the 100 µm and 200 µm nozzles, as a function of distance are presented in Figure 34. The black bars represent the standard deviation for each measurement. Notice that the focusing of the aerosol particles definitely occurs outside of the nozzle. In fact, focusing of the aerosol beam from the 100 µm nozzle occurs at approximately 2 mm and at 2.5 mm for the 200 µm nozzle.

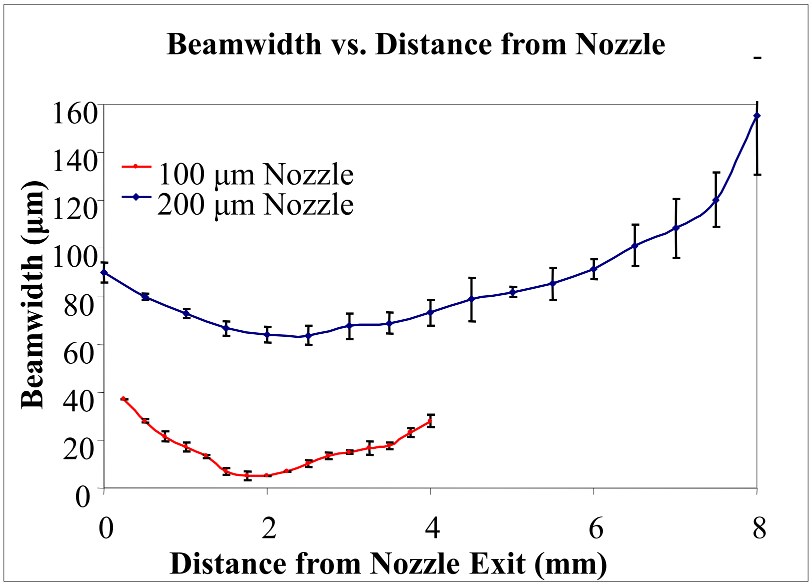

Figure 34. Beamwidth vs. distance from nozzle for liquid aerosols, and ceramic micro-capillaries of 100 µm and 200 µm exit diameter.

During experiments, there were two issues with measuring beam width. The first is that the particle beams tended to move with time causing the aerosol beam width to appear larger than it actually was. This was especially noticed on nozzles with very small beam widths (< 10 µm). The second issue was that beam widths at 1 mm from the nozzle exit were difficult to measure due to the large amount of scattering affecting the image noise.

The previous algorithm to measure beam width was modified to fix these two problems. First, when taking beam width images, 100 total images were acquired. Then, the images are normalized and 20 rows of pixels are averaged together for each image.

Beam width, and the center of the beam is calculated for each image. If the calculated center is off by more than a specified value (10x the pixel size), that image is discarded. Then the remaining beam widths are averaged together to result in the final beam width. The movement of the beam is generally within ± 1 µm, but if the beam width is below 10 µm, this will cause up to a 10% error in measurements. One example of the moving beam center is shown in Figure 35 where a) the beam center vs. time and b) a Fast Fourier Transform (FFT) spectra are shown. It is clear that there is a resonant vibration in the system which causes the beam to deviate, but the removal of this is not practically possible and should not create an issue with measurements so long as the beam width is calculated from the average of individual images rather than the beamwidth of an average of 100 images. For reference, the updated Matlab code used for beam width measurements can be found in the Appendix.

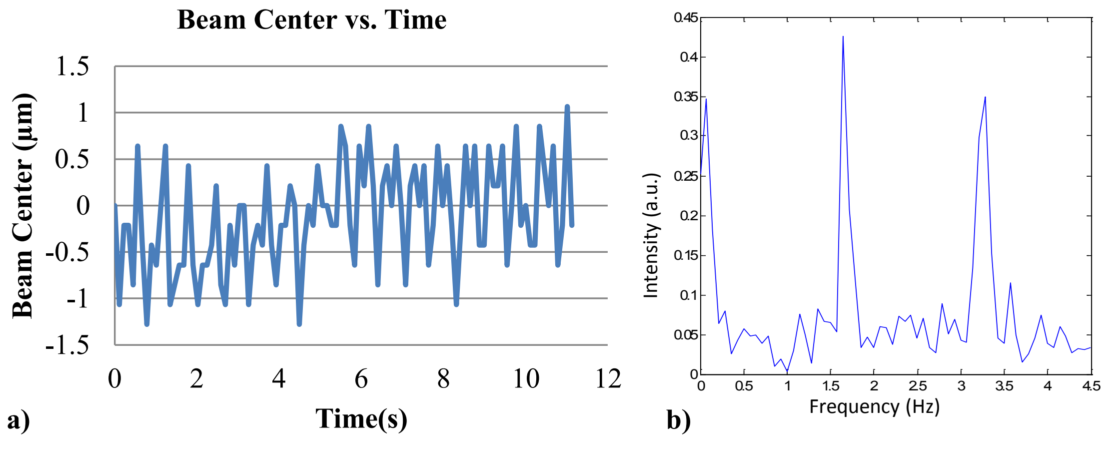

Figure 35. Graph of a) aerosol beam center vs. time, and b) FFT spectra of beam center.

5.4. Characterizing Aerosol Beams Using Shadowgraphy

Particle image velocimetry (PIV) using a scattered laser light sheet with seeded aerosol particles is commonly used to determine the trajectory of a fluid flow field at macroscale dimensions, but PIV is not designed for individual aerosol particle tracking and requires a very dense aerosol which is extremely difficult to implement at the micro scale.

We implemented a shadowgraph method to determine trajectories of individual particles focused by a nozzle [107]. This work is detailed in Mike Robinson's Master's Thesis [106], but a summarized description will be given. A PIV system with shadowgraph option available from La Vision Inc. was used to measure the aerosol particles exiting a linearly converging nozzle. A schematic of the system is shown in Figure 36. Illumination is provided by a pair of Nd:YAG pulsed lasers, that pump a dye to produce incoherent light that is transmitted through a liquid fiber guide, and collimated with a Fresnel lens. The aerosol stream is placed between the camera and light source and produces shadow images on the camera. For alignment and comparison to previous results with scattered light, a CW laser is also incorporated into the system. This system is advantageous in that it is capable of measuring the particle location, velocity, and size simultaneously.

Results of these measurements are shown in Figure 37 a, b, and c, where a) particle size distribution; b) average, minimum and maximum particle velocity vs. distance from the nozzle exit; and c) beam width from light scattering and number of particles from shadowgraph vs. the radial position (focus) are displayed. In this case, the particle size distribution from an ultrasonic atomizer measured using the DaVis software has a mean diameter around 2.5 µm, well within the assumed range for modeling of 0.5 to 5 µm. It should be noted that this particle size distribution is only an example and is below the range (5 µm) as advertised to be accurately sized. Particle velocities are shown to increase up until about 1 mm away from the nozzle. Finally, the beam width of the aerosol particles measured by the CW laser and by shadowgraph is very similar. Results of all these measurements show the validity of the shadowgraph method to characterize the aerosol stream exiting a nozzle for particle size, velocity, and distribution. Future results will allow additional refinement of fluid-particle forces giving a more accurate model for predicting aerosol focusing [107].

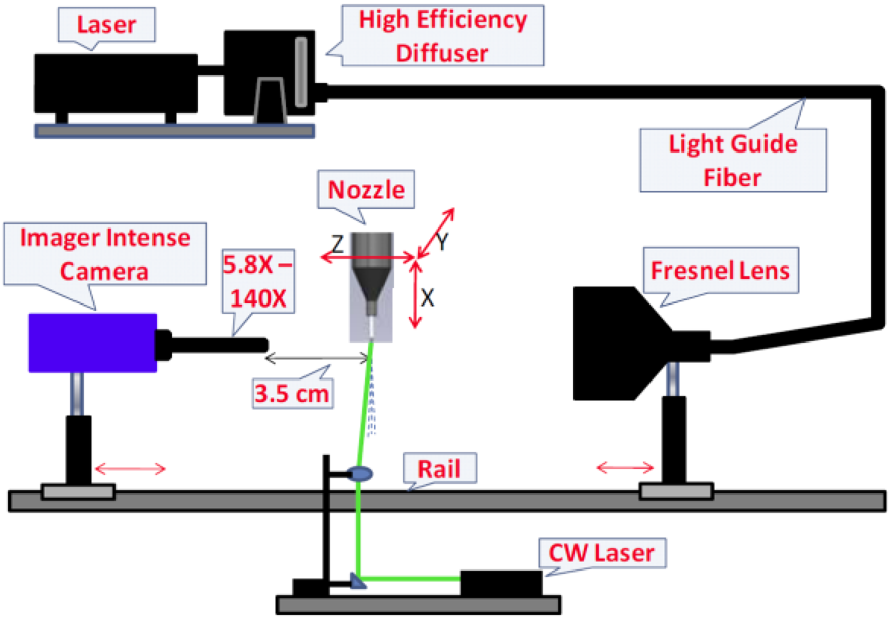

Figure 36. Schematic of shadowgraph system for the measurement of aerosol particles, from Mahmud et al. [107], Copyright 2010 ASME. Reprinted with Permission.

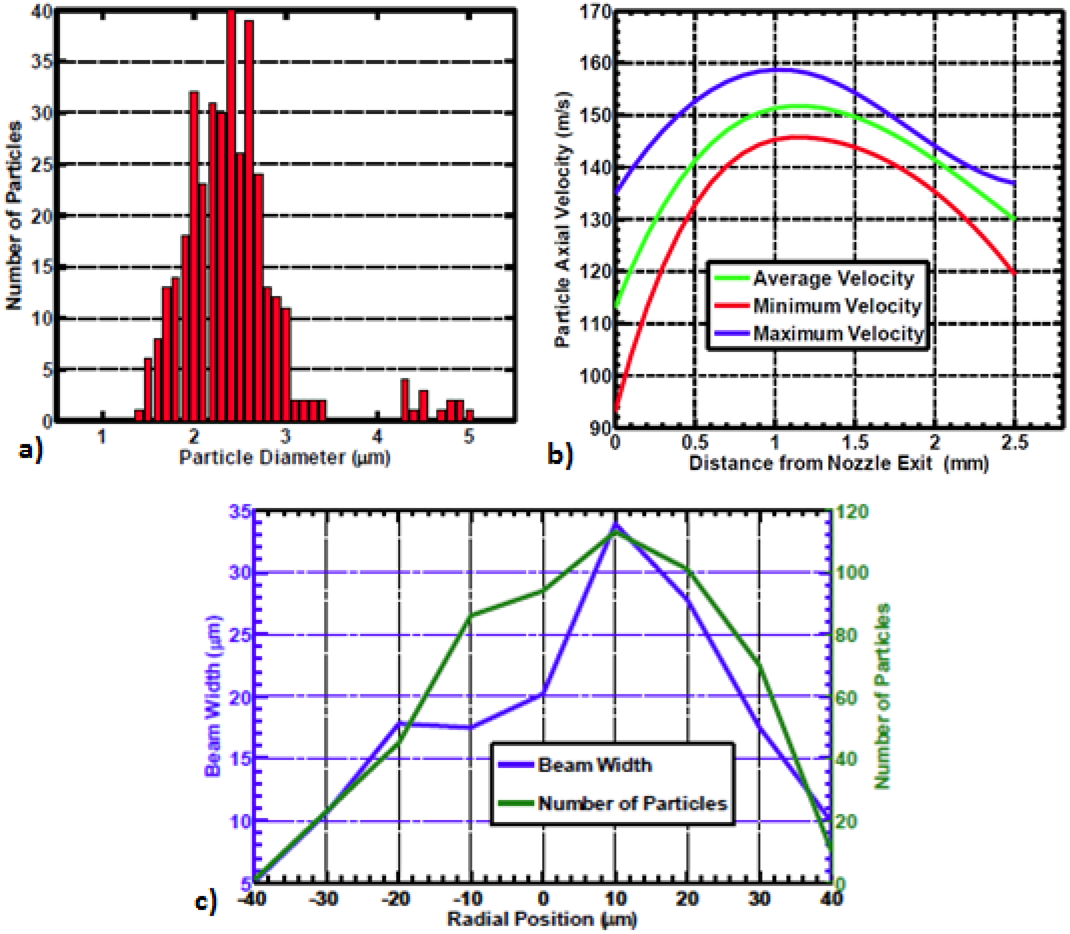

Figure 37. Shadowgraph results showing a) histogram of particle size, b) particle velocity vs. distance from the nozzle exit, and c) CW laser beamwidth and number of particles from shadowgraphy vs. radial position (focus), from Mahmud et al. [107], Copyright 2010 ASME. Reprinted with permission.

Shadowgraphy offers the ability to determine a large amount of information about an aerosol beam, as already discussed, but for the size of aerosol particles used in these experiments, the algorithms to determine particle size and the position of the particle in the depth of field (z-axis) are somewhat limited. Mike Robinson developed an algorithm denoted as the Small Particle Sizing Algorithm (SPSA) [106, 108] which is reasonably capable of sizing and positioning aerosol particles. The algorithm for sizing aerosol particles works by evaluating the image size and image slope of a particle from a shadowgraph and comparing to calibration curves developed using particles of known size. Once particle size is determined, particle location in the depth of field can also be found using similar calibration curves. The end result from this algorithm would be that if an aerosol beam were visualized from shadowgraphy, information about particle velocity, size and position in 3-dimensions would be known. Although this algorithm is mostly complete, further testing is still required to determine the applicability to aerosol particles of different composition such as liquid particles or silica particles.

5.5. Comparison of Theory and Experiments

Initial comparisons to theory and experiment were first detailed in my master's thesis. In these results it was assumed that the nozzle was linearly converging, which led to the conclusion that the only way theory and experiment could compare to each other was if 1) both Stokes and Saffman force were introduced, 2) the aerosol diameter was artificially small (0.42 μm). In light of more recent findings on the actual geometry, these conclusions may have not been entirely correct. The most recent results will now be summarized.

Two methods of determining aerosol beam width have been described. Measuring the beam width using the Mie scattering is far quicker that using shadowgraphy, but should only be used if the beam width can be confirmed similar for both methods. A comparison of the shadowgraphy beam width and that using the CW laser (Mie scattering), along with the theoretical beam width calculated with and without Saffman force applied for a 220 μm linear converging nozzle with 3.8 μm silica particles is shown in Figure 38. The beam widths for both shadow and CW data compare very well until 5-6 mm past the nozzle exit. It should be noted here that inlet conditions for the simulation assume the aerosol particles occupy 32% of the inlet diameter. A range of 30 to 50% have been experimentally seen.

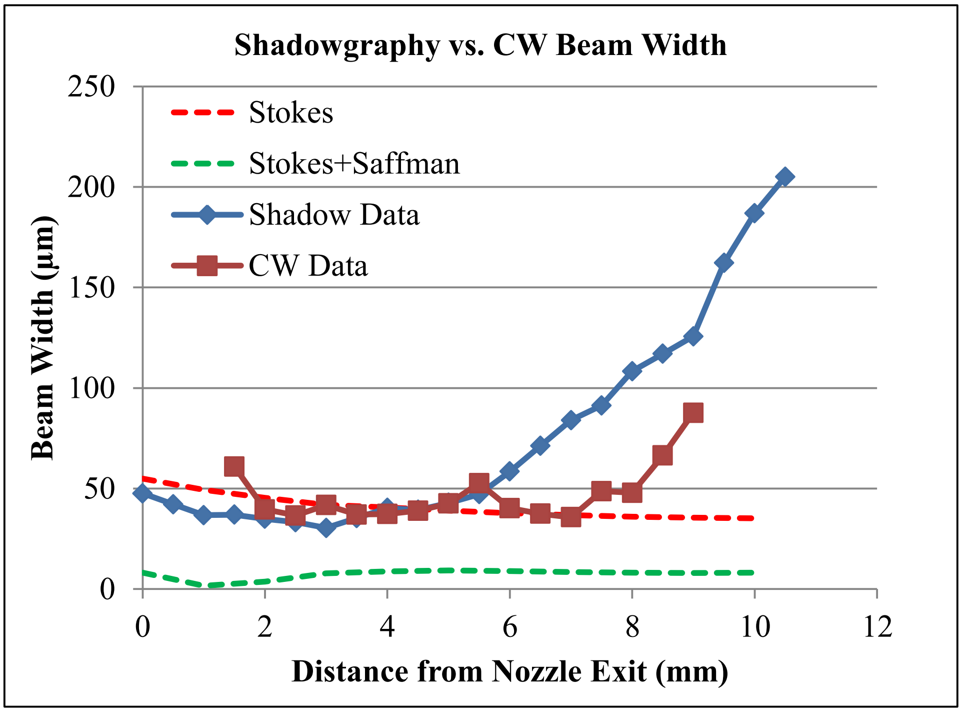

Figure 38. Beam Width comparison for 220 µm linearly converging nozzle with 3.8 µm silica particles.

From these results, it is apparent that using the CW beam width data is an acceptable practice as long as 1) the beam width at the nozzle exit is not needed, and 2) beam widths past 6 mm from the nozzle are unnecessary. Also shown in this graph is the clear under-prediction of beam width when Saffman force is used, while beam width is very near the same for the model which accounts for only Stokes force. This initial finding may seem to suggest Saffman force is not acting on the aerosol particles in this particular situation and is no longer needed in the simulation.

After looking closer at the data, it was thought that one possible explanation for not needing Saffman force in these particular simulations is that the corrections used are not completely appropriate for our application. The corrections we use right now are from Dandy and Dwyer [81], Equation (28), and are not designed for the range of Reynolds number and compressibility that are being simulated, so it seems natural that an adaptation to their corrections may be needed. A rough way to do this is by multiplying the corrected Saffman force by a constant. To determine this constant, a comparison of theory to experiment must be undertaken where Saffman force is accentuated. The geometry must be something easily obtainable from nozzle manufacturers with a known geometry. For this comparison, a linearly converging nozzle, 19.05 mm long with inlet and outlet diameters of 820 µm and 220 µm, is connected to a straight nozzle, with length of 30 mm, and diameter of 264 µm. A simulation of this geometry using a flow rate of 120 ccm with 3.8 µm silica particles as shown in Figure 39 reveals that particles focused using only Stokes force (blue) are collimated but at a rather wide beam width, where particles focused using both Stokes and Saffman force (red) are not only collimated but very near the centerline. This geometry should be an excellent example for creating a correction to Saffman force because there is such a large difference in aerosol beam widths due to the addition of Saffman force. If the experimental beam widths happen to match that of Stokes force only, then it would be apparent that Saffman force is not applicable for this flow regime.

Experimental beam widths were measured using Mie scattering, with 3.8 µm silica particles. A total of 3 experiments were done, with measurements taken at 1 mm increments and averaged over the 3 sets. Beam width results at FWHM for the experiment as well as for the simulation with and without Saffman force applied are shown in Figure 40. Results reveal that the experimental beam width (~7 µm) is between the model for

Stokes force (~55 μm) and that with Stokes and Saffman force (~2 μm). This result gives credence to the necessity for an additional correction factor.

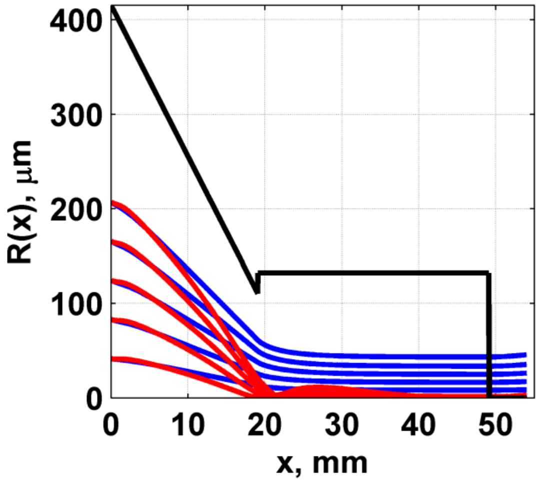

Figure 39. Graph of linearly converging to straight nozzle displaying trajectories of aerosol particles with Stokes force (blue) and Stokes and Saffman force (red) applied.

Introducing different correction factors to Saffman force greatly affects the calculated beam width by decreasing beam width with increasing strength of Saffman force. The change in Saffman force and how it compares to the experimental data is shown in Figure 41 where; a) a graph of the beam width vs. the distance from the nozzle is shown; b) a graph of the average beam width from 0-5 mm from the nozzle exit vs. the correction to Saffman force. For this specific instance, the best fitting correction to Saffman force is a multiplication of 0.19. Both the average beam width (dotted line in Figure 41b), and the shape of the beam width are in good agreement. For convenience, this constant of multiplication is assumed correct; however a more thorough investigation of this correction is warranted to determine if there is a correlation of this correction to the Reynolds number of the particle.

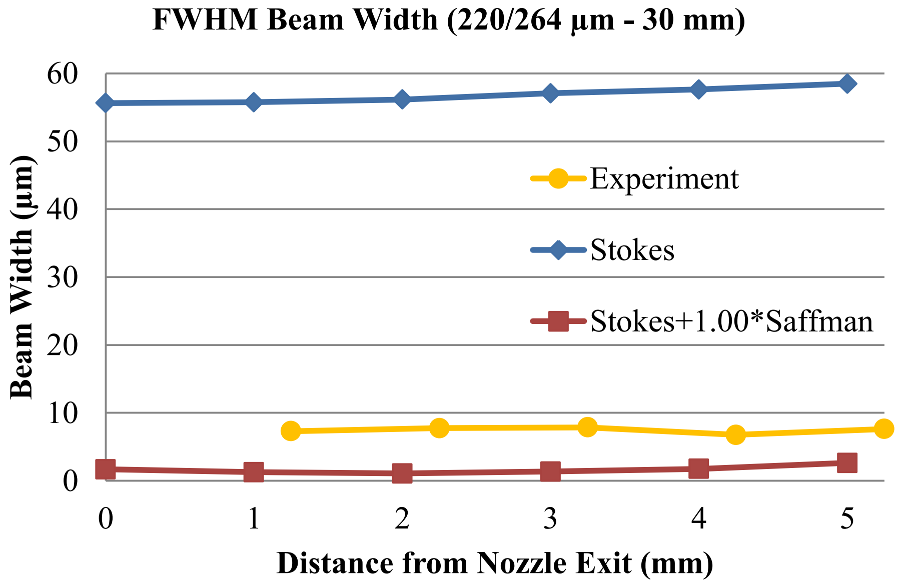

Figure 40. Beam width vs. distance from the nozzle for experiment and modeling using 3.8 µm silica particles through a 220 µm linearly converging nozzle with 30 mm long 264 µm diameter straight section.

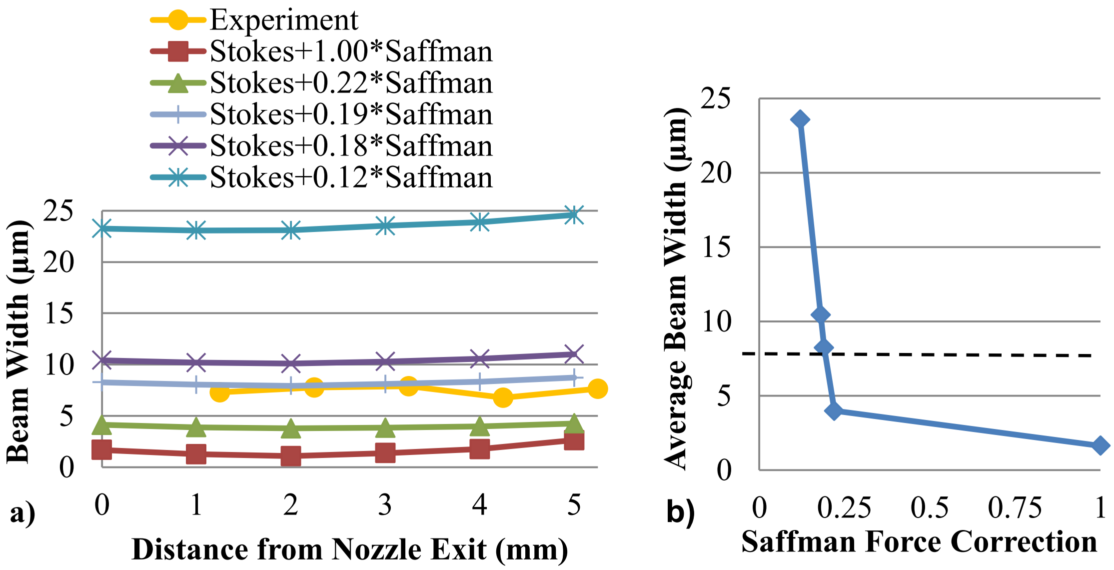

Figure 41. Graph of a) beam width vs. the distance from the nozzle (no, Saffman force and Saffman force multiplied by a correction factor) and b) average beam width from 0-5 mm from the nozzle exit vs. the correction to Saffman force.

In the previous results using converging nozzles we had come to the hypothesis that Saffman force was not accurately modeled and may not be necessary. After confirming with the linearly converging-straight nozzle design that Saffman force needs a correction of 0.19, the converging nozzle may now be revisited. Beam width for a 175 µm ceramic nozzle is shown in Figure 42 where flow rate was 120 ccm with 3.8 µm silica particles. Both the experimental beam width and theoretical beam width are shown. From these results it can be seen that the results with the 0.19 corrected Saffman force are very similar to those of the Stokes force only simulated beam width. Although the simulated beam widths are not the same shape as the experimental beam width, they are reasonably close, when considering standard deviation (black bars). These results do show that there still may be a small error in predicting the shape of the ceramic capillary but the geometry known should be sufficient for these simulations.

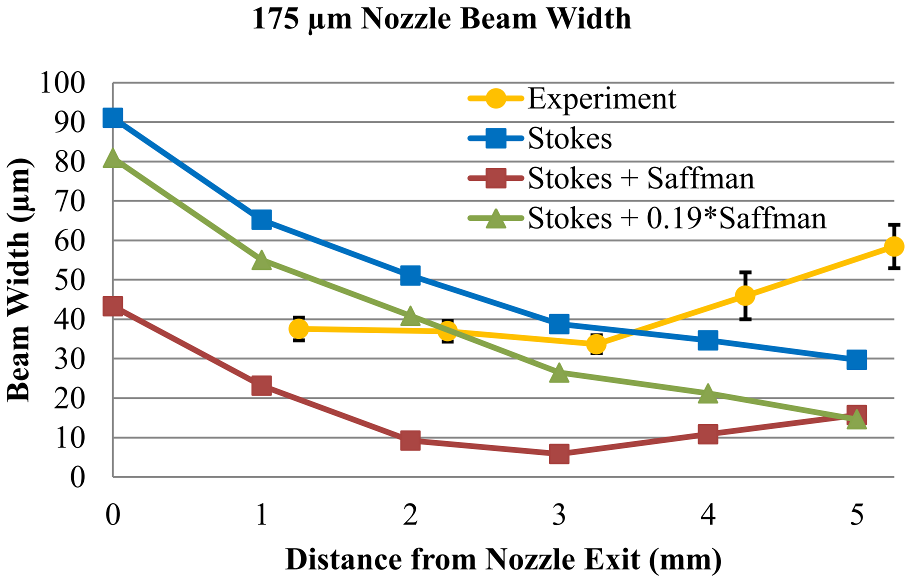

Figure 42. Graph of experimental and simulated beam width vs. distance for 175 µm ceramic nozzle. Flow rate is 120 ccm using 3.8 µm silica particles.

5.6. Collimated Aerosol Beam Direct Write

Collimated Aerosol Beam-Direct Write (CAB-DW) is one of the technologies we developed at NDSU [9, 109] during this research, and consists of a three-component converging-diverging-converging nozzle (Figure 43) capable of reducing depositions from the Aerosol Jet system to 5 μm by further collimating and focusing the aerosol beam. Other characteristics of CAB-DW are nearly identical to that of Aerosol Jet. The ability to develop an improved nozzle design was only realized after an extensive experimental-analytical analysis was performed on the Aerosol Jet system. Aerosol particles entrained in the nozzle were modeled using a Lagrangian tracking scheme in Poiseuille flow through a linearly converging nozzle using Stokes and Saffman forces of fluid-particle interaction. The trajectories of individual particles were calculated and the aerosol beam width exiting the nozzle was determined after summing the trajectories of several particles exiting the nozzle. The idea to develop this shape nozzle came about due to the modeling predictions which at first appeared to show a nearly perfectly collimated aerosol beam. After further work, it was shown that that initial model was incorrect, but that the nozzle still had significantly thinner beams.

The aerosol beam width was experimentally determined by measuring the intensity of scattered laser light from the aerosol beam emanating from the nozzle using a CCD camera and microscope. The theoretical beam width (measured at full-width half-max, FWHM) was then compared to experiment, with both theory and experiment similar after adjustment of predicted particle size and corrections to the forces of interaction. After the analytical model was developed, new nozzle geometries were input to the model, with corresponding beam widths calculated. The 3-component nozzle appeared to have a much better collimation and focus theoretically and was chosen for experimental verification. Calculated trajectories of 4 μm silica particles through the CAB-DW nozzle at a flow rate of 40 ccm are shown below in Figure 44 where blue lines represent both Stokes and Saffman force applied to the particles, and red lines where only Stokes force is applied.

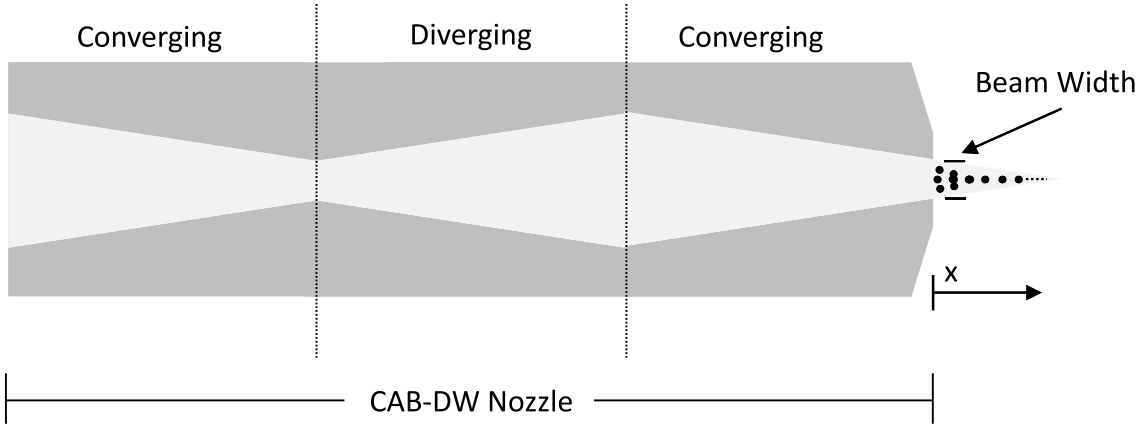

Figure 43. Illustration of 3-component converging-diverging-converging CAB-DW nozzle and measurement of aerosol beam width, reprinted from Hoey et al. [17].

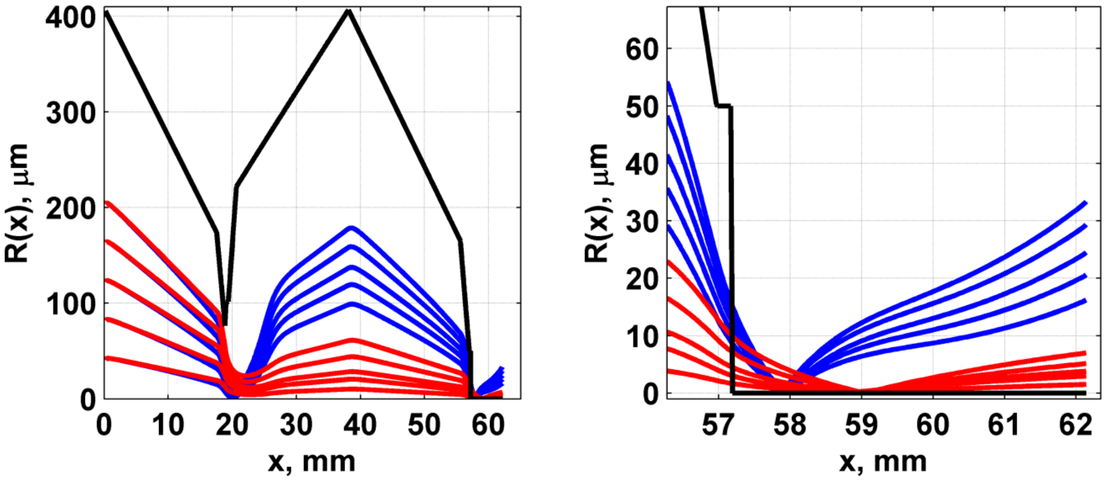

Figure 44. Calculated trajectories of 4 μm silica particles through CAB-DW nozzle with Stokes and Saffman force applied (blue), and only Stokes force applied (red), reprinted from Lutfurakhmanov [80].

The beam width from the CAB-DW nozzle was measured and compared to the single nozzle (Aerosol Jet, conventional aerosol spray) as illustrated in Figure 45. In this case the CAB-DW nozzle provided for a much more collimated and focused beam with a minimum beam width of 1.9 µm at 2 mm past the nozzle exit as compared to 5.0 µm at 1.8 mm past the nozzle exit for the conventional aerosol spray (Aerosol Jet) [110]. Additional beam widths of CAB-DW are displayed below in Figure 46. These beam widths are for 3.8 µm silica particles and modeled using Stokes force and 0, 0.19, or 1.0 times Saffman force applied to the particles with an assumption that the particles entrained 50% of the inlet. Experimental beamwidth is calculated using CW data results. Beam widths look very thin, although not as thin as with the liquid aerosol. It can be seen that in this case the use of Saffman force at 100% intensity does not resemble the experimental results.

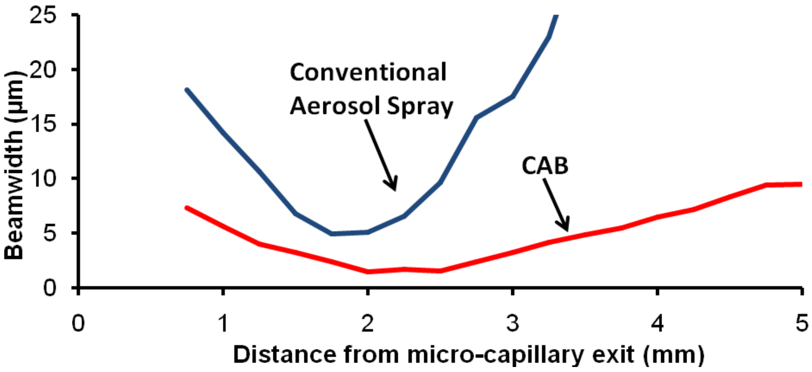

Figure 45. Graph of experimental aerosol beam width vs. distance from the nozzle exit for 1) Aerosol Jet (conventional aerosol spray) and 2) CAB-DW, from Schulz et al. [110], Copyright 2010 IEEE.

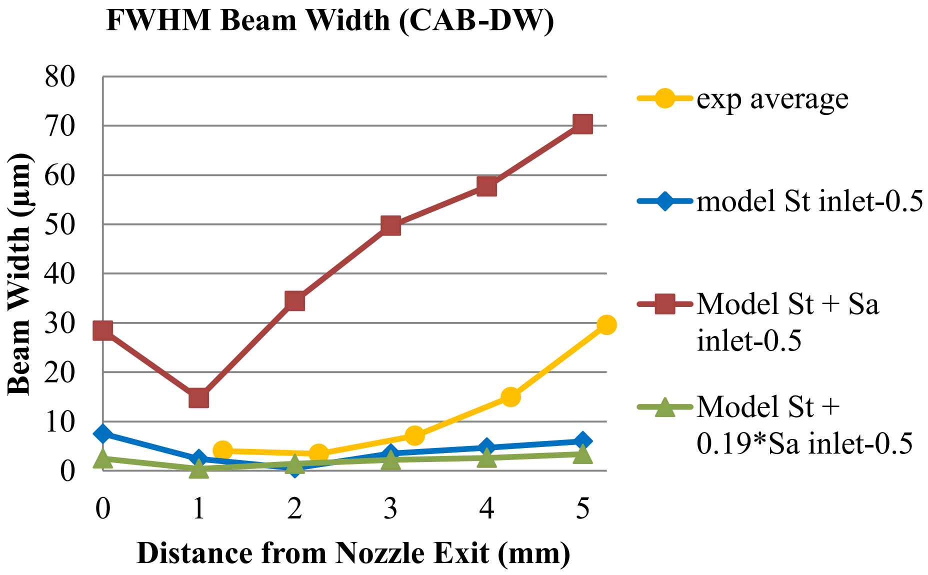

Figure 46. Beam widths vs. distance from the nozzle for CAB-DW with theoretical model, and CW laser experimental results.

5.7. Converging-Straight Nozzles

The beam widths through a linearly converging-straight nozzle was already discussed in section 5.5, where a correction to Saffman force of 0.19 was determined to be an accurate approximation. In this section, beam width results for other converging straight sections will be discussed. In this case, a 175 µm converging ceramic capillary is connected to a straight section of 200 µm diameter, and lengths of 11.84 mm, 17 mm, and 30 mm. Beam widths were measured using 3.8 µm silica particles with a flow rate of 120 ccm. Results for the 11.84 mm long converging section are shown in Figure 47. From the graph, one can see that the beam width is thin, and that the model which uses the correction for Saffman force or 0.19 compares well to the experimental results. Results for a 17 mm long straight section are shown in Figure 48. These results are interesting in that the beam width is slightly over-predicted. In the 30 mm long straight section (Figure 49) the model with Saffman force multiplied by 0.19 again matches very well to the experimental results. For all of these graphs the model with Stokes force and that with Stokes and Saffman force are also shown for reference. It can be seen though that the best fit overall is produce from the 0.19 corrected Saffman force model.

A graph of the beam width of the 0.19* Saffman vs. length of the straight section of the nozzle for the 175 µm to 200 µm straight section as compared to experimental results at 2 mm from the nozzle exit is shown in Figure 50. It is clear that the model and experiment are very closely matching, confirming the correction to be appropriate to these simulations.

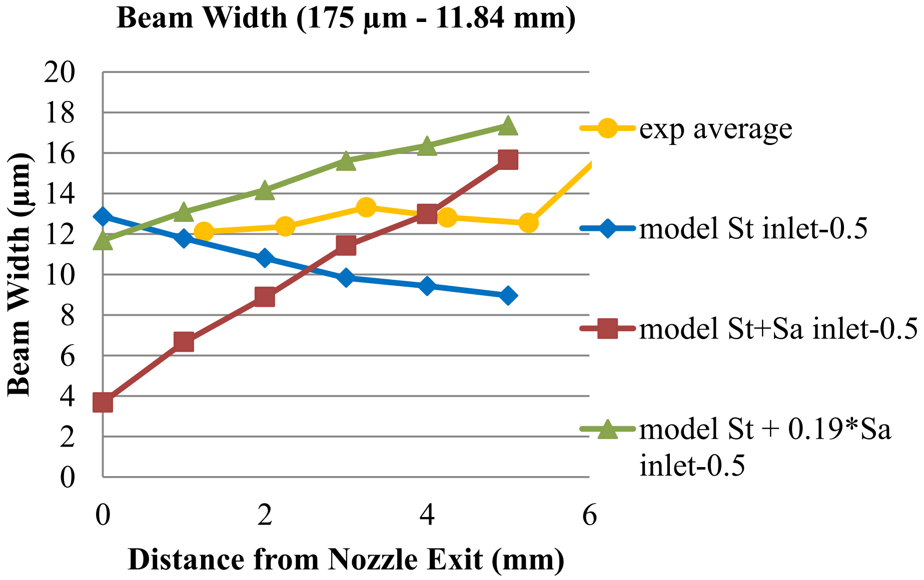

Figure 47. Graph of beam width vs. distance from the nozzle exit for a 175 µm converging nozzle coupled to an 11.84 mm long 200 µm diameter straight section.

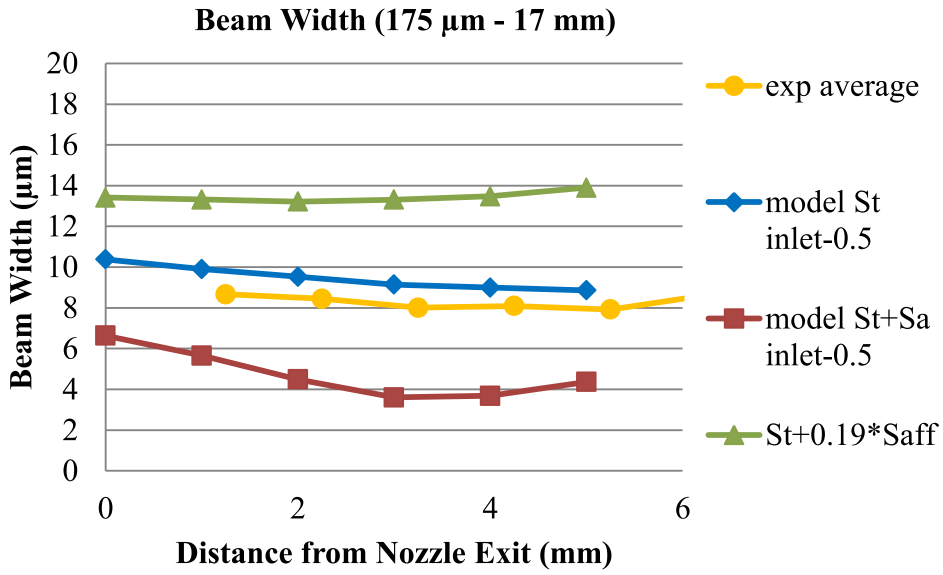

Figure 48. Graph of beam width vs. distance from the nozzle exit for a 175 µm converging nozzle coupled to a 17 mm long 200 µm diameter straight section.

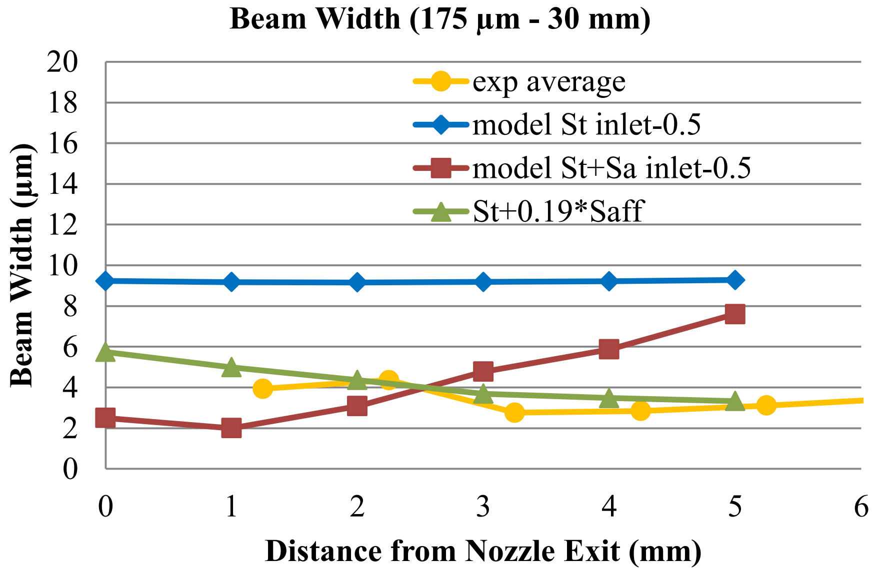

Figure 49. Graph of beam width vs. distance from the nozzle exit for a 175 µm converging nozzle coupled to a 30 mm long 200 µm diameter straight section.

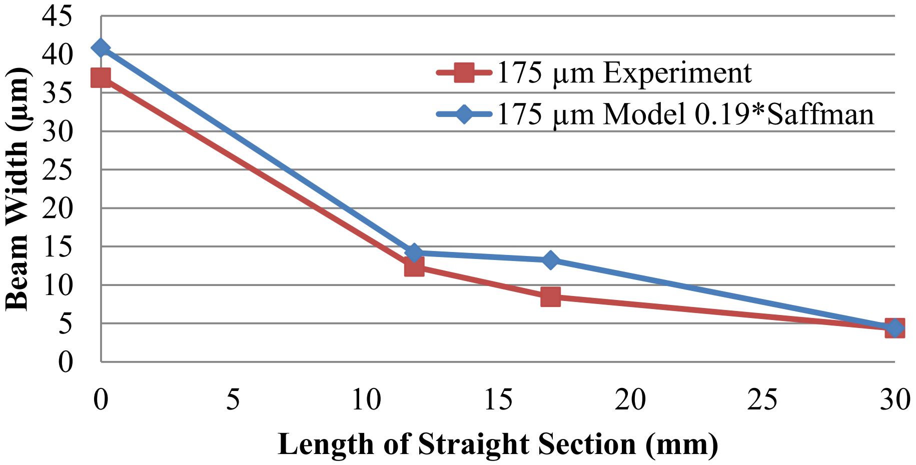

Figure 50. Graph of the beam width of the 0.19* Saffman vs. length of the straight section of the nozzle for the 175 µm to 200 µm straight section as compared to experimental results at 2 mm from the nozzle exit.

5.8. Confirmation of Printed Line Widths

5.8.1. Single Nozzle Results

To confirm experimentally that focusing is taking place the lines deposited onto a substrate can be examined as well. The widths of deposited lines should change as the stand-off distance is varied if there is indeed focusing. Experimentally, focusing was determined by printing over a step. A glass microscope slide was placed on a small sheet of Kapton® film and then Kapton® tape was placed over the glass slide. The glass slide produced a 1 mm step as seen in Figure 51. The stand-off distance was initially set to 2 mm over the glass slide, thus when the capillary passes over the glass slide edge, the stand-off distance increases to 3 mm.

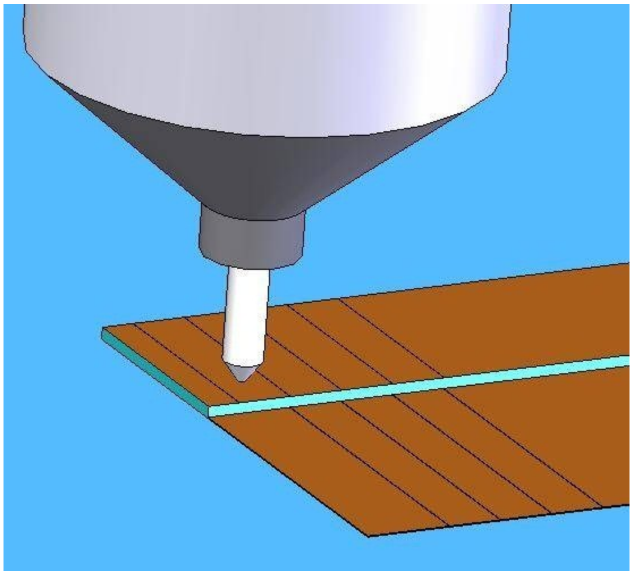

Figure 51. Experimental geometry for printing over a 1 mm step, reprinted from Akhatov et al. [82], Copyright 2008, with permission from Elsevier.

The results of lines written over a 1 mm step can be seen in Figure 52. The 800/100 µm micro-capillary with an aerosol flow of 25 cm^3/min, sheath flow of 15 cm^3/min, stage velocity of 30 mm/s and silver nano-ink supplied by Harima were used for this experiment. The as-deposited line widths are 29.9 µm and 47.2 µm for a stand-off distance of 2 mm and 3 mm respectively. The sintered line widths are slightly less than the as-deposited line widths with 23.8 µm and 42.8 µm widths for 2 mm and 3 mm stand-off distances respectively. Notice that the in-flight beam widths in Figure 34 for 2 mm and 3 mm stand-off distances are 5.13 µm and 17.56 µm respectively. The beamwidth at these points could be assumed as a rough approximation of the absolute minimum line width for each stand-off distance. The increasing in-flight beamwidth as the stand-off distance increases from 2 mm to 3 mm has a similar trend to the increasing line width at similar stand-off distances. A direct quantitative comparison cannot be made due to the spreading of the line on the substrate which is a function of surface tension; however, the trend is still similar and is good evidence of the focusing of the aerosol particles in a micro-capillary.

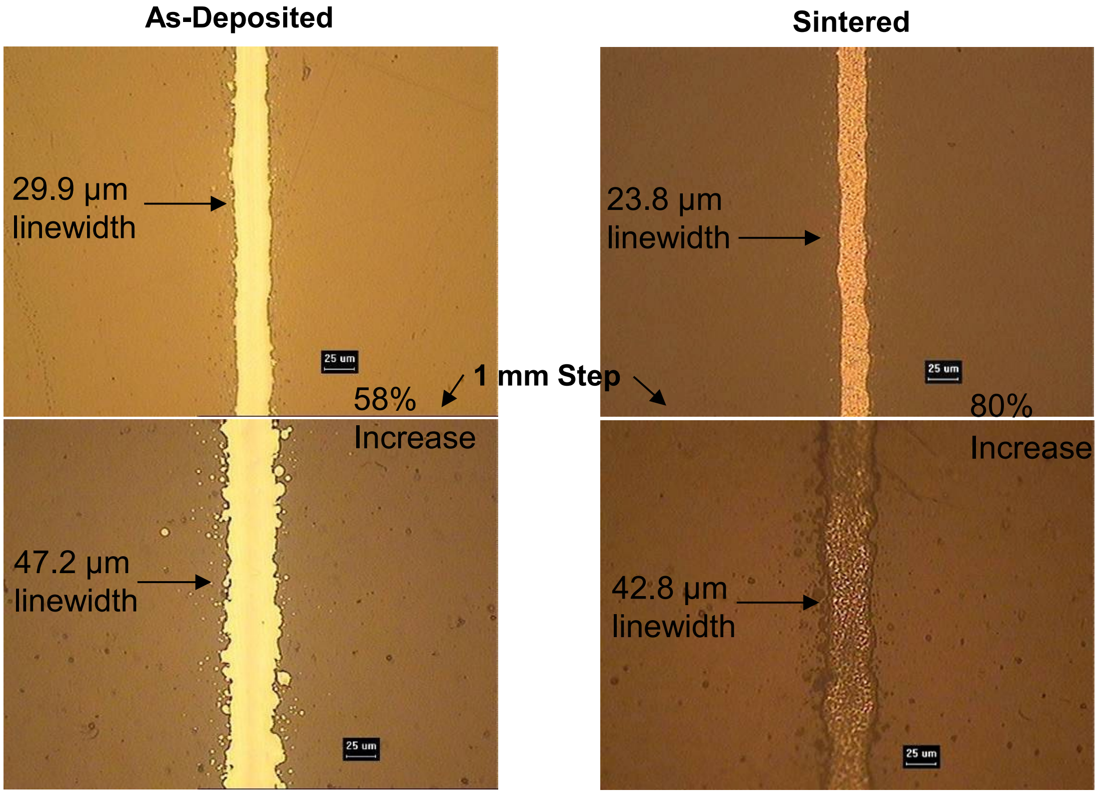

Figure 52. Experimental pictures of lines drawn over a step with Harima ink. Parameters: 800/100 µm micro-capillary with aerosol flow of 25 cm^3/ min; sheath flow of 15 cm^3/min; and a stage velocity of 30 mm/s, reprinted from Akhatov et al. [82], Copyright 2008, with permission from Elsevier.

5.8.2. CAB-DW Printing Results

Not only was the aerosol beam more focused with CAB-DW than Aerosol Jet, but the printed lines were also thinner when comparing the two at identical conditions (25 sccm carrier gas, 15 sccm sheath gas, 2 mm stand-off height, 30 mm/s translation) where aerosol Jet afforded 31 µm wide lines and CAB-DW produced 11 µm wide lines as shown in Figure 53.

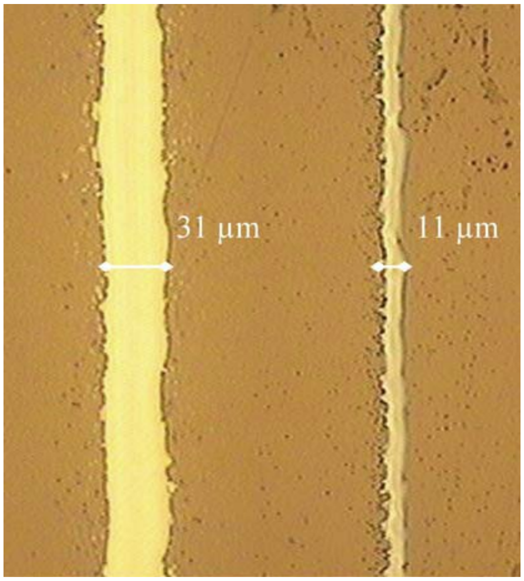

Figure 53. Comparison of A-DW printed lines made with Aerosol Jet (left) and CAB-DW (right) under identical print parameters (25 sccm carrier gas, 15 sccm sheath gas, 2 mm stand-off height, 30 mm/s translation), reprinted from Akhatov et al. [8], Copyright 2008, with permission from Springer.

5.8.3. CAB-DW Printed lines on Tape

Silver lines were printed using a 100 µm CAB-DW nozzle with a carrier gas (20 - 30 sccm) and sheath gas (10 sccm) flow. Aerosol was produced via an ultrasonic atomizer operating at 2.4 MHz with a commercially available (PV Nanocell) silver nanoparticle (50 nm) ink based on a solvent of ethylene glycol and diluted 50% with DI water. The nozzle was elevated to 2 mm from the substrate during the printing and the stage was traversed at 5 mm/s. Platen temperature was maintained at 80 °C. The substrate was a cleaned glass microscope slide. Silver lines were printed atop a glass microscope slide which was taped to the heated platen using standard Scotch® tape to ensure the substrate would not slide as the stage was traversed. The tape was inadvertently slid across the substrate during assembly leaving a residue of the adhesive on the slide. While printing, one of the lines was printed over the adhesive. It was noticed that the line on the adhesive was substantially thinner (i.e. 4 µm vs. 8 µm) as illustrated in Figure 54. It was determined that further investigation into the properties of lines printed on adhesive was warranted.

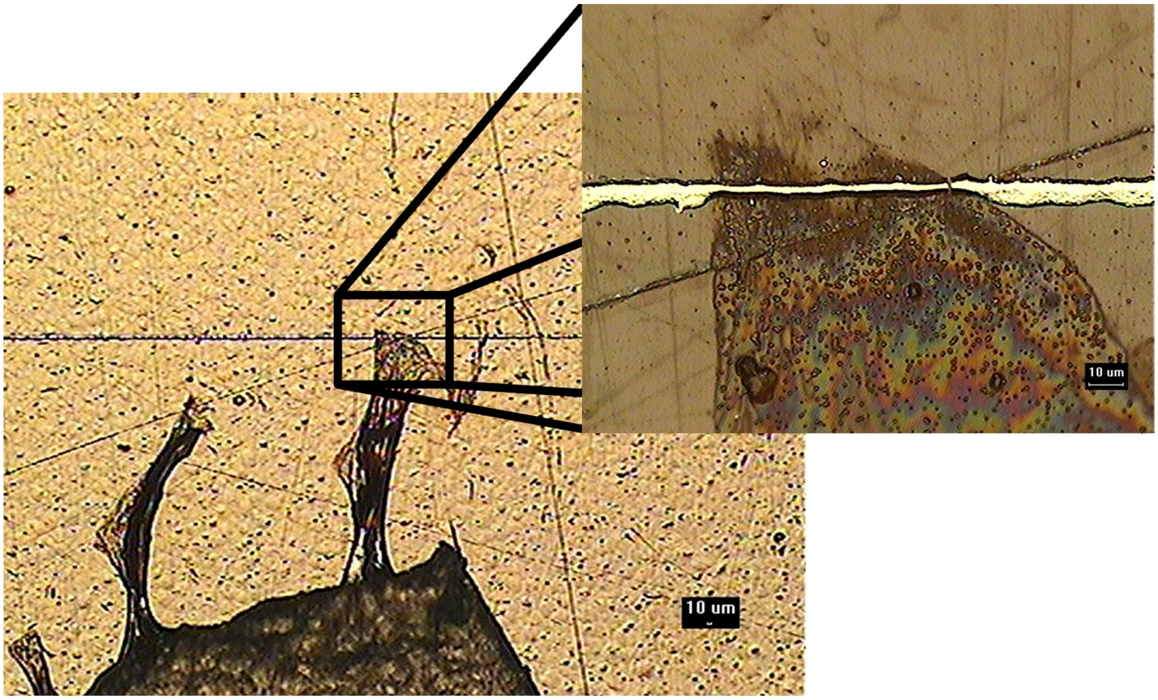

Figure 54. Optical microscope images of silver lines printed on a glass microscope slide and residual tape adhesive.

First, lines were printed on plain glass slides. These lines were shown to be as thin as 8 µm (Figure 55a). The lines were created with 15 sccm carrier gas, 25 sccm sheath gas, and a translation speed of 10 mm/s. The edge definition in this case is not as good as possible due to the irregular wetting of the ink with the surface. Excellent edge definition and reduced overspray can be achieved by printing wider lines. When the ink is deposited, it flows from the deposition region, covering any overspray and surface anomalies. Lines of 25 µm were also created and can be seen in Figure 55b. Better visualization of the lines was obtained using SEM imaging as shown in Figure 56. A cross section of the line reveals that the line is between 1 μm and 1.65 μm in thickness, and 11 μm wide. Note that these lines in the SEM pictures were drawn on glass.

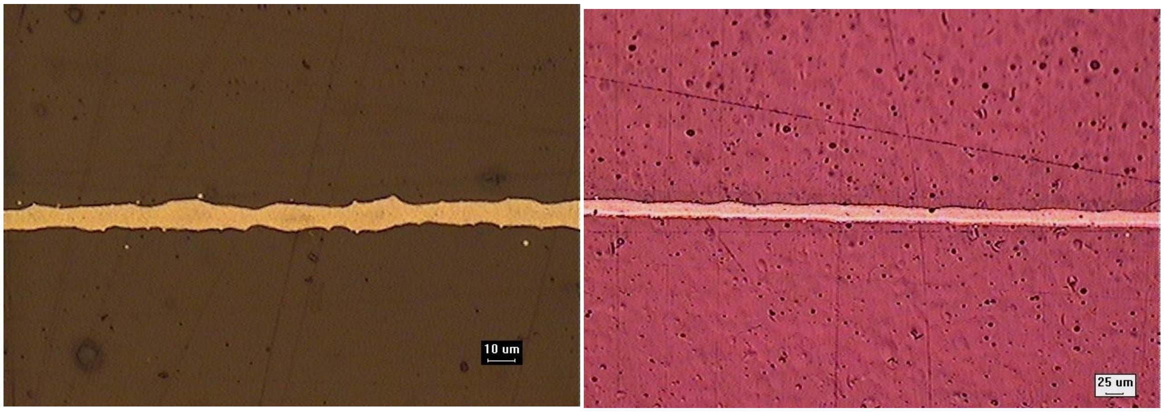

Figure 55. Silver lines printed on glass with a) 8.7 μm wide line using 15 sccm carrier gas, 25 sccm sheath gas, b) 25 μm wide line using 20 sccm carrier gas, 25 sccm sheath gas, and a 5 mm/s translation speed.

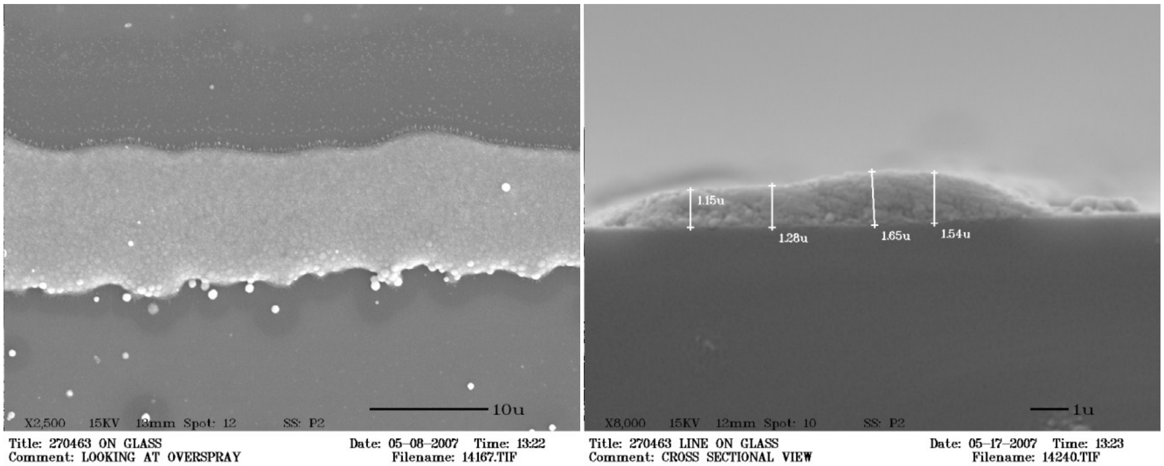

Figure 56. SEM images of CAB-DW printed line. Line width is approximately 11 μm.

Lines were printed on adhesive (Scotch® permanent double-sided tape) using an additional gas which was inserted along with the carrier gas. This gas is further more called the diluent gas. Parameters for printed lines were 20 sccm carrier gas, 10 sccm sheath gas, 10 sccm diffuser gas, and a translation speed of 10 mm/s. Visibly, the lines were much smaller than those printed on glass. Optical microscope images are shown in Figure 57, where a minimum line width was measured at 3.7 µm. Due to this very small width, SEM imaging may be a more accurate method of measuring line width. Using SEM imaging, the lines appear slightly wider as shown in Figure 58, where widths of approximately 5.3 µm were measured. Notice that the edge is much more difficult to distinguish in this image as compared to optical images.

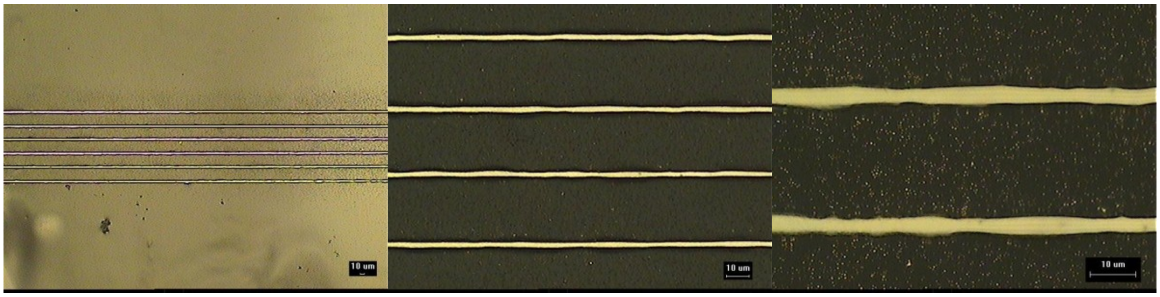

Figure 57. Lines written on double sided tape. Using flow rates of 20, 10, and 10 for the aerosol sheath and diffuser flows respectively. Line-widths appear to be approximately 3.7 µm.

The line on tape was cross-sectioned and further imaged as shown in Figure 59. The line when deposited created a trough in which it rested. This trough is approximately 1 µm deep and the printed line extends horizontally underneath the trough increasing the line-width to approximately 6.2 µm. This trough phenomenon is the reason why lines appear much thinner in the optical images as compared to the SEM images. The trough does have marked benefits in decreasing line-width, improving edge definition, and increasing the line aspect ratio (line height/ line width). This idea of simultaneously creating a trough while printing a line is novel, and may prove beneficial for certain applications where buried contacts are desirable. The objective of this experiment was to print only on adhesive to determine the decrease in line width, but in this experiment, printing was done on a soft polymer lines with adhesive. The soft polymer (when heated) deformed under the forces caused by the aerosol particles and gas stream.

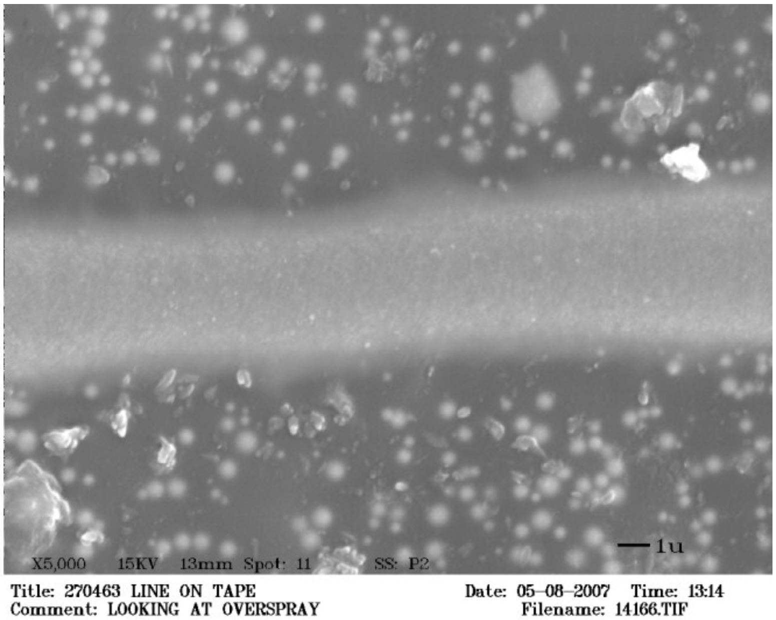

Figure 58. SEM image of line on tape. Line width is approximately 5.3 µm.

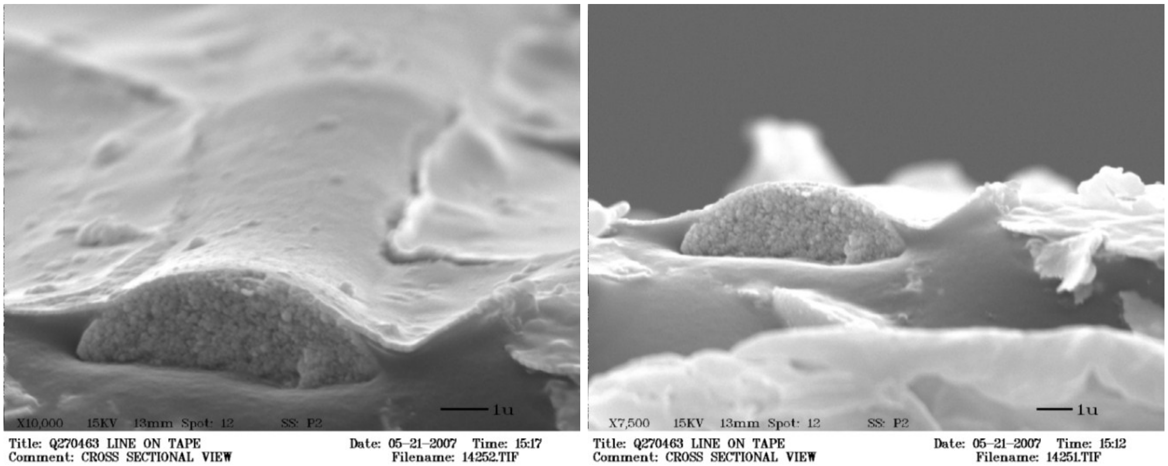

Figure 59. SEM pictures of silver line written on double-sided tape with CAB-DW. Approximate line width is 6.2 µm.

5.8.4. Printing Results Using Converging-Straight Nozzle

Measuring the beam width of aerosol particles, is generally a good predictor of the printed line width as was found for CAB-DW. The beam widths measured for converging-straight nozzles, however, was done using larger (3.8 μm) particles. These particles are likely larger than that found for liquid aerosols, so printed lines may be much different. In fact, a simulation of 1 μm particles through a 175 μm converging ceramic capillary coupled to a 17 mm long, 200 μm straight capillary show beam widths will be around 75 μm if modeled using Stokes force only as shown in Figure 60.

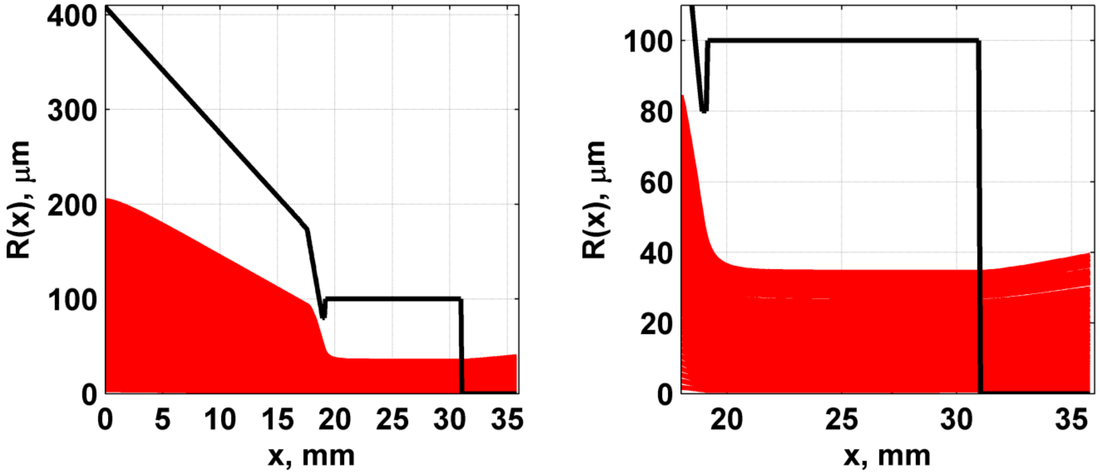

Figure 60. Geometry and simulation of 1 μm silica aerosol particles through a 175 μm ceramic converging capillary into a 200 μm tungsten carbide capillary of 17 mm length using Stokes force only.

Lines were printed using several nozzles including a 175 μm ceramic nozzle, CAB-DW, a 175 μm ceramic nozzle coupled to a 30 mm 200 μm diameter straight section, and a 100 μm ceramic nozzle coupled to a 30 mm 200 μm straight section. Printing was done using Novacentrix ink, with a 2 mm nozzle-substrate distance at a translation speed of 10 mm/s. total flow rate was held constant for all nozzles with a flow rate of 120 ccm for the 175 µm nozzles, and 40 ccm for the CAB-DW and 100 µm nozzle. The ratio of carrier gas to sheath gas was adjusted to see the relation this had on line width. Line width was measured using optical microscopy. Results of the experiment are shown in Figure 61.

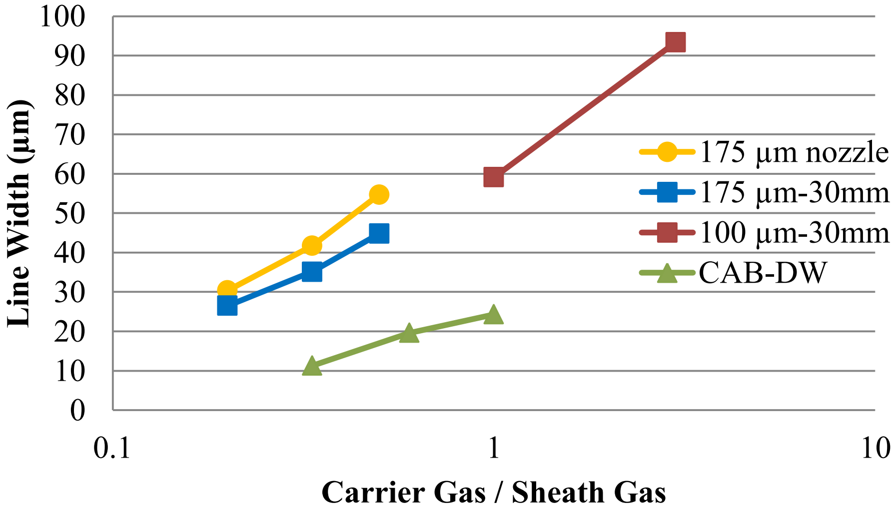

Figure 61. Printed line widths vs. carrier gas to sheath gas ratio for liquid aerosols using silver ink.

Results of this experiment confirm that printed line widths are indeed wide at widths from 26.5 µm for the 175 µm connected to a 30 mm straight section at a carrier gas flow of 20 ccm and sheath flow of 100 ccm. Thinnest lines were achieved with CAB-DW, at 11.3 µm at a flow of 10 ccm carrier and 30 ccm sheath gas. The graph does show a slight improvement in lines widths as a function of carrier gas/ sheath gas of the 175 µm nozzle coupled to a straight section as compared to the nozzle without a straight section. Overall, this experiment shows that the converging nozzles coupled to a straight section are not ideally suited for liquid aerosols of small particle size. Other applications using larger particles however may prove useful.

5.9. Consideration of Drop Impaction on a Substrate

At present, aerosol-based direct-write technology suffers from "overspray" that is reported as deleterious for the manufacture of printed electronics such as displays, smart cards, RFID tags, sensors, solar cells and batteries where precise drop placement and deposition is required [111]. This topic was presented at the IEEE-PV conference in Philadelphia, PA in 2009 [109]. (The review portion of this section was predominantly created with Dr. Akhatov, and further edited for fitment.) There are two plausible reasons for overspray: (1) splashing when a liquid droplet strikes a substrate; and (2) lack of control over the beam that gives spots of deposited material outside the desired line width. The case for droplet splashing is now considered.

An up-to-date review of the interaction of liquid droplets impinging substrates has been presented by Yarin [112]. A similar evaluation specific to the inkjet printing processes has also been recently published [2]. In general, the forces that control this phenomenon (i.e., inertia, viscosity and surface tension) are embodied in the Reynolds number, Weber number

$$We = \rho d\, v^2 / \sigma\,, \tag{42}$$

which describes the ratio between droplet kinetic energy and surface energy where *d* is the droplet diameter and σ is the surface tension; Ohnesorge Number

$$Oh = We^{1/2} / \mathrm{Re} = \mu / \sqrt{\rho \sigma d}\,, \tag{43}$$

which describes the ratio between viscous and surface forces.

The droplet splashing limits for impact over dry and wet solid substrates may finally be defined in terms of a dimensionless parameter, K,

$$K = We\,Oh^{-0.4}. \tag{44}$$

For impact on a substrate covered by a liquid film of thickness h, the conditions for splashing have been experimentally determined as Equation (45) [113]:

$$K > K_h = 2100 + 5880H^{1.44}, \quad H = h/d, \quad 0.1 < H < 1. \tag{45}$$

For impact on a dry solid substrate the conditions for splashing depend on the roughness of the substrate ε, as Equation (46) [113, 114]:

$$K > K_\varepsilon = 649 + 3.76R^{-0.63}, \quad R = \varepsilon / d. \tag{46}$$

For the case of aerosol-based direct-write technology the ranges for *We* and *Oh* can be estimated based on the following data for aerosol-based deposition. The ink being used is a mixture of ethylene glycol, Ag nanoparticles and water. The density of the ink can be estimated as ρ_p=2000 kg/m^3 which mainly depends on the amount of nanoparticles dispersed in the ink. Based upon the ink composition, surface tension coefficients and viscosity can be roughly estimated as $\sigma = 6.34 \text{ X } 10^{-2}$ N/m and $\mu = 6.28 \text{ X } 10^{-3}$ N·s/m, respectively. In the experiments [113-115], the particle velocity, ν, was in the range of 75 and 90 m/s and the particle diameter, *d,* between 2 and 4 μm. These estimates give the following parameters for CAB-DW of Ag lines:

$$\begin{aligned} &We_1 < We < We_2, \quad We_1 \approx 345, \quad We_2 \approx 1022 \\ &Oh_1 < Oh < Oh_2, \quad Oh_1 \approx 0.28, \quad Oh_2 \approx 0.4 \\ &K_1 < K < K_2, \quad K_1 \approx 500, \quad K_2 \approx 1700 \end{aligned} \tag{47}$$

From these rough order of magnitude calculations, it is clear that splashing will not likely occur for aerosols impacting a wetted substrate for any thickness of the liquid film (see Eq. (45)).

In the case of deposition on a dry substrate, splashing will depend on the surface roughness. For relatively smooth substrates with surface roughness about ε = 1nm, from Equation (46) one can show that critical K_ε values will vary from 1100 to 1350. Thus, splashing may or may not occur for aerosol-based deposition on a dry substrate when roughness is low. There are no known reports where evidence of splashing has been confirmed or denied under similar parameters (i.e., v = 90 m/s and d = 2 μm).

In-situ imaging of the aerosol particles during printing was accomplished using the shadowgraphy system as schematically shown in Figure 62. Double-frame experiments were conducted with the following parameters: 125 μm ceramic nozzle; 20 sccm carrier gas; 20 sccm sheath gas; 0.3 and 0.5 mm/s stage velocity; 2 mm nozzle-to-substrate height; 0.4 μs between frames; and, a 10 ns pulse duration. The ink used was a mixture of 33% ethylene glycol in DI water.

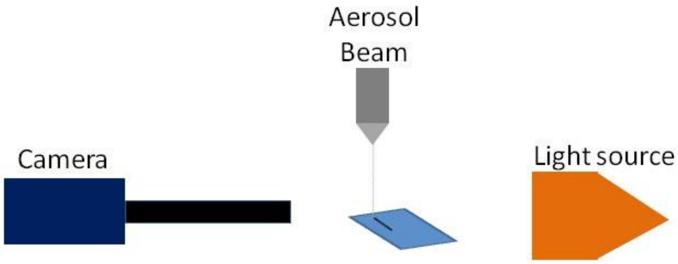

Figure 62. Schematic of shadowgraphy system used to visualize drop impaction in-situ, from Hoey et al. [109], Copyright 2009 IEEE.

A set of pictures of a single aerosol droplet before and after impact are shown in Figure 63. In this figure, the aerosol beam is directed normal to the substrate such that particles look to have moved downward in the subsequent image. It appears that an in-flight particle is impinging the leading face of a liquid film with no rebounding or satellites observed. Additional information can be ascertained from the shadowgraphy images where average particle size was 2.7 ± 0.4 μm and the vertical velocity of the particles was 87 ± 4 m/s. These initial results suggest that droplet splashing is not the major factor for overspray. Rather, it appears to be related to limited control of the aerosol beam. Toward that end, a deeper understanding of beam control shall lead to further improvement of the technology with respect to minimized overspray and finer pitch deposits.

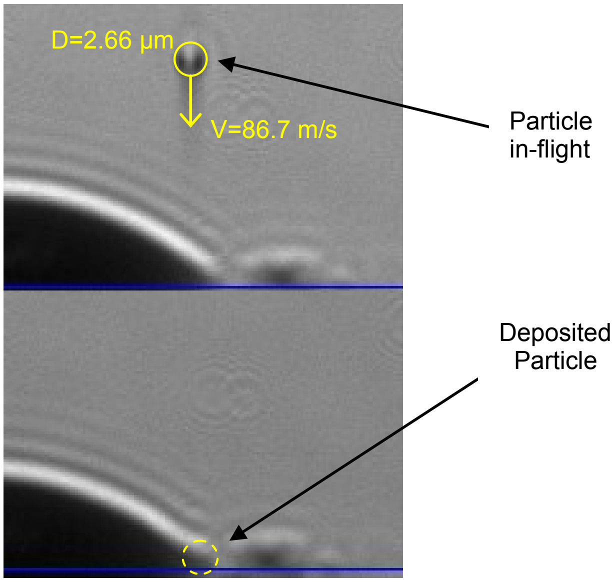

Figure 63. A double image of a single aerosol particle impacting a substrate, from Hoey et al. [109], Copyright 2009 IEEE.

6. AEROSOL DIRECT-WRITE APPLICATIONS

6.1. Micro Cold Spray – Solid Aerosols through Nozzles

Cold spray was developed in the early 1980's by Papyrin et al. [116] who was experimenting with two-phase supersonic flow and found that at certain critical velocities particles would adhere to surfaces. This adherence is caused when the aerosol particle impacts the substrate at a velocity great enough to cause plastic deformation of the particle and/or substrate which results in a localized heating and high pressure region creating intimate contact between the particle and substrate. The critical velocity is dependent on a combination of the particle material, substrate material, particle temperature prior to impaction, and particle size. Critical velocities for copper, iron, nickel and aluminum are reported to be ~570, 630, 630 and 690 m/s, respectively [117]. Cold spray technology was developed into a commercial system designed for thin film deposition in 2001 [116, 118].

The knowledge of aerosol focusing in conjunction with the understanding of cold spray technology lead to the development of a new technology termed micro cold spray (MCS) direct write. The ability to focus the spray of powder to small (<100 μm) dimensions gives beams of material and substantiates the term MCS. The idea behind MCS is to use nozzles developed in our aerosol focusing experiments for use with solid powder at high velocity. In this case not only is the focus and collimation of the particles important, but so is the particle velocity. Building from the experimental-analytical comparison of liquid aerosols discussed in Section 0 of this report, in our previous paper by Bhattacharya et al. [11], and from work accomplished as further described in Sourin Bhattacharya's Dissertation [119], the development and applications of MCS are further described.

An advantage of MCS of circuit metallization/interconnects is that the deposited material require no post-processing. MCS incorporates a nozzle system to deposit lines of ductile metals that exhibit conductivities that reach 90% of the bulk values. Figure 64 is a schematic diagram of the NDSU MCS system which shows the following infrastructure: helium gas first passes through one of two mass flow controllers (MFC). The outlet of the first MFC passes through a powder feeder where solid particles are aerosolized into the He, creating a carrier gas stream (Figure 64a). The second MFC controls the He accelerator gas flow to around 2 LPM (versus 100 sccm for the carrier). Each of these streams then enters the deposition head (Figure 64b) where both are heated to offset the cooling effect of gas acceleration. The two streams interact in the flow-cone section of the deposition head and finally pass through a converging nozzle. Nozzle diameters of 100 to 200 µm are commonly employed and a multi-nozzle system could also be adopted. MCS is capable of printing traces from solid aerosols of tin, aluminum and copper onto various hard and flexible substrates. Formation of continuous lines depends upon both the substrate materials as well as the solid particles being deposited. Table 3 shows a list of the substrates with a (+) or (-) designating whether or not a particular solid metal aerosol gave a continuous line. Electrical properties were measured for copper traces prepared using a 100 µm focusing nozzle, 400 ccm carrier gas (aerosol) flow, ~0.75 MPa accelerator (sheath) gas pressure, 0.5 mm stand-off distance and a 1 mm/s translation speed (greater speeds possible). These traces were ~50 µm wide (Figure 65) and had a resistivity of 1.9 µΩ-cm. In addition to metallic traces, the ability to fill vias from 75 µm to 150 µm in diameter with metals was demonstrated, creating the possibility of including trace deposition and via filling into one process.

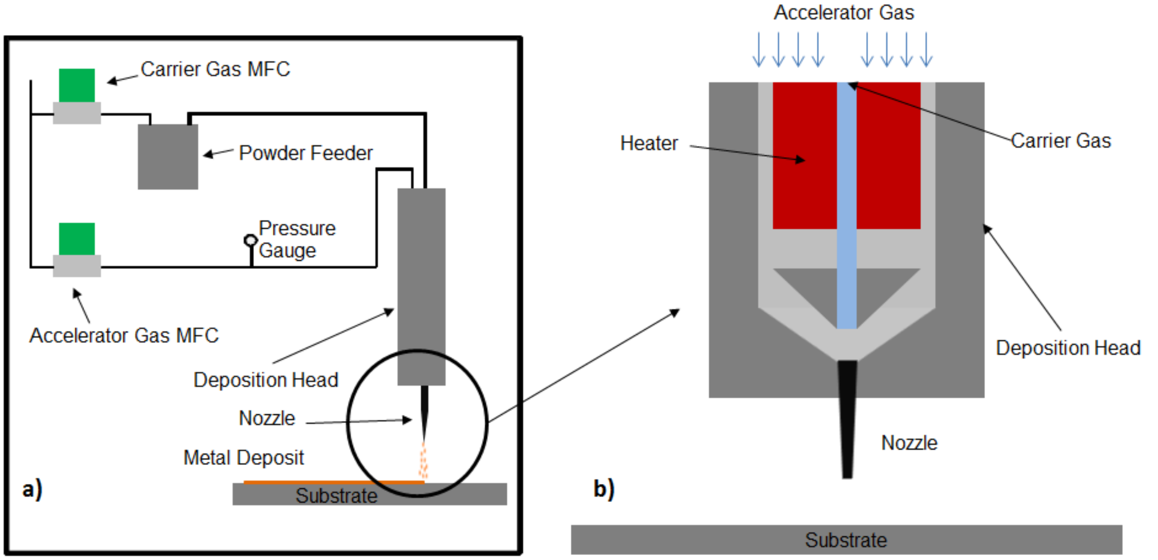

Figure 64. Schematic diagram of a) the MCS system for solid aerosols, b) MCS deposition head, from Bhattacharya et al. [11], Copyright 2012 ASME. Reprinted with permission.

Table 3. MCS material-substrate compatibility, from Bhattacharya et al. [11], Copyright 2012 ASME. Reprinted with permission.

Substrate	Tin	Aluminum	Copper
Glass	+	+	+
Silicon	+	+	+
BT[1]	+	+	-
PEEK[2]	-	+	+
Kapton	+	+	-
Teflon	-	+	+
PES[3]	-	+	+
LCP[4]	-	+	+
Teslin	-	-	+
FR4[5]	-	+	-
Mylar	-	+	+

[1] Fiberglass-reinforced Bismaleimide Triazine Epoxy
[2] Polyether ether ketone
[3] Polyethersulfone
[4] Liquid crystal polymer
[5] Glass-reinforced epoxy laminate

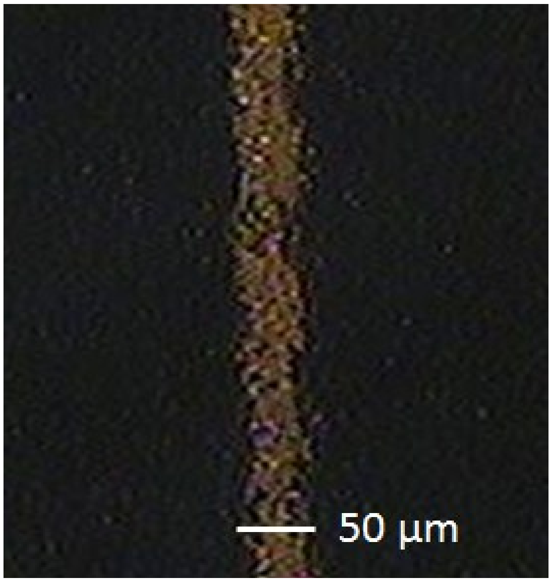

Figure 65. Image of MCS printed 50 µm wide copper line on glass, from Bhattacharya et al. [11], Copyright 2012 ASME. Reprinted with permission.

The previous results were accomplished using ceramic and tungsten carbide nozzles with only a converging geometry. Results discussed in Section 5.8.4 showed how a converging nozzle coupled to a straight section will dramatically reduce beam widths using 3.8 µm silica particles. In MCS, solid particles near that size range are commonly employed, so this seems a natural application of these nozzle sets. The other main benefit of the converging-straight nozzles is that particle velocity is dramatically increased as compared to only a converging nozzle. An example of velocities achieved through simulation is shown below in Figure 66. Here Figure 66a shows the geometry and trajectories of particles in a linearly converging 200 µm diameter nozzle, 19.05 mm long connected to a 200 µm diameter straight capillary of 30 mm length. Rather than flow rate, pressure was set, using 225 kPa (red) and 475 kPa (blue) lines and particles are 3 µm diameter copper. In Figure 66b the velocity of the particles are shown where maximum velocity achieved is ~450 m/s for 225 kPa inlet pressure, and >550 m/s for 475 kPa inlet pressure. These results suggest that critical velocity can be achieved using this nozzle with subsonic flow.

Due to the increased velocity achieved in the modeling results with the converging-straight nozzles, deposition should occur at much lower preheat temperatures and/or pressures as compared to only a converging nozzle. To confirm this, MCS was run using a 175 µm converging nozzle coupled to a 200 µm diameter 30 mm long straight section. Deposition of 3 µm copper occurred at an inlet pressure of 550 kPa (5,800 ccm), with a preheat temperature of only 100 °C. When only a converging nozzle was used, preheat temperature must be ~250 °C. These results confirm that a reduced preheat temperature is afforded with the new nozzle designs. Further experiments would need to be completed to determine if deposition could occur at room temperature.

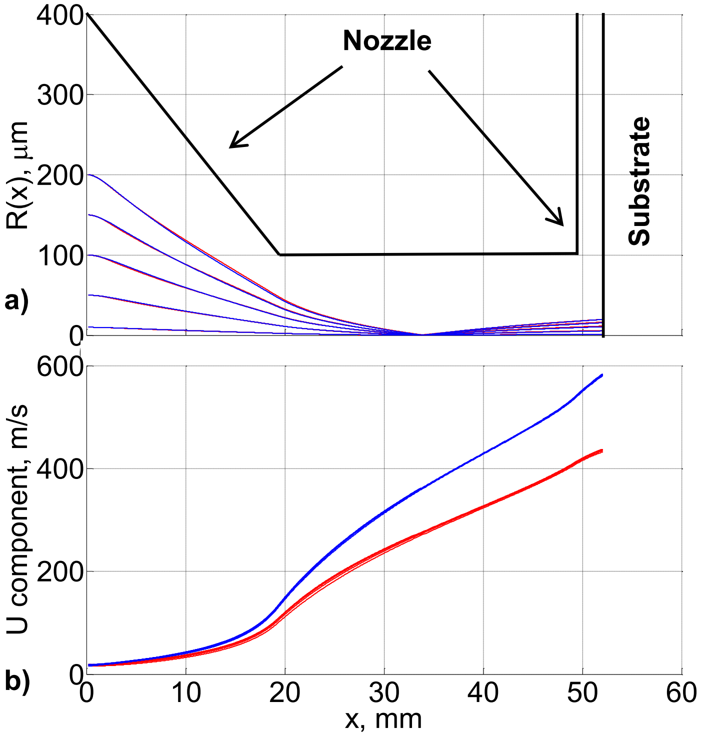

Figure 66. Graph of 3 μm copper particles through a 200 μm linearly converging nozzle connected to a 30 mm, 200 μm diameter straight section; a) nozzle geometry and trajectories of particles; b) velocity of particles. Inlet pressure is 225 kPa (red), 475 kPa (blue), reprinted from Bhattacharya [119].

6.2. Printed RFID Tags via Direct-Write

A-DW systems Aerosol Jet and CAB-DW along with MAPLE-DW were used to print silver nanoparticle based RFID antennas on Kapton® film at NDSU [111]. The goal of the research was to determine whether direct-write approaches were amenable to RFID applications. This work was published in IEEE Transactions on Advanced Packaging in 2009 [111].

6.2.1. RFID Materials

For this direct-write work, a “squiggle” dipole antenna geometry developed by Alien Technology (Morgan Hill, CA) for its UHF RFID product line was used as the benchmark. Each antenna in an RFID application is uniquely designed for use with a particular integrated circuit, so the matching ICs were also obtained from Alien Technology and attached to the direct-written antennas after post-processing. In order to effectively create trace geometries wider than a single direct-write trace, multiple parallel traces were applied. Overlap of adjacent direct-written traces was also required in some cases to ensure complete coverage. Individual Aerosol Jet written lines were between 60 and 100 µm wide, CAB-DW lines were between 20 and 25 µm wide and MAPLE-DW traces were between 140 and 160 µm wide. Spacing between adjacent lines was 20 µm for Aerosol Jet and CAB-DW and 100 µm for MAPLE-DW.

Ink used for Aerosol Jet and CAB-DW consisted of 50 nm silver particles dispersed in ethylene glycol (Nano-Size Inc.). Dilution of the ink was required for those direct-write methods where atomization was a requisite part of the process (i.e., Aerosol Jet and CAB-DW). Toward that end, Aerosol Jet used a mixture comprised of 20 vol. % Nano-Size AG 310EG, 40 vol. % deionized water and 40 vol. % 100 PPM ethylene glycol in water. The CAB-DW process used a mixture of 50 vol. % Nano-Size Sample AG 310EG ink, 25 vol. % deionized water and 25 vol. % 100 PPM ethylene glycol in water. MAPLE-DW used ink as-received from Harima Inc. and was composed of a suspension of 57-62 wt. % 50 nm diameter particles of silver, 27-34 wt. % n-tetradecane solvent and 8-

12 wt. % dispersants. The MAPLE-DW ribbon thickness was 14 µm and was applied using a 25 µm thick doctor-blade film applicator. Kapton grade HN film (5 mil thick) was used as the substrate for all three direct-write deposition processes. After printing of the silver inks, all antennas were thermally-treated in air at 250 °C for 1 hour. Figure 67 shows pictures and micrographs of each of the antennas in this study.

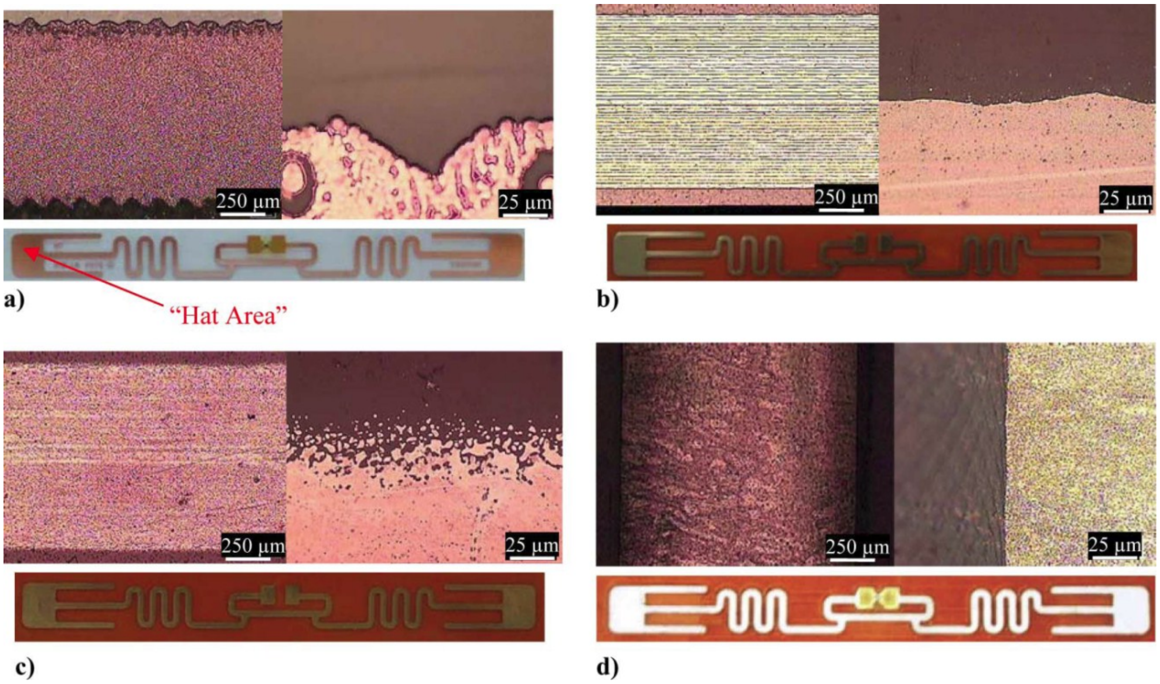

Figure 67. Picture and micrographs of Alien squiggle antennas made with a) copper etching, b) CAB-DW, c) Aerosol Jet, and d) MAPLE-DW, reprinted from Hoey et al. [111], Copyright 2009 IEEE.

Surface profiles were determined using a KLA Tencor P15 stylus profiler with a 2 µm radius probe. Surface morphologies were ascertained with a Veeco/Wyko NT3300 optical profiler. Profiles were determined at a 1-mm wide section of the antenna. Average thicknesses of the tags and surface roughness are displayed in Table 4. Graphs of the cross sectional area of each tag using the stylus profiler can be seen in Figure 68. Note that the large surface roughness of the CAB-DW printed lines was primarily due to the spacing of individual traces which produced a regular wave-like surface.

Table 4. RFID Physical Characteristics, reprinted from Hoey et al. [111], Copyright 2009 IEEE.

Antenna	Average Trace Thickness (μm)	Surface Roughness, Ra (nm)
Alien	3.70	157
Aerosol Jet	0.28	124
CAB-DW	0.51	201
MAPLE-DW	1.93	54

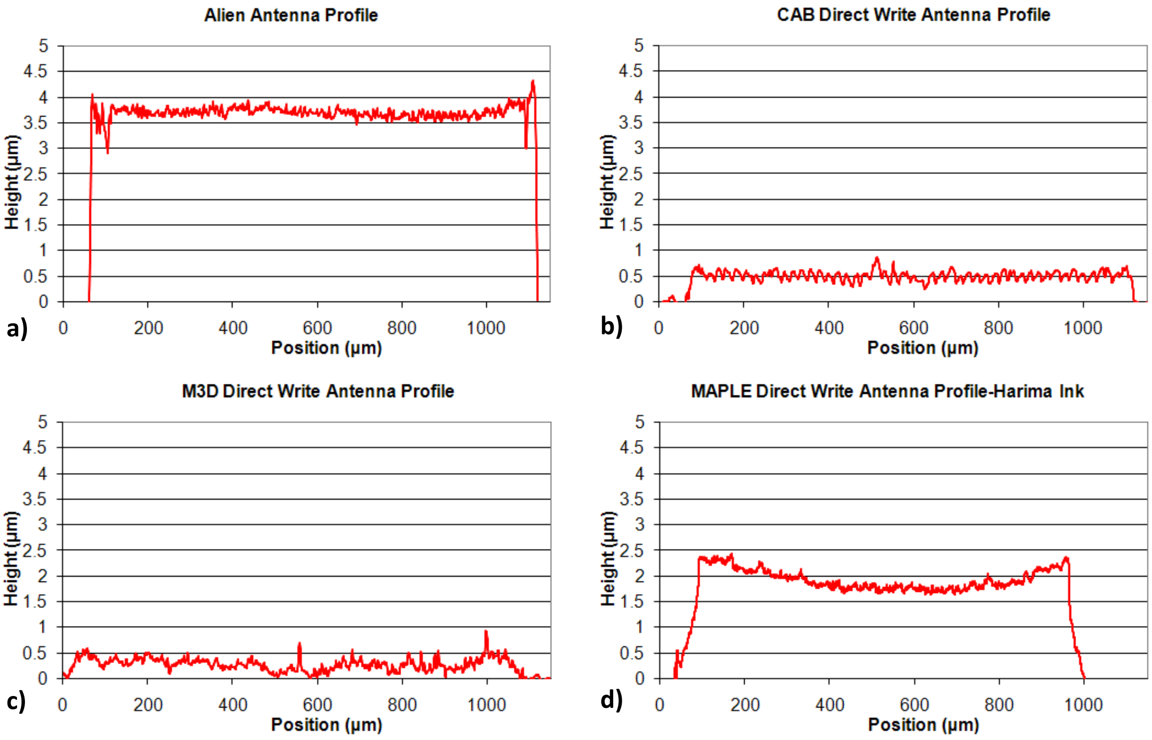

Figure 68. Antenna surface profiles of a) Alien antenna, b) CAB-DW antenna, c) Aerosol Jet (M^3D) antenna, and d) MAPLE-DW antenna, reprinted from Hoey et al. [111], Copyright 2009 IEEE.

6.2.2. RFID Methods

Four different antennas with the same target geometry were tested in this study (Figure 67). A commercial-off-the-shelf Alien antenna based on thin film copper was used as the control. The experimental group for this dataset included silver antennas prepared by CAB-DW, Aerosol Jet and MAPLE-DW. Measurements of antenna performance were conducted using an Alien 9800 RFID signal interrogator. Once a tag had been properly positioned and aligned with the reader antenna, a custom program was used to determine the minimum reader transmit power needed to successfully interrogate the tag. This was accomplished by stepping down the output power from the reader until communication with the tag was lost. This minimum transmit power was then used to estimate the maximum communication distance that could be achieved between the tag and the reader.

A total of six Alien tags were tested two times each while three tags from each direct-write version were tested a total of four times each. There was little variance in the measurements taken for each tag and a maximum standard deviation of less than 5% was in all instances. Antenna dc sheet resistances were determined using a Cascade Microtech C4S44/S 4-point probe with a Keithley 2400 multimeter. The resistances were measured at the end of the tags in the “hat area” (see Figure 67a) four times per tag (twice on each hat) with the probes being removed and re-contacted in a slightly different location prior to the subsequent data collection. Minor deviations from ideal sheet resistances due to geometrical factors have an effect on these measurements but a comparative analysis is most important for this discussion.

6.2.3. RFID Results and Discussion

A potential concern was that the overspray would limit the performance of RF wireless devices manufactured using direct-write processes. Using rapid prototyping direct-write tools, experiments were performed to either confirm or dispel this potential limitation for direct-write of RFID antennas. As illustrated in Figure 69 and shown in Table 5, the average maximum communication distance of the MAPLE-DW, Aerosol Jet, and CAB-DW antennas is 74%, 81%, and 89%, respectively, of the average maximum communication distance of the commercial tags. Additionally, the best performing tags for each direct-write category fall into the range of values observed for the Alien tags. While every effort was made to ensure consistency during manufacturing and testing, the spread seen in the performance of the direct-written tags could be due to several factors including (1) inconsistencies in the strap attachment procedure, (2) slight variations in ink composition or deposition between antennas, and/or (3) variations in the testing environment.

Several factors, including sheet resistance, surface/edge morphologies and geometrical deformities were examined to determine the effect on overall tag performance. As can be seen in Figure 69, the sheet resistances of the direct-written tags are significantly larger than the Alien antenna. This may be due to the decreased thickness and/or non-ideal sintering/densification of the printed deposits. While the direct-write antennas have sheet resistances nearly an order of magnitude higher than the copper antenna (35 to 45 mΩ/□ versus 5 mΩ/□), this has little effect on the maximum communication distance.

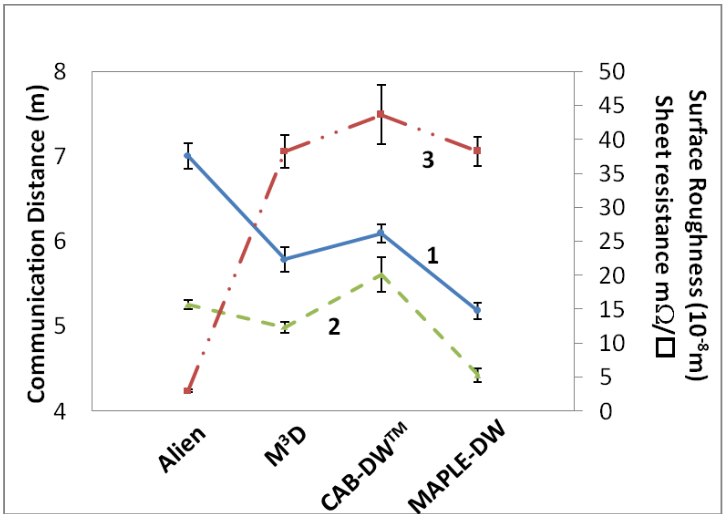

Figure 69. Comparison of (1) maximum communication distance, (2) surface roughness and (3) sheet resistance. Error bars are the standard deviation of each test, from Hoey et al. [111], Copyright 2009 IEEE.

Table 5. Maximum communication distance, from Hoey et al. [111], Copyright 2009 IEEE.

Antenna	Maximum[a]	Minimum[a]	Average[a]
Alien	7.7	5.8	7.0
Aerosol Jet	6.4	4.9	5.7
CAB-DW	6.7	5.5	6.2
MAPLE-DW	5.7	4.7	5.2

[a] Distances are in meters.

The average surface roughness for the direct-write antennas (Table 4, Figure 69) are comparable or less than the commercially-available tags. There is no apparent trend between smaller surface roughness and improved performance. This might be rationalized as the surface roughnesses of all of the antennas are much smaller than the wavelength of the RF signal (e.g., 915 MHz gives a wavelength of ~ 33 cm) and no perturbation would thus be expected during signal propagation. Along these lines, edge definition also appears to have minimal effect on antenna performance. This can be seen by comparing the fine edge definition of the CAB-DW printed antenna to that of the commercial copper antenna (Figure 67) where similar performance is observed.

It is of note that the present study compares the performance of copper antennas that maintain good fidelity (i.e., dense metal with conductivity approaching bulk) to silver antennas that are somewhat porous with resistivity several times bulk. While a comparison of the commercial copper antennas to copper antennas prepared by direct-write may be more appropriate, such a study is limited by both the availability of a copper nanoparticle ink for direct-write as well as the propensity of copper nanoparticles to form oxide coatings that are deleterious toward conducting films [120]. We point out that given the small difference between the bulk conductivity for silver and copper (i.e., 1.6 vs. 1.7 mΩ.cm, respectively), it is expected that the reported performance losses are due to differences in the fidelity of the antenna patterns and not simply a consequence of substituting silver for copper.

6.2.4. RFID Conclusions

This study aimed to determine if RFID antennas can be successfully prototyped using direct-write processes. Tag performance was tested and results showed the predicted maximum communication distances for copper Alien tags do not markedly differ from the tags fabricated using silver antennas prepared by direct-write. In some instances, performance of CAB-DW and Aerosol Jet printed antennas were better than the commercially-available Alien tags. This observation may be counterintuitive to device engineers that claim any overspray is deleterious to performance of RF devices. In addition, it was thought that an antenna thickness less than about 4 μm would limit performance of UHF RFID tags. The performance results of tags that used printed silver antennas do not markedly differ from the Alien copper tag despite the fact that the antennas prepared by CAB-DW and Aerosol Jet are only 0.5 and 0.3 μm thick, respectively.

Testing results gave some insight into the inner workings of RFID devices with general trends in test results comparing well to antenna performance. The edge definition appears to have minimal effects on antenna performance which can be verified by comparing the edge definition of commercially-available Alien tags to antennas prepared by CAB-DW. In this instance, both tags have similar performance characteristics even though edge roughness is much greater for the Alien tags.

These experiments show that it is possible to direct-write functional UHF antennas for RFID applications using Aerosol Jet, CAB-DW and MAPLE-DW. These printed antennas show comparable performance to commercially-available RFID tags. It follows that these direct-write techniques represent a rapid prototyping route to RFID antenna designs that is simple, straightforward, timely and cost-effective. One of the direct-write methods, CAB-DW, may find additional utility given the fine edge definition possible with this new technique.

6.3. Printed TFTs by CAB-DW

6.3.1. Source-Drain Contacts for Bottom Gate TFTs

CAB-DW was used to print the source-drain contacts for bottom gate silicon based thin film transistors (TFTs) where the active material (Si_6H_{12} based liquid silane ink) was spuncoat onto silicon nitride coated P^{++} silicon wafers [121]. Interdigitated electrodes with an approximately 50 μm channel length were printed using silver nanoparticle ink and sintered in forming gas at 400 °C for 1 hour prior to spincoating the silicon active layer. A schematic of the transistor is shown below in Figure 70a, and an image of the transistor is shown in Figure 70b.

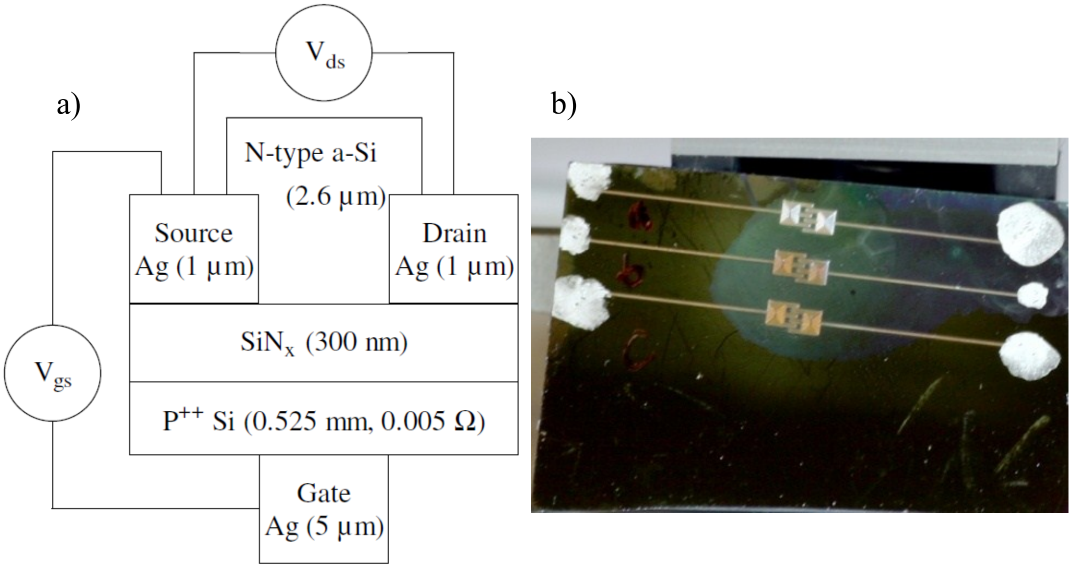

Figure 70. a) Schematic of Si_6H_{12} based transistor with CAB-DW source-drain contacts, from Han et al. [121], Copyright 2008, with permission from Elsevier. b) image of interdigitated transistor.

Initial characterization of the TFT showed a field effect, but no performance characteristics (i.e., on/off ratio, mobility) were reported. The results are shown in Figure 71. The shapes of the curves are correct, but because the source-drain current does not drop to zero when V_{ds} is zero. This is likely caused from shorting in the transistor gate.

Poly 3-hexylthiophene (P3HT) TFTs using CAB-DW printed source-drain electrodes were also printed [122]. One TFT, as shown in Figure 72, consisted of an n^{++} doped silicon wafer, 300 nm silicon nitride gate dielectric, 15 μm channel length silver nanoparticle based source-drain electrodes, 50 nm spincoated P3HT film using tricholorobenzene (TCB), and spincoated poly(methyl methacrylate) (PMMA) in anisole (methoxybenzene). The TFT itself had a mobility of about 10^{-2} cm^2/V-s. This TFT illustrates the benefit of using CAB-DW's high resolution (5 µm) printing which is easily able to produce 15 µm channel lengths.

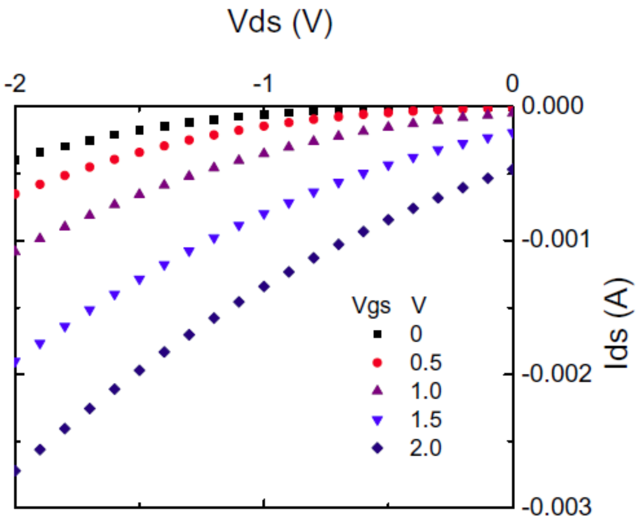

Figure 71. I_{ds} vs. V_{ds} for CAB-DW printed source-drain contacts silicon transistor, from Han et al. [121], Copyright 2008, with permission from Elsevier.

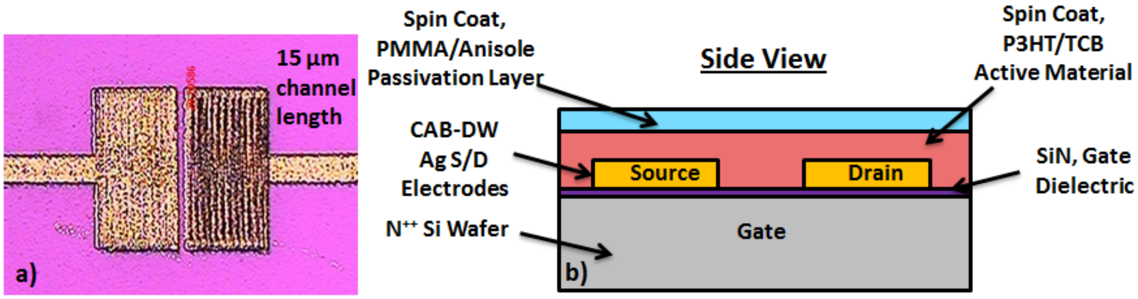

Figure 72. a) optical micrograph of Ag source and drain electrodes deposited by CAB-DW on SiNx-coated Si wafer with a channel length of 15 µm, b) schematic of all-solution processed bottom-gate P3HT active TFT, from Robinson et al. [122].

6.3.2. CAB-DW of Air Sensitive Materials

Printing the source and drain contacts for TFTs is an important first step to an all-printed TFT. To fully print TFTs, the active material must also be printed. Most active materials are sensitive to air and need to be used in an air-free environment. For this work, it was also desired to print with a liquid silicon material, Cyclohexasilane, Si_6H_{12} (CHS) which can be solution processed to form silicon features. An inert atmosphere glovebox was setup to print and process these materials. The glovebox is shown in Figure 73. Precision x-y stages (Aerotech Inc.) with 150 mm travel and 50 nm resolution were mounted to an aluminum breadboard. A heated (350 °C capability) platen was mounted to the top of the stages. An ultrasonic atomizer (2.4 MHz) utilizing a custom cooling system and silicon oil bath (Sonair Ultrasonics) is used for aerosolizing materials. An optical system to bring laser light into the glovebox for both laser sintering and polymerization was installed. In addition, cameras to view the liquid printing, laser sintering, and finished features were setup.

Once the glovebox was setup, printing of Si_6H_{12} could commence. The goal of the project was to print the liquid silicon in the active region of a TFT. First experiments were done using glass substrates and partially polymerized CHS. The printing ink consisted of 100 µL of partially polymerized CHS with 900 µL toluene. Printing was accomplished using parameters: CAB-DW nozzle, 5 ccm carrier gas, 30 ccm sheath gas, 5 mm/s print velocity with substrate temperature ranging of 350 °C. Printed results are shown below in Figure 74. As can be seen, the line is continuous and less than 20 µm wide.

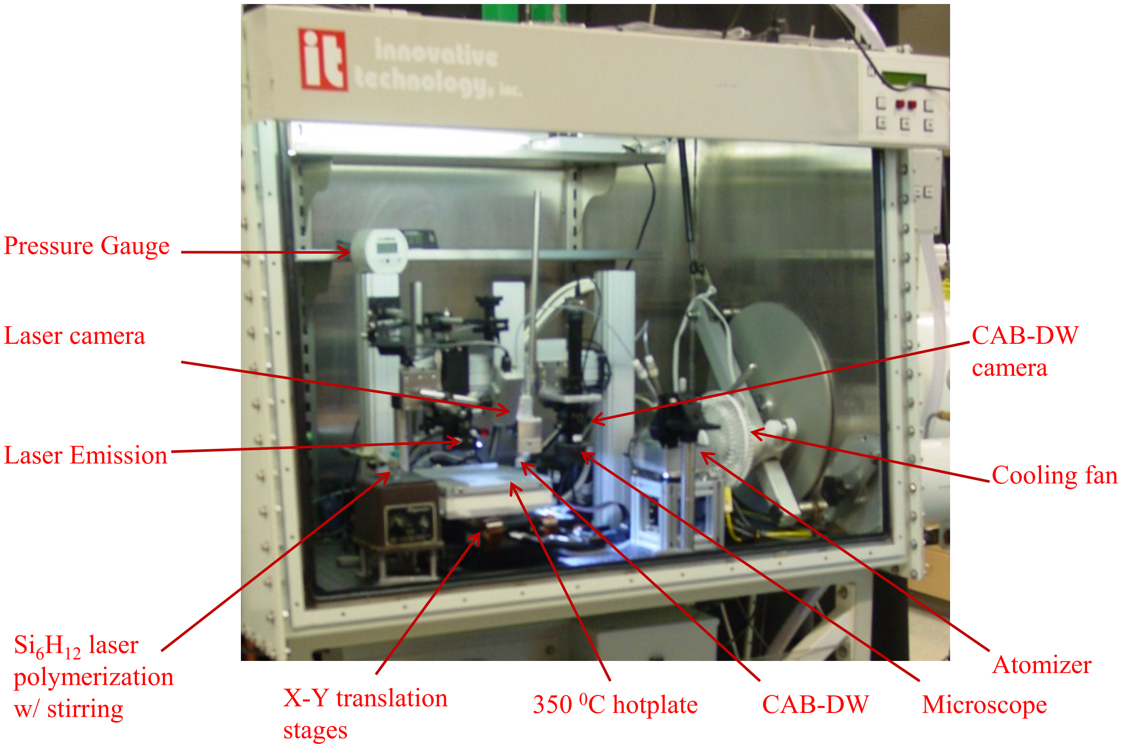

Figure 73. Glovebox setup for CAB-DW of air sensitive materials, with laser sintering and polymerization capability.

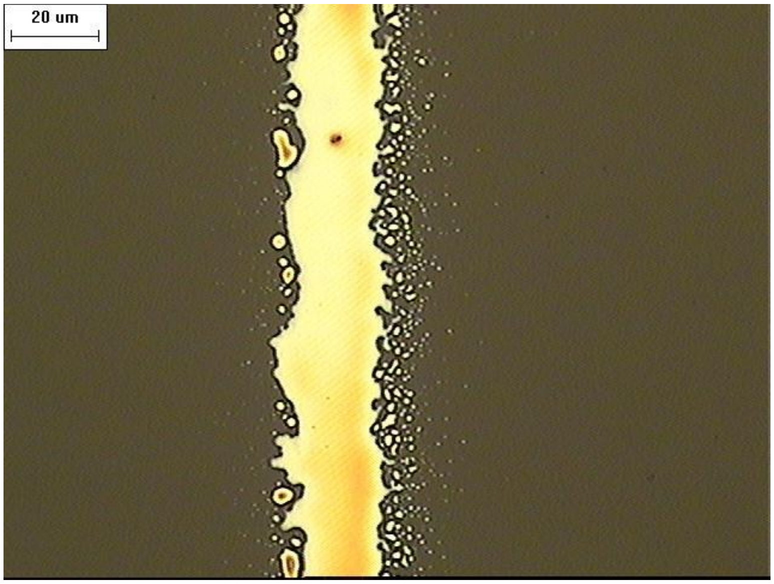

Figure 74. Micrograph of silicon line printed with CAB-DW using CHS ink.

In addition to printing on rigid substrates such as glass, it may be advantageous to print on flexible substrates if a flexible TFT is desired. For proof-of-concept, silicon lines were printed on Kapton film. Similar deposition parameters as describe above were used, but substrate temperature was decreased to 150 °C, and carrier gas was set at 5, 7 and 10 ccm. Results, as shown in Figure 75, show that both line width and thickness increase with carrier gas flow. At 5 ccm, almost no deposit is visible, while at 10 ccm, the deposit is thick enough to crack. In any case, this experiment proves the viability of printing silicon on flexible substrates.

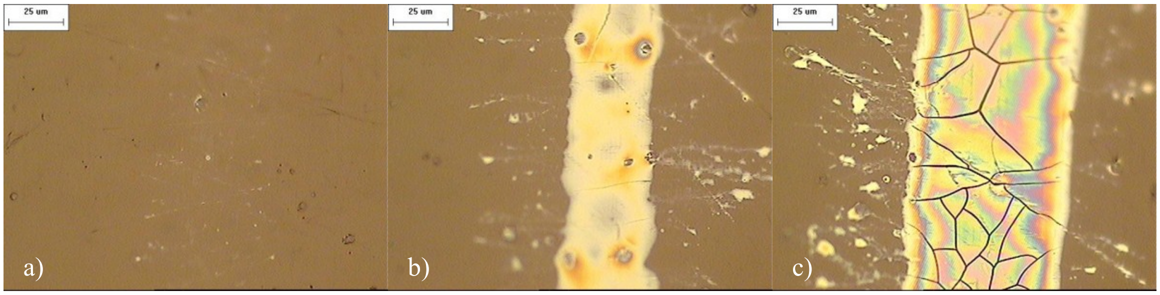

Figure 75. Printed silicon from CHS using CAB-DW on Kapton films with carrier gas flow rates of a) 5 ccm, b) 7 ccm, and c) 10 ccm.

There are several methods to convert the CHS deposits to silicon such as thermal IR and laser annealing. Because laser optics were already installed in the glove box, it seemed reasonable to see whether it was possible to anneal and crystallize the silicon line. A line printed with CHS similar to that described above was laser crystallized with a 355 nm pulsed laser (HIPPO, Newport Corp.). As can be seen in Figure 76a, the laser crystallized the untreated silicon printed line (polysilane) but also ablated a portion of it. A contact profile (Figure 76b) of the non-crystallized portion reveals that the polysilane line is about 6 μm tall and 35 μm wide.

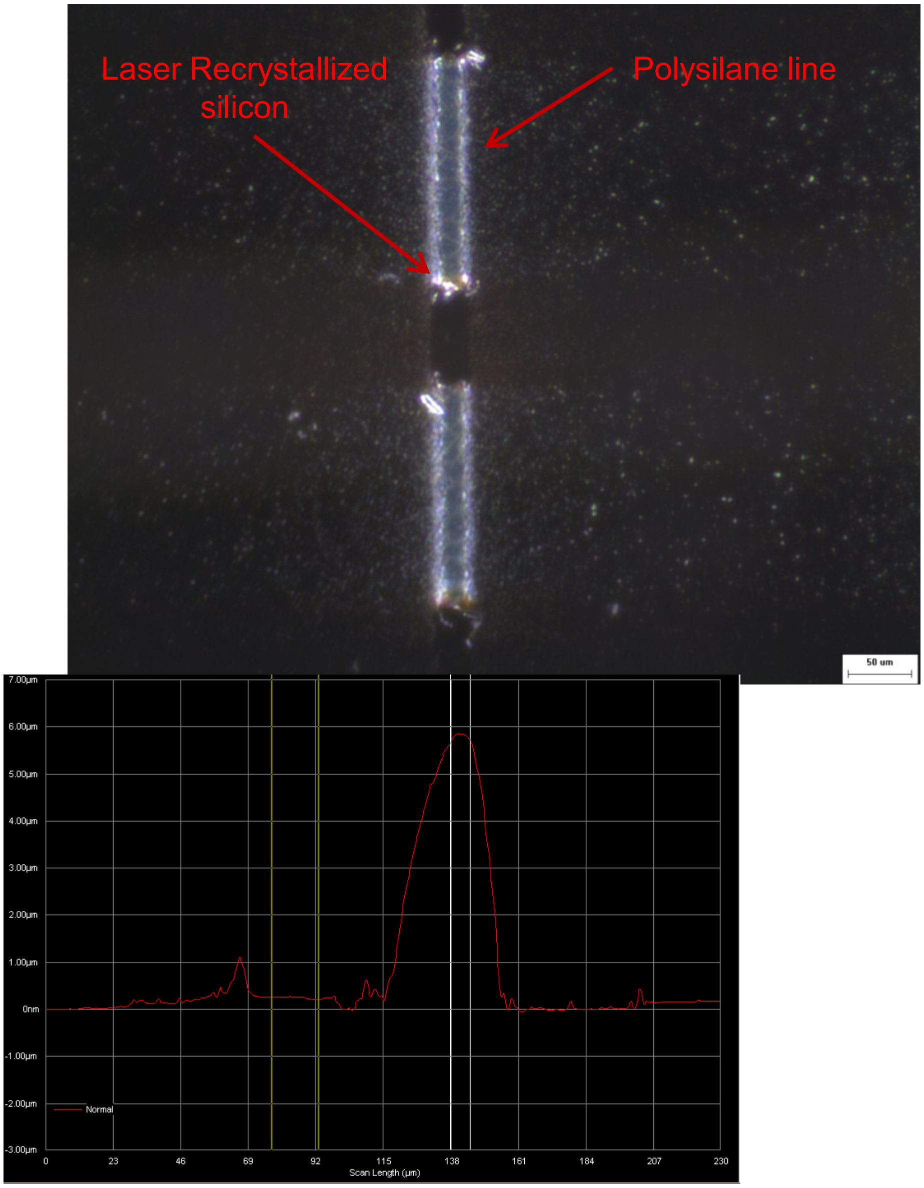

Figure 76. a) micrograph of laser crystallized silicon line, b) optical profile of line.

The next step in printing a transistor was to show it possible to deposit the silicon onto the active region of a TFT. Silver source-drain electrodes with 15 µm channel length and 250 µm channel width were previously printed on silicon wafers as described above. The pre-made substrate was aligned onto the printing platen and silicon was successfully deposited as illustrated below in Figure 77. The sample was heat treated at 350 °C and then tested, but no field effect was seen.

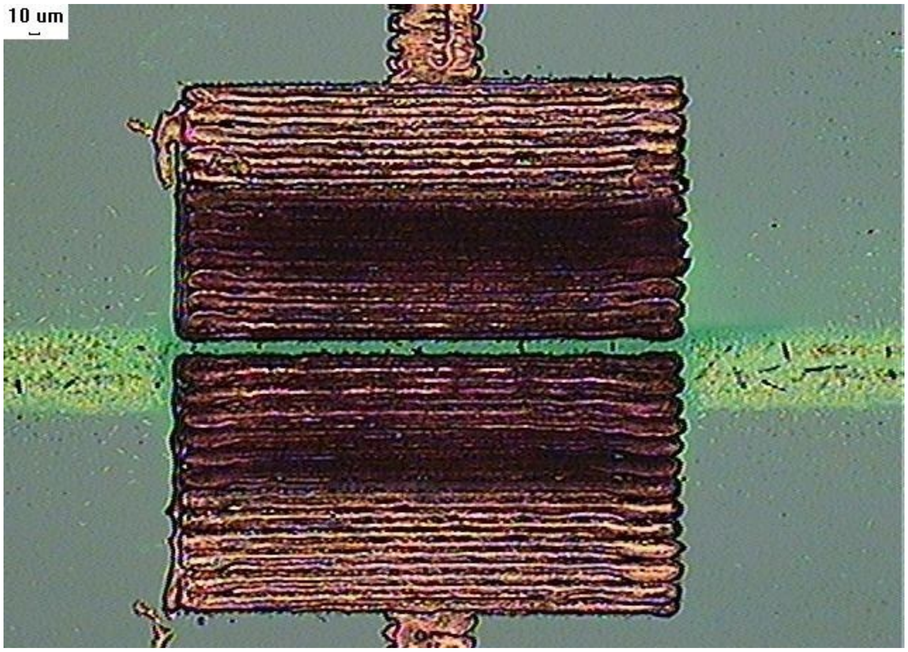

Figure 77. CAB-DW printed bottom-gate transistor with silver source-drain contacts, and silicon active layer.

6.3.3. All-Printed Top Gate TFTs

The final goal of this transistor project is to develop an entirely printed TFT. Transistor source-drain electrodes were printed via CAB-DW using silver nanoparticle ink from NanoSize LTD onto a conductive silicon wafer with 300 nm thick SiO_2 dielectric. The nominal width of the lines was 8 µm, with transistor channel length and width 15 µm and 250 µm, respectively. Once the electrodes were printed and sintered, silicon was deposited in the channel. The next step in the process is to design top-gate transistors which required the use of a dielectric, and a top gate electrode. The dielectric used is PMMA, which was spincoated onto the bottom gate transistors already built. The top gate required the use of a low temperature ink because of the PMMA layer which has a Tg at 120 °C. Several inks were sourced for a low temperature conducting ink; two were chosen (Nanomas Inc., UT Dots Inc.). The challenge of the low temperature inks is that they are usually a xylene based solvent and can be difficult to aerosol print. Nanomas ink (Nanomas Technologies, Endicott, NY) which has a primary particle size of 5 nm and is based on xylene and terpineol for solvents was printed using CAB-DW and tested. It was found that lines of 20 µm width can be printed, but conductivity and edge definition suffered, but should be more than sufficient for testing purposes. The fully printed transistor is detailed below in Figure 78. These top gate transistors were also tested for electrical performance. Results show that a small field effect was present, but that the transistor was sub-optimal. The initial results obtained from this work show that the physical geometry of a top-gate TFT with ~15 µm channel length using all-printed methods can be accomplished. Even though this transistor did not work correctly, the results obtained are still significant. Future work to further develop this TFT structure will include determining the properties of the silicon-silver junction and minimizing the Shottky barrier by using materials such as aluminum which minimize contact resistance.

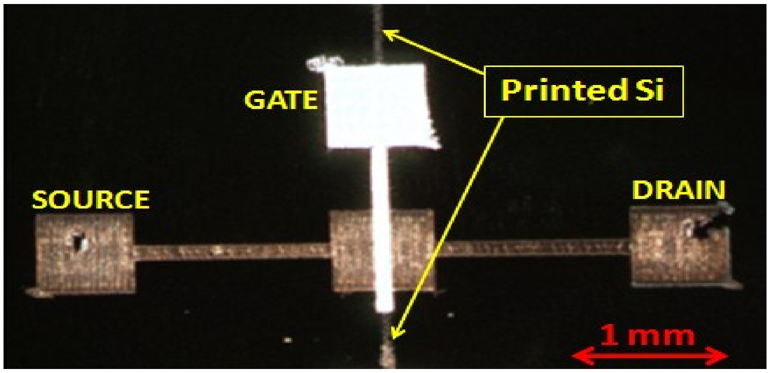

Figure 78. Top gate orientation fully printed silicon-based transistor using Si_6H_{12} converted to a-Si:H active material and PMMA gate dielectric.

6.4. CAB-DW for Solar Cell Metallization

The application of aerosol spray for solar cell metallization layers has been investigated by several groups for the printing of the top metallization layer. Benefits associated with A-DW are a consequence of the ability to print lines as thin as 5 μm which affords a reduction in shadowing, series resistance and production costs. Due to the non-contact approach utilized with aerosol spray, thinner wafers (i.e., 100 μm) can be used without the breakage associated with contact print methods such as screen printing giving a higher number of solar cells per Si single crystal boule [28, 109]. Silver based traces as thin as 7 μm were printed on hetero-junction with intrinsic thin layer (HIT) solar cells produced at NDSU and also in collaboration with NREL. This work was started soon after CAB-DW was discovered and presented at the 2009 IEEE-PV conference in Philadelphia Pa [109] and at the 2010 MRS spring meeting in San Francisco CA [123]. Further research was also accomplished by Jacob Fink who obtained his M.S. in mechanical engineering May, 2012 [124].

6.4.1. Testing of Silver Contacts on In-House Built Solar Cells

The HIT cells built in-house utilize an indium tin oxide (ITO) transparent conducting oxide (TCO) lateral transport layer so no burn-through was required for the top metallization layer [109, 123]. The silver top metallization layer for the solar cells was printed as the final step in a HIT solar cell prototype (Figure 79). An eight inch p-type (1 Ω·cm) wafer 0.5 mm in thickness was used as the substrate for these prototypes. Ohmic contact was made by sputtering (Kurt Lesker CMS-18) a trilayer of Cr/Al/Au at a thickness of 100/150/75 nm. The wafer was next placed into a PECVD system (Oxford

Plasmalab 100+) and thin layers of intrinsic (10 nm thick) and n-type (30 nm thick) silicon were grown using disilane and phosphine as the precursor gases with H_2 dilution. The PECVD processes used in this study are similar to those previously reported by Centurioni et al. [125].

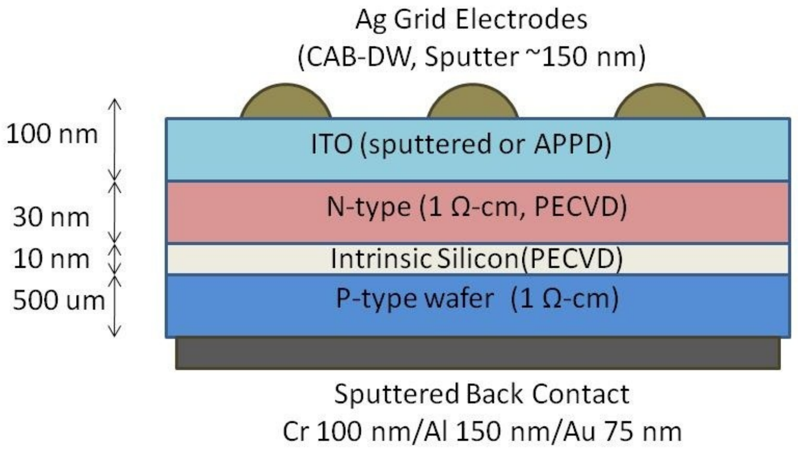

Figure 79. HIT solar cell prototype structure, which is acquired without Ag grid electrodes, from Hoey et al. [109], Copyright 2009 IEEE.

The solar cell test structures were finished by depositing Ag grid lines by either sputtering or CAB-DW. Sputtered Ag 150 nm in thickness utilized a shadow mask with 90 μm line widths and 590 μm spacing. The initial CAB-DW experiments targeted this same line width and spacing. The utility of the CAB-DW process was investigated by selecting much smaller trace widths of 5 μm with spacing of either 37 or 74 μm and line thickness around 500 nm. In all instances, the total length of the Ag grid lines was 1 cm.

The CAB-DW experiments utilized a Ag nanoparticle (primary particle size = 50 nm) ink from NanoSize Ltd. After printing, the Ag was annealed in a nitrogen atmosphere (less than 0.5 ppm O_2) for 60 min at 225 °C. Resistivities in the range of 5 μΩ·cm (i.e., about three times bulk Ag) are generally observed for this recipe [111]. Photographs of the Ag grid lines deposited by CAB-DW are shown in Figure 80 for both the 90 μm (a) and 5 μm (b) lines. Both samples are 1 cm X 1 cm and the total amount of shadowed area is calculated to be a constant around 15%.

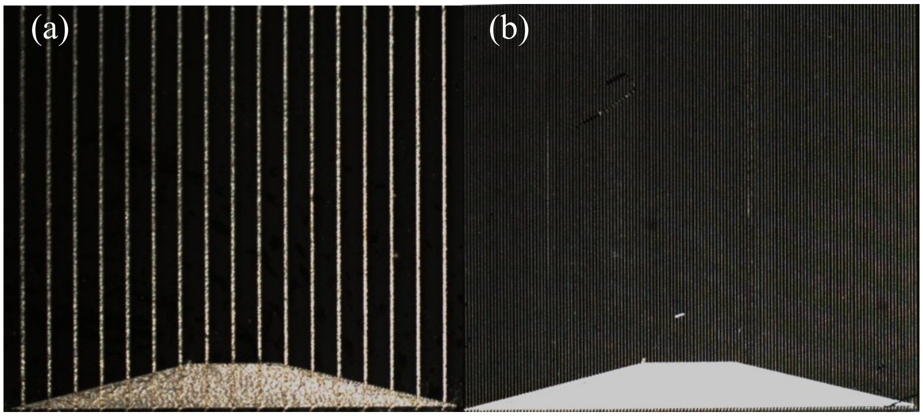

Figure 80. Photographs of Ag top grid arrays prepared by CAB-DW with (a) 90 μm and (b) 5 μm traces, from Hoey et al. [109], Copyright 2009 IEEE.

Solar cells were tested using a PV Measurements Inc. (Boulder, CO) Solar Cell Tester. Illumination is provided by a tungsten lamp and conditioned through an atmospheric spectrum filter to obtain AM 1.5 global illumination for an area of 1 cm^2. Light intensity was calibrated using a GaAs solar cell (18.9% efficient). IV data were obtained using Labview software and a Keithley 2400 sourcemeter. Solar cells were aligned and held in place with a specially designed mount that has an indium metal front contact and a round-tipped probe as a back contact. This test jig is shown in Figure 81.

The solar cell test results reveal that the top metallization layer has a dramatic effect on device performance. A marked improvement was noted for CAB-DW versus sputtered with 90 μm and 5 μm CAB-DW lines exhibiting improved device efficiencies of

31% and 230%, respectively. It is also interesting to note that reducing the number of 5 μm traces by half (i.e., 74 μm spacing) gives an 83% increase in efficiency versus the sputtered silver. This improvement in efficiency is likely due to decreased series resistance given the smaller spacing between metal contacts and the reduced distance the carriers are required to travel through the semiconducting ITO. Perhaps part of this marked difference relates to the high sheet resistance in the ITO layer whereby more closely spaced opaque grids leads to enhanced collection of the carriers into the external circuit.

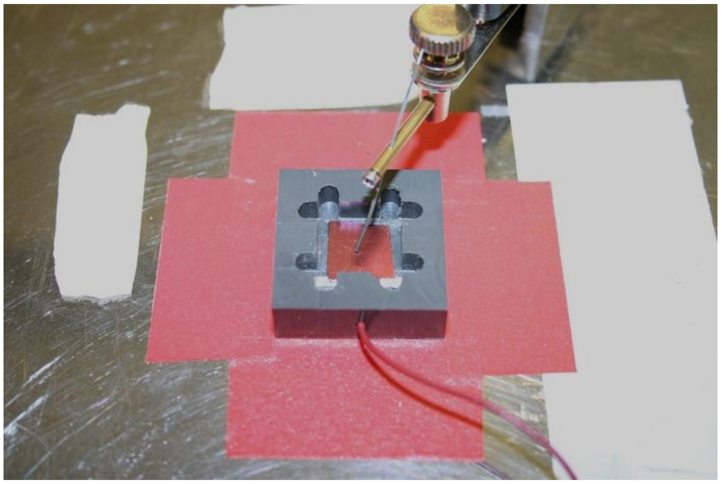

Figure 81. Solar cell test jig, from Hoey et al. [109], Copyright 2009 IEEE.

ITO films prepared by APPD were finished by CAB-DW of Ag with 5 μm trace widths and 74 μm spacing. The preliminary outcome of this study shows the cell prototypes fabricated from APPD exhibit efficiencies about 50% of those that utilized sputtered ITO. This is counterintuitive as the sheet resistance of the former is about five times better than the later and we tentatively ascribe this effect to a difference in the n-type Si / ITO interfaces.

6.4.2. Physical Properties of Printed Silver for Solar Cells

Before any further printing on solar cells, the morphology of the printed lines was first analyzed. Specifically, it is necessary to know the height, width, and area of traces to ensure an appropriate geometry of the conductor is achieved. The geometry of printed lines can be varied using different process parameters (i.e. carrier flow rate, print speed, deposition temperature, ink formulation), or the geometry can be varied by printing over the same location several times. It was found that using multiple print passes to produce a single line (Figure 82) increases both the height and width of the line so that the ratio of height to width is near 1:2, and area of the line increases near linearly with print passes. In this study a maximum height of 13 μm was achieved.

It was found in previous work that the sintering environment had a large effect on the final resistivity of the printed silver lines. To determine the optimum printing atmosphere CAB-DW was used to deposit silver nanoparticle based lines on glass substrates. The samples were subjected to heat treatments of 250 °C and 400 °C for one hour in atmospheres of a) 20% O_2 in N_2, b) N_2, and c) 5% H_2 in N_2 (forming gas). After heat treatment the electrical resistivity of the samples was tested using resistance measurements and trace area measured using an optical profilometer. The results of the test can be seen below in Figure 83. From these results it was shown that annealing the lines in a reducing atmosphere (forming gas) had a dramatic effect on sintered resistivity with a minimum resistivity below 4× bulk silver at 400 °C, and about 8× bulk at 250 °C. From this data it was determined that forming gas was the optimum atmosphere for all sintering.

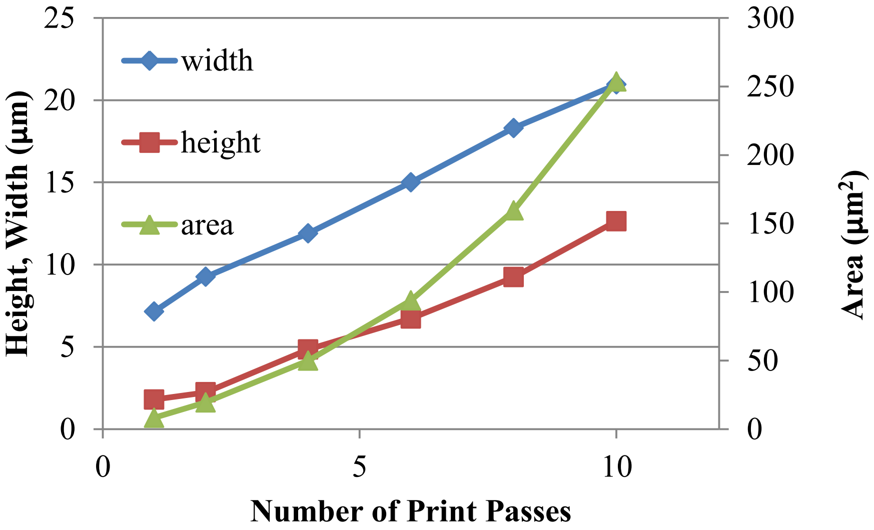

Figure 82. Plot of the effect printing multiple passes using CAB-DW has on the trace width, height, and area.

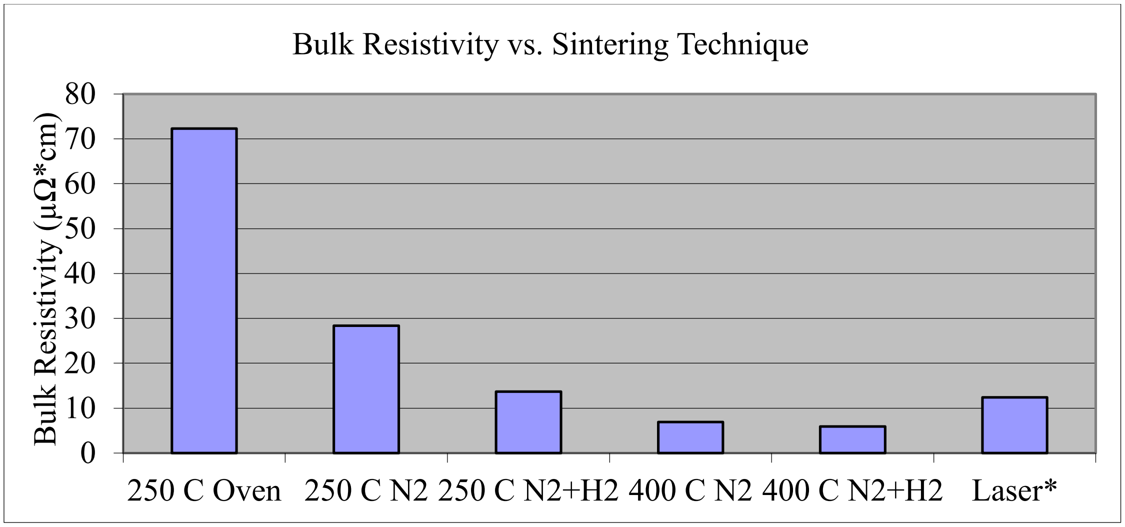

Figure 83. Graph of sintered resistivity for various temperatures and annealing atmospheres using Ag nanoparticle ink.

Silicon solar cells can be sensitive to annealing due to dopant diffusion within the cell. Due to the sensitivity of solar cells the minimum sintering temperature which will provide a stable low resistivity should be used for the metallization layer. To determine the minimum sintering temperatures CAB-DW printed silver lines were annealed at temperatures between 160 °C and 220 °C for 1 hour in forming gas (N_2 + 5% H_2). From the data displayed in Figure 84, the sintering temperature must be at least 180 °C to have a stable low resistance, with trace resistance decreasing with increasing sintering temperature. To allow for process variations and impose a safety factor to the sintering, the chosen anneal temperature for the silver nanoparticle traces on the SHJ cells was chosen to be 200 °C. This temperature will reduce the trace resistance with minimal degradation to the solar cell performance.

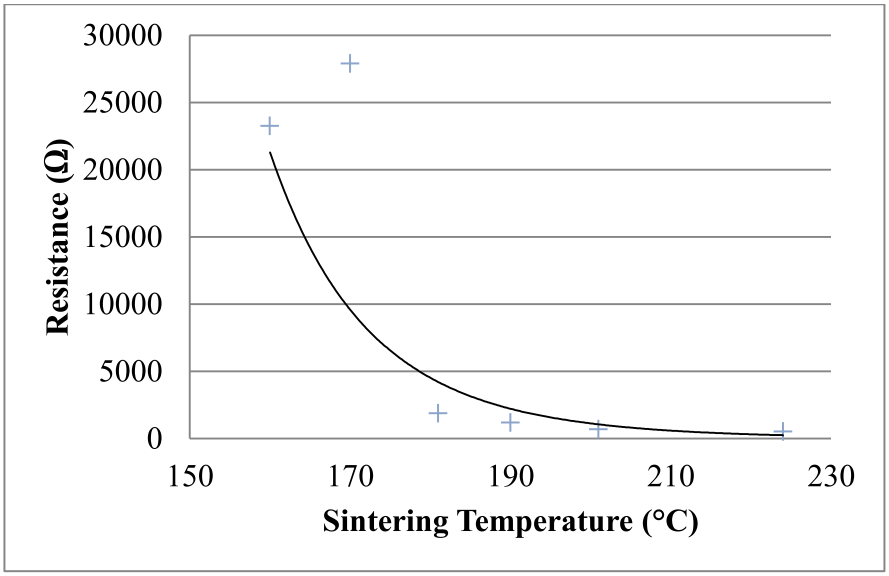

Figure 84. Sintered temperature vs. silver trace resistance in forming gas.

The contact resistance of the silver metallization layer to the ITO must be ascertained to ensure that the series resistance of the cell will be minimized. The Transmission Line Method was used to determine the contact resistance of the printed silver traces. This test consists of printing a series of pads 300×300 μm^2 on ITO coated glass at distances ranging from 100 µm to 1 mm which are sintered at 200 °C for one hour in forming gas and measuring the resistance between the pads at each distance.

Resistance was measured using an Agilent B1500A semiconductor analyzer with 4-point probe measurements to preclude any error due to contact of the probes. Results of the test are shown below in Figure 85 where the resistance between the lines decreases as the spacing between the pads decreases. The contact resistance is found by calculating the resistance at the limit when the distance between the pads is zero. This can't be measured directly, but can be found by fitting a line to the data, and using the y-intercept as the zero-distance resistance. The contact resistance was found to be 9.8 mΩ*cm^2, a value about 20× greater than some results reported by NREL, but definitely acceptable for preliminary evaluations.

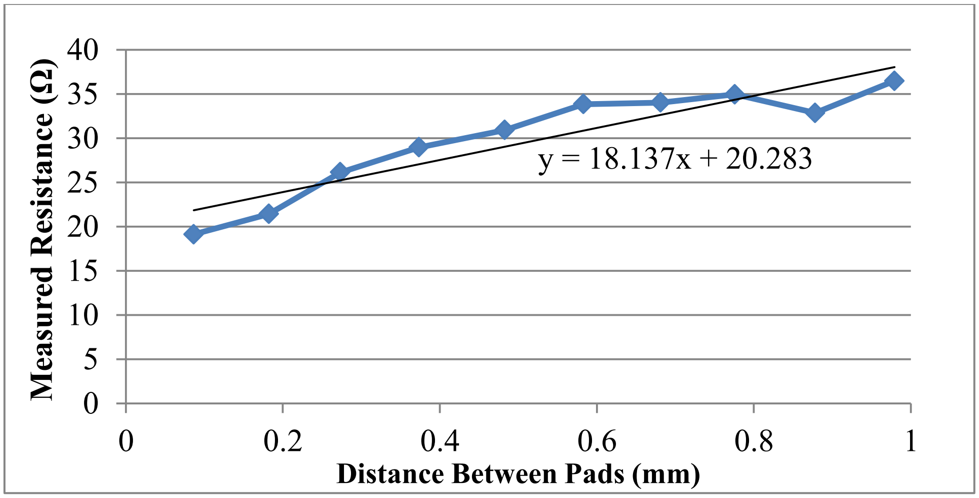

Figure 85. Measured silver contact pads resistance vs. the distance between the pads.

After all printing parameters were determined; the solar cell grids were designed for a total of 4 passes of printing which should give ample material deposition to minimize the series resistance. The samples now labeled "25 µm Control / 4 pass" and "5 µm / 4 pass" were printed and analyzed via optical profilometry (Figure 86), where the resultant lines have an overall area of 103 and 10 μm^2 respectively. The total conductor cross-sectional area for the fingers in a 1×1 cm^2 cell are 821.4 μm^2 for the "25 μm Control / 4 pass", and 392.7 μm^2 for the "5 μm / 4 pass".

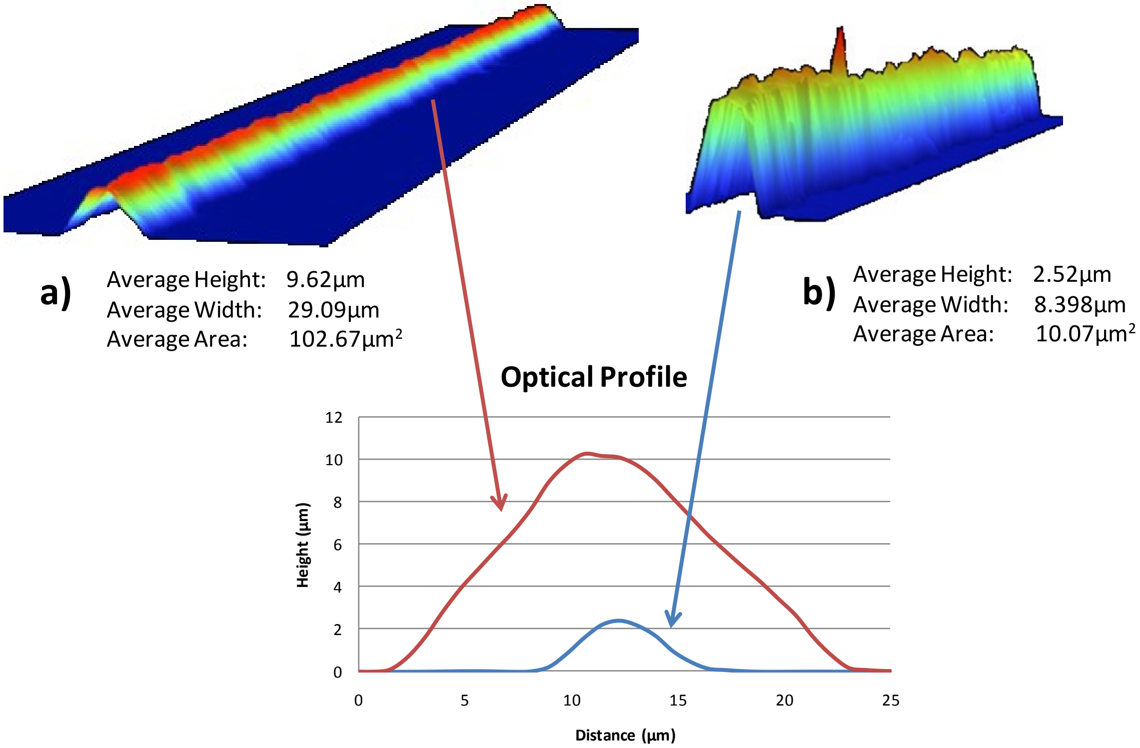

Figure 86. Optical profile measurements of solar cell traces a) "25 μm Control / 4 pass", and b) "5 μm / 4 pass".

SEM images of the printed lines were also obtained (Figure 87) where a top view of a single trace from the "25 μm Control / 4 pass" and "5 μm / 4 pass" patterns are displayed in a) and b) and cross sections in c) and d), respectively. The cross section was fashioned by scribing the glass substrate on the back side and fracturing it. It appears that some shrinkage occurs on the "25 μm Control / 4 pass" traces, but other than that both traces appear well adhered to the substrate (except near the fracture site in d), minimal overspray, and have a semi-cylindrical structure. It is important to note that this semi-cylindrical structure may aid in reducing the reflectance of the traces as compared to a flat structure typically seen with sputtered and evaporated contacts.

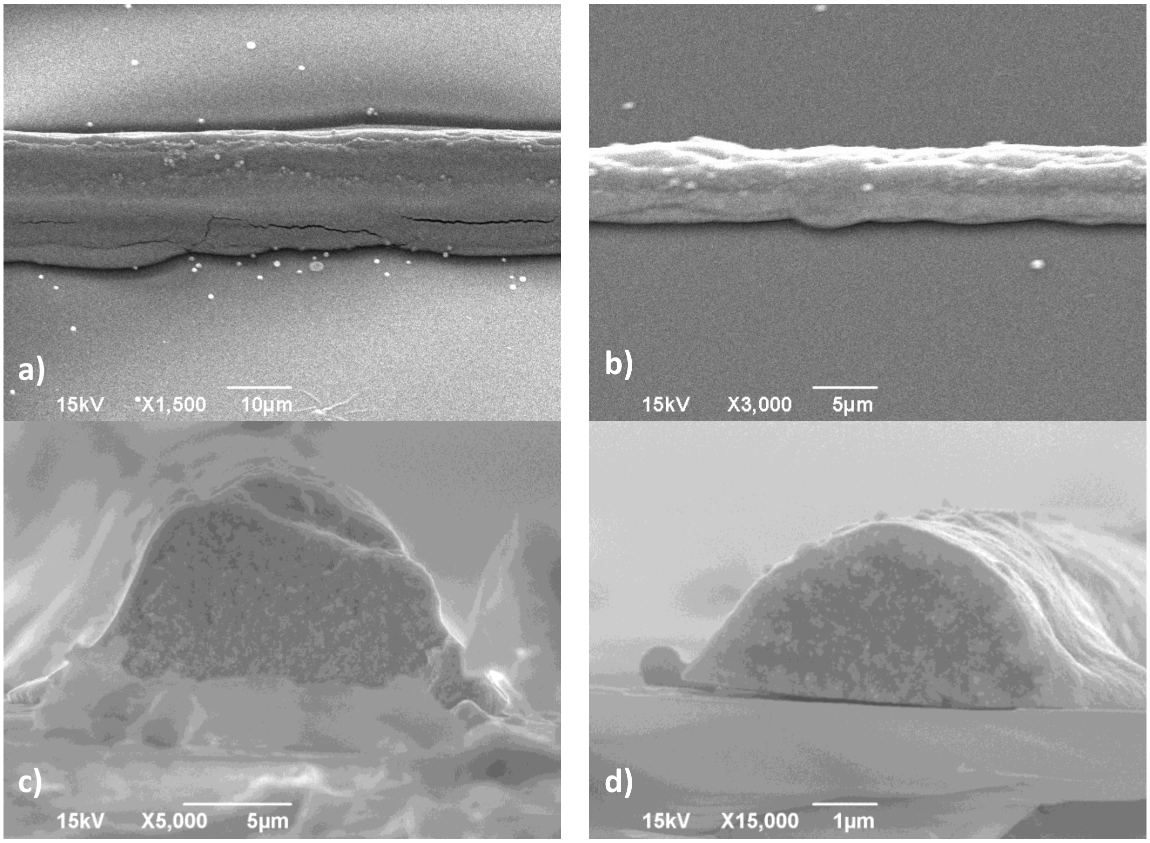

Figure 87. SEM images of a top view of a) “25 µm Control / 4 pass” trace, b) “5 µm 4 pass” trace, and cross-sectional view of c) “25 µm Control / 4 pass” trace , and d) “5 µm / 4 pass” trace.

Results from the first set of printing HIT solar cells show that there is indeed a benefit to printing with smaller line widths as far as improving overall solar cell efficiency. The increase in efficiency was found a result from both the decrease in series resistance of the solar cell, and decrease in shadowing due to the shape of the printed traces. As already discussed, internal reflection can have a large part in the decrease of shadowing. Proof of decreased shadowing was futher confirmed by calculating and measuring the actual reflectance of the printed lines. The silver traces were printed onto borosilicate glass slides with 10% area coverage in patterns of 20 mm × 20 mm with 9 print passes using the CAB-DW nozzle with silver nanoparticle ink. After printing, the samples were sintered at 250°C for 1 hour in N_2. By looking at the cross section of some of the printed traces using a contact profilometer and calculating that the critical angle for internal reflectance is about 20.4°, an effective shadowing of the traces was calculated to be as low as 46.4% of the geometric shadowing [126]. Next, the samples were encapsulated with Ethylene Vinyl Acetate (EVA) and one more borosilicate glass slide. The reflectance of the sample was measured using an integrating sphere (QEX7 Solar Cell Spectral Response/ QE/IPCE, PV Measurements, Boulder CO) from 400 nm to 1400 nm light wavelength. Normalized reflectance data can be seen below in Figure 88. Results show an average reflectance of only 51% of the geometric shadowing, which is in close agreement with the calculated result.

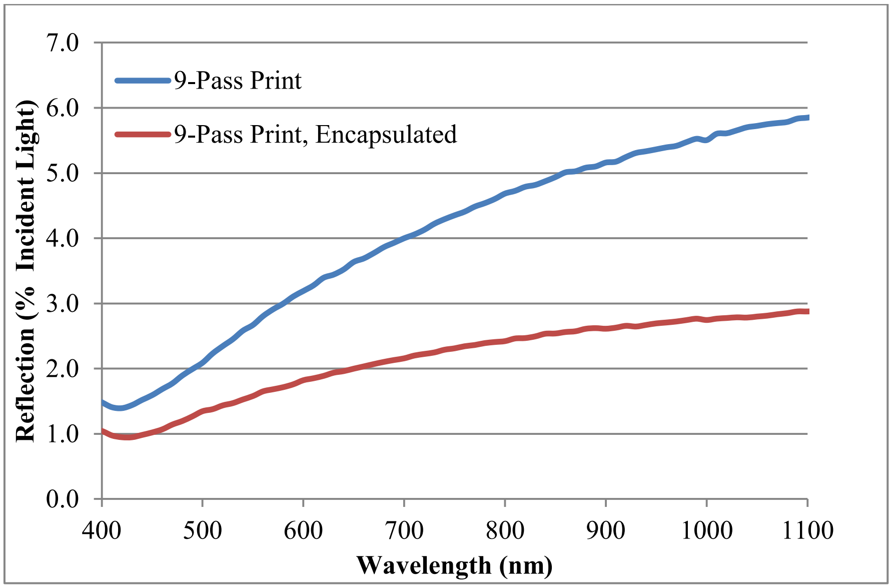

Figure 88. Reflectance vs. wavelength for 9-pass printed silver traces, reprinted from Fink [126].

6.4.3. Contacts on NREL Provided Solar Cells

Top contacts on NREL procured solar cells were printed using the silver nanoparticle ink, and CAB-DW nozzle with 100 µm final nozzle diameter. The substrate was heated to 100 °C for deposition with a print speed of 10 mm/s. After deposition the samples were placed in a tube furnace under forming gas atmosphere and annealed for 1 hour at 200 °C. Three finished cells can be seen below in Figure 89. Sample 1 is a cell with the "25 µm Control / 4 pass" pattern which replicates NREL's. Sample 2 is the "5 µm Control / 2 pass" pattern which has minor printing errors due to a clogged nozzle during printing. Sample 3 is the "5 µm Control / 4 pass" pattern.

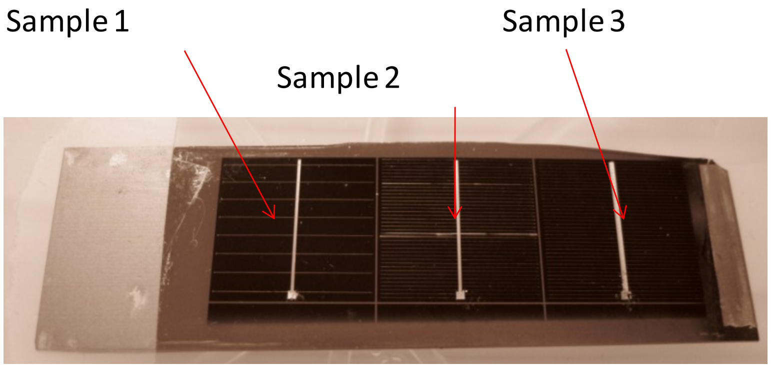

Figure 89. Optical image of completed NREL solar cells.

Initial data for solar cell tests reveals that the thinner lines in Sample 3 do indeed increase the overall cell efficiency by over 1% absolute compared to Sample 1! The increased efficiency in Sample 3 resulted primarily from the increased fill factor, 51% vs 44% for Sample 3 and 1 respectively. The V_{oc} slope was also less for Sample 3, which equates to a decreased series resistance in the cell. Sample 2 did not show improved performance vs. Sample 1 which is assumed to be due to the decreased trace area from only 2 printing passes. The decreased trace area increased the series resistance to a value similar to Sample 1, and therefore no improvement in cell efficiency was observed.

The optimal geometry for the printed lines can be calculated using a Tranfer Length Model (TLM) which is designed to account for the power loss which occurs in the traces due to bulk resistance (ΔP_F) and contact resistance (ΔP_C), ohmic loss in the ITO layer (ΔP_E), and shadowing of the cell (ΔP_{FS}). Using the properties from the solar cells procured from NREL, the optimum finger width is calculated to be 20.5 µm as shown in Figure 90. As an example, the minimum widths found from other technologies are displayed in the figure. In addition, the mass loading of silver which would be required on the solar cell is displayed using the right axis where it can be seen that mass loading is directly proportional to line width.

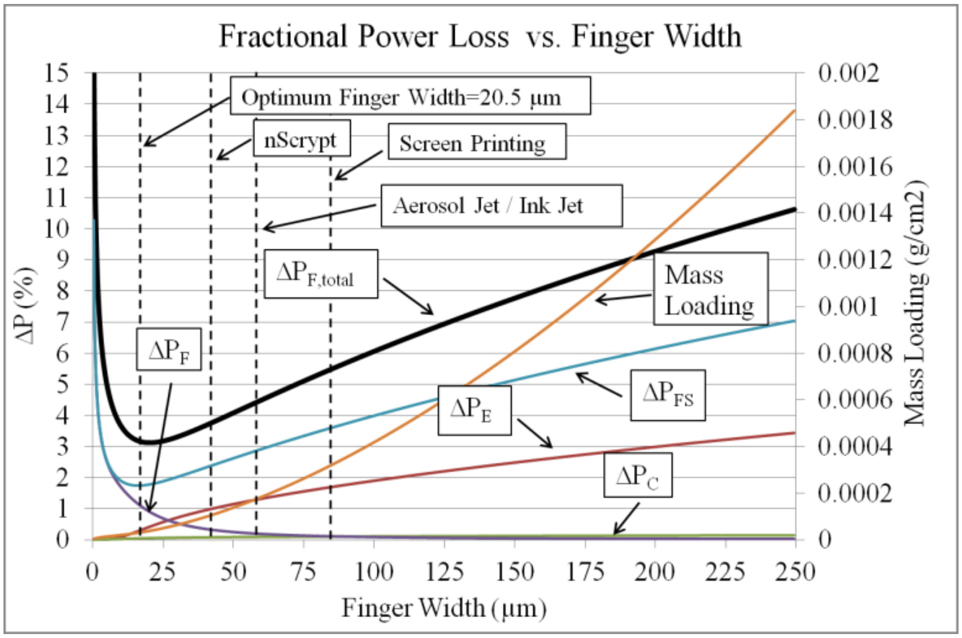

Figure 90. Power loss curve for varying finger width of top metallization layer, reprinted from Fink [126].

Additional top contacts on NREL solar cells were printed using silver nanoparticle ink from Novacentrix using an approximately 20 µm wide finger width. These lines were made by printing on a heated substrate with 20 passes. After printing, the samples were sintered at 300 °C for 1 hour in air. Cell efficiencies were measured, with a peak efficiency of 17.2% achieved, which represents a substantial improvement from previous results. In addition, this result shows the viability of CAB-DW for printing high-efficiency solar cells.

7. CONCLUSIONS

The ability to understand and model aerosol flow physics and compare it to experimental designs is paramount in improving aerosol direct-write technology. All A-DW technologies still suffer from minor overspray and non-optimum line width. One challenge with liquid aerosol technologies is not in the printing itself, but rather in the ink formulation. For example, metal traces can be printed using nanoparticle or metalorganic based inks, but after deposition, the inks must be post processed. This post processing adds an additional cost to the overall process and can limit the ability to print on some temperature sensitive substrates. In addition, a sub-bulk conductivity due to porosity of the deposits and incomplete sintering is common. If these difficulties are overcome with improved aerosol focusing and ink technology, the applications of A-DW will greatly benefit from the decreased feature size, and increased conductivity afforded. Table 6 summarizes the main characteristics of the A-DW technologies including line width, deposition speed, special requirements, and whether post processing is required.

Table 6. Summary of A-DW technology print system characteristics, reprinted from Hoey et al. [17].

Method	**Minimum line width (µm)**	**Deposition speed (mm/s)**	**Vacuum-required**	**Overspray scrubber required**	**VOC concern**	**Post Processing Required**
Aerosol Jet	< 10	200	No	Yes	Yes	Yes
CAB-DW	< 5	200	No	Yes	Yes	Yes
Aero-dynamic lenses	~10	0.01	Yes	Yes	Yes	No
MCS	50	>10*	No	Yes	No	No

*Deposition speeds greater than 10 mm/s are possible, but have not been experimentally validated.

Aerosol direct-write is a relatively new class of technologies rapidly becoming available for commercial use in electronic applications where a non-contact, high-resolution, and 3D capable tool is required. Aerosol Jet is the leading commercial technology available for A-DW, with CAB-DW, MCS, and aerosol lens focusing still in development stages. These devices all rely on aerodynamic focusing to create controllably fine deposits. The understanding of the physics of the fluid-particle interactions enables developers of A-DW technologies to further improve these devices reducing overspray, improving resolution, and decreasing tool down-time. Recent advancements in aerosol visualization and measurement using shadowgraphy and other techniques has led to an improved understanding of aerosol focusing pertaining to A-DW technologies.

In this work, the physics and methods of characterizing aerosol flow were presented, along with beam width calculations and a correction to Saffman force. The models and experience with aerosol particle-laden flows led to the discovery and initial development of three new technologies; 1) CAB-DW, 2) MCS, 3) a convergent-straight nozzle.

The coupling of A-DW technology to electronics leads to several advantages over traditional techniques including reduced costs, reduced time to startup and improved feature resolution. A-DW has been shown for printing features for electronic devices such as TFTs and solar cells. A newer technology, MCS, is not used in many applications, but has been shown capable of printing without post processing, a feature which could reduce production costs. The overall development of A-DW technologies may lead to a more widespread use for microelectronics applications especially those where rapid prototyping is employed.

REFERENCES

1. A. D. Halvorsen, P. Vaidya, M. Robinson, and D. L. Schulz, "Transforming a laser micromachiner into a direct-write tool for electronic materials," *Journal of microelectronics and electronic packaging,* vol. 5, pp. 116-121, 2008.
2. K. K. B. Hon, L. Li, and I. M. Hutchings, "Direct writing technology—Advances and developments," *CIRP Annals - Manufacturing Technology,* vol. 57, pp. 601-620, 2008.
3. W. Liu and J. DuPont, "Fabrication of functionally graded TiC/Ti composites by laser engineered net shaping," *Scripta materialia,* vol. 48, pp. 1337-1342, 2003.
4. M. J. Renn, G. Marquez, B. King, M. Essien, and W. Miller, "Flow-and laser-guided direct write of electronic and biological components," *Direct-Write Technologies for Rapid Prototyping Applications; Pique, A., Chrisey, DB, Eds.; Academic Press: San Diego, CA,* pp. 475–492, 2002.
5. (2012). *Mesoscribe Technologies*. Available: www.mesoscribe.com
6. D. B. Chrisey, A. Pique, R. Modi, H. D. Wu, R. C. Y. Auyeung, and H. D. Young, "Direct writing of conformal mesoscopic electronic devices by MAPLE DW," *Applied Surface Science,* vol. 168, pp. 345-352, Dec 2000.
7. A. Lutfurakhmanov, G. K. Loken, D. L. Schulz, and I. S. Akhatov, "Capillary-based liquid microdroplet deposition," *Applied Physics Letters,* vol. 97, Sep 2010.
8. I. S. Akhatov, J. M. Hoey, O. F. Swenson, and D. L. Schulz, "Aerosol flow through a long micro-capillary: collimated aerosol beam," *Microfluidics and Nanofluidics,* vol. 5, pp. 215-224, Aug 2008.

9. J. M. Hoey, I. S. Akhatov, O. F. Swenson, and D. L. Schulz, "Convergent-divergent-convergent nozzle focusing of aerosol particles for micron-scale direct writing," 2009/0053507, 2009.

10. R. A. Sailer and J. M. Hoey, "Micro cold spray direct write technology for printed micro electronics applications," US Patent 61/591,365, 2012.

11. S. Bhattacharya, A. Lutfurakhmanov, J. M. Hoey, O. F. Swenson, and R. A. Sailer, "Micro Cold Spray Direct Write Process," presented at the ASME International Mechanical Engineering Congress and Exposition, Houston, Texas, USA, 2012.

12. L. Qi, "Aerosol printing of colloidal nanocrystals by aerodynamic focusing," Ph.D., Materials Science and Engineering, University of Minnesota, Minneapolis, 2010.

13. L. J. Qi, P. H. McMurry, D. J. Norris, and S. L. Girshick, "Impact dynamics of colloidal quantum dot solids," *Langmuir,* vol. 27, pp. 12677-12683, Oct 2011.

14. S. L. Girshick, "Aerosol processing for nanomanufacturing," *Journal of Nanoparticle Research,* vol. 10, pp. 935-945, Aug 2008.

15. L. J. Qi, P. H. McMurry, D. J. Norris, and S. L. Girshick, "Micropattern deposition of colloidal semiconductor nanocrystals by aerodynamic focusing," *Aerosol Science and Technology,* vol. 44, pp. 55-60, 2010.

16. M. J. Renn, "Direct Write™ System," USA Patent 7108894 B2, 2006.

17. J. M. Hoey, A. Lutfurakhmanov, D. L. Schulz, and I. S. Akhatov, "A review on aerosol-based direct-write and its applications for microelectronics " *Journal of Nanotechnology,* vol. 2012, pp. 1-22, 2012.

18. (2012). *Sono-Tek Homepage*. Available: www.sono-tek.com

19. (2012). *Sonaer Ultrasonics Homepage*. Available: www.sonozap.com

20. S. C. Tsai, Y. L. Song, C. S. Tsai, Y. F. Chou, and C. H. Cheng, "Ultrasonic atomization using MHz silicon-based multiple-Fourier horn nozzles," *Applied Physics Letters,* vol. 88, Jan 2006.

21. J. Y. Ju, Y. Yamagata, H. Ohmori, and T. Higuchi, "High-frequency surface acoustic wave atomizer," *Sensors and Actuators a-Physical,* vol. 145, pp. 437-441, Jul-Aug 2008.

22. A. Qi, L. Y. Yeo, and J. R. Friend, "Interfacial destabilization and atomization driven by surface acoustic waves," *Physics of Fluids,* vol. 20, Jul 2008.

23. J. Friend and L. Y. Yeo, "Microscale acoustofluidics: Microfluidics driven via acoustics and ultrasonics," *Reviews of Modern Physics,* vol. 83, pp. 647-704, Jun 2011.

24. N. S. Kim and K. N. Han, "Future direction of direct writing," *Journal of Applied Physics,* vol. 108, Nov 2010.

25. B. King and M. Renn, "Aerosol Jet direct write printing for mil-aero electronic applications," ed. www.optomec.com, 2009.

26. V. R. Marinov, Y. A. Atanasov, A. Khan, D. Vaselaar, A. Halvorsen, D. L. Schulz, and D. B. Chrisey, "Direct-write vapor sensors on FR4 plastic substrates," *IEEE Sensors Journal,* vol. 7, pp. 937-944, May-Jun 2007.

27. M. Maiwald, C. Werner, V. Zoellmer, and M. Busse, "INKtelligent printed strain gauges," *Sensors and Actuators a-Physical,* vol. 162, pp. 198-201, Aug 2010.

28. M. F. A. M. van Hest, "Direct write approaches for metallization," presented at the 2nd workshop on metallization of crystalline silicon solar cells, Cibstabcem Germany, 2010.

29. M. F. A. M. van Hest, S. E. Habas, J. M. Underwood, R. M. Pasquarelli, P. Hersh, A. Miedaner, C. J. Curtis, and D. S. Ginley, "Direct write metallization for photovoltaic cells and scaling thereof," in *35th IEEE PVSC*, Honolulu, HI, 2010, pp. 3626-3628.

30. S. E. Habas, H. A. S. Platt, M. van Hest, and D. S. Ginley, "Low-cost inorganic solar cells: From ink to printed device," *Chemical Reviews,* vol. 110, pp. 6571-6594, Nov 2010.

31. K. Drew, S. Hopman, M. Horteis, S. W. Glunz, and F. Granek, "Combining laser chemical processing and aerosol jet printing: a laboratory scale feasibility study," *Progress in Photovoltaics,* vol. 19, pp. 253-259, May 2011.

32. M. Horteis and S. W. Glunz, "Fine line printed silicon solar cells exceeding 20% efficiency," *Progress in Photovoltaics,* vol. 16, pp. 555-560, Nov 2008.

33. A. Mette, P. L. Richter, M. Horteis, and S. W. Glunz, "Metal aerosol jet printing for solar cell metallization," *Progress in Photovoltaics,* vol. 15, pp. 621-627, Nov 2007.

34. C. E. Folgar, C. Suchicital, and S. Priya, "Solution-based aerosol deposition process for synthesis of multilayer structures," *Materials Letters,* vol. 65, pp. 1302-1307, May 2011.

35. M. Ha, Y. Xia, A. A. Green, W. Zhang, M. J. Renn, C. H. Kim, M. C. Hersam, and C. D. Frisbie, "Printed, sub-3V digital circuits on plastic from aqueous carbon nanotube inks," *ACS nano,* vol. 4, 2010.

36. J. H. Cho, J. Lee, Y. Xia, B. Kim, Y. Y. He, M. J. Renn, T. P. Lodge, and C. D. Frisbie, "Printable ion-gel gate dielectrics for low-voltage polymer thin-film transistors on plastic," *Nature Materials,* vol. 7, pp. 900-906, Nov 2008.

37. L. Herlogsson, M. Colle, S. Tierney, X. Crispin, and M. Berggren, "Low-voltage ring oscillators based on polyelectrolyte-gated polymer thin-film transistors," *Advanced Materials,* vol. 22, pp. 72-76, Jan 2010.

38. Y. Xia, W. Zhang, M. J. Ha, J. H. Cho, M. J. Renn, C. H. Kim, and C. D. Frisbie, "Printed sub-2 V gel-electrolyte-gated polymer transistors and circuits," *Advanced Functional Materials,* vol. 20, pp. 587-594, Feb 2010.

39. C. S. Jones, X. J. Lu, M. Renn, M. Stroder, and W. S. Shih, "Aerosol-Jet-printed, high-speed, flexible thin-film transistor made using single-walled carbon nanotube solution," *Microelectronic Engineering,* vol. 87, pp. 434-437, Mar 2010.

40. J. Vaillancourt, H. Y. Zhang, P. Vasinajindakaw, H. T. Xia, X. J. Lu, X. L. Han, D. C. Janzen, W. S. Shih, C. S. Jones, M. Stroder, M. Y. H. Chen, H. Subbaraman, R. T. Chen, U. Berger, and M. Renn, "All ink-jet-printed carbon nanotube thin-film transistor on a polyimide substrate with an ultrahigh operating frequency of over 5 GHz," *Applied Physics Letters,* vol. 93, Dec 2008.

41. M. J. Renn, B. H. King, M. Essien, and L. J. Hunter, "Apparatuses and method for maskless mesoscale material deposition," US Patent 7045015, 2006.

42. "ANSYS CFX-Solver Theory Guide," ed, 2011.

43. I. Akhatov, J. M. Hoey, D. Thompson, A. Lutfurakhmanov, Z. Mahmud, O. F. Swenson, D. L. Schulz, and A. N. Osiptsov, "Aerosol flow through a micro-nozzle," in *ASME 2nd Micro/Nanoscale Heat & Mass Transfer International*, 2009.

44. C. T. Crowe, M. Sommerfeld, and Y. Tsuji, *Multiphase flows with droplets and particles*: CRC press, 1998.

45. I. Kim, S. Elghobashi, and W. A. Sirignano, "On the equation for spherical-particle motion: effect of Reynolds and acceleration numbers," *Journal of Fluid Mechanics,* vol. 367, pp. 221-253, Jul 1998.

46. J. S. Marshall, "Discrete-element modeling of particulate aerosol flows," *Journal of Computational Physics,* vol. 228, pp. 1541-1561, Mar 2009.

47. F. Odar and W. S. Hamilton, "Forces on a sphere accelerating in a viscous fluid," *Journal of Fluid Mechanics,* vol. 18, pp. 302-314, 1964.

48. J. Y. Ran, L. Zhang, Q. Tang, and M. D. Xin, "Numerical simulation of the particle motion characteristics in boundary layer of gas-solid rotary flow," *Journal of Fluids Engineering-Transactions of the Asme,* vol. 128, pp. 596-601, May 2006.

49. P. G. Saffman, "Lift on a small sphere in a slow shear flow," *Journal of Fluid Mechanics,* vol. 22, pp. 385-&, 1965.

50. R. I. Nigmatulin, *Dynamics of multiphase media* vol. 1,2. New York: Hemisphere, 1991.

51. P. A. Baron, P. Kulkarni, and K. Willeke, *Aerosol measurement: principles, techniques, and applications*: Wiley, 2011.

52. G. G. Stokes, "On the effect of the internal friction of fluids on the motion of pendulums," *Transactions of the Cambridge Philosophical Society,* vol. 9, pp. 8-108, 1851.

53. J. F. De la Mora and P. Riesco-Chueca, "Aerodynamic focusing of particles in a carrier gas," *Journal of Fluid Mechanics,* vol. 195, pp. 1-21, Oct 1988.

54. Z. G. Li and H. Wang, "Drag force, diffusion coefficient, and electric mobility of small particles. I. Theory applicable to the free-molecule regime," *Physical Review E,* vol. 68, Dec 2003.

55. R. A. Millikan, "Coefficients of slip in gases and the law of reflection of molecules from the surfaces of solids and liquids," *Physical Review,* vol. 21, pp. 217-238, Mar 1923.

56. R. W. Johnson, *The handbook of fluid dynamics*. Washington D.C.: CRC Press, 1998.

57. E. Cunningham, "On the velocity of steady fall of spherical particles through fluid medium," *Proceedings of the Royal Society of London Series a-Containing Papers of a Mathematical and Physical Character,* vol. 83, pp. 357-365, Mar 1910.

58. D. J. Carlson and R. F. Hoglund, "Particle drag and heat transfer in rocket nozzles," *AIAA,* vol. 2, pp. 1980-1984, 1964.

59. M. Knudsen and S. Weber, "Luftwiderstand gegen die langsame bewegung kleiner kugeln," *Amm. Physics,* vol. 36, pp. 981-994, 1911.

60. R. V. Mallina, A. S. Wexler, and M. V. Johnston, "High-speed particle beam generation: Simple focusing mechanisms," *Journal of Aerosol Science,* vol. 30, pp. 719-738, Jul 1999.

61. M. D. Allen and O. G. Raabe, "Re-evaluation of Millikan's oil-drop data for the motion of small particles in air," *Journal of Aerosol Science,* vol. 13, pp. 537-547, 1982.

62. I. Langmuir, "Filtration of aerosols and development of filter materials," *Office of Scientific Research and Development,* 1942.

63. C. N. Davies, "Definitive equations for the fluid resistance of spheres," *Proceedings of the Physical Society of London,* vol. 57, pp. 259-270, 1945.

64. W. DeMarcus and J. W. Thomas, "Theory of a diffusion battery," *Oak Ridge National Laboratory,* p. 26, 1952.

65. A. Reif, "Aviation Medicine Selected Reviews," C. S. White, I. Lovelace, W.R., and F. G. Hirsch, Eds., ed: Pergamon Press, Oxford, 1958.

66. N. A. Fuchs, *The mechanics of aerosols*. Oxford: Pergamon Press, 1964.

67. B. Dahneke, J. Hoover, and Y. S. Cheng, "Similarity theory for aerosol beams," *Journal of Colloid and Interface Science,* vol. 87, pp. 167-179, 1982.

68. R. L. Buckley and S. K. Loyalka, "Cunningham correction factor and accommodation coefficient - interpretation of Millikan data," *Journal of Aerosol Science,* vol. 20, pp. 347-349, 1989.

69. R. Clift, J. R. Grace, and M. E. Weber, *Bubbles, drops, and particles*. Mineola, NY: Dover Publications Inc. , 2005.

70. L. Schiller and A. Nauman, "A drag coefficient correction," *V.D.I. Zeitung,* vol. 77, pp. 318-320, 1935.

71. B. Y. Wang, X. Xiong, and A. N. Osiptsov, "Two-way coupling model for shock-induced laminar boundary-layer flows of a dusty gas," *Acta Mechanica Sinica,* vol. 21, pp. 557-563, Dec 2005.

72. R. Mei, "An approximate expression for the shear lift force on a spherical particle at finite Reynolds number," *International Journal of Multiphase Flow,* vol. 18, pp. 145-147, Jan 1992.

73. Q. Z. Wang, K. D. Squires, and O. Simonin, "Large eddy simulation of turbulent gas-solid flows in a vertical channel and evaluation of second-order models," *International Journal of Heat and Fluid Flow,* vol. 19, pp. 505-511, Oct 1998.

74. B. Kuan and M. P. Schwarz, "Numerical prediction of dilute particulate flow in horizontal and vertical ducts," in *Third international conference on CFD in the minerals and process industries*, Melbourne, Australia, 2003, pp. 10-12.

75. B. Y. Wang and A. N. Osiptsov, "Near-wall boundary layer behind a shock wave in a dusty gas," *Fluid dynamics,* vol. 34, pp. 505-515, 1999.

76. J. L. M. Poiseuille, "Recherches sur les Causes du Mouvement du Sang Dans les Vaisseaux Capillaires," *Annales Des Sciences Naturelles,* vol. 5, p. 111, 1836.

77. G. Segre and A. Silberberg, "Behavior of macroscopic rigid spheres in Poiseuille flow Part 2. Experimental results and interpretation," *Journal of Fluid Mechanics,* vol. 14, pp. 136-157, 1962.

78. J. P. Matas, J. F. Morris, and E. Guazzelli, "Lateral forces on a sphere," *Oil & Gas Science and Technology-Revue De L Institut Francais Du Petrole,* vol. 59, pp. 59-70, Jan-Feb 2004.

79. D. R. Oliver, "Influence of particle rotation on radial migration in the Poiseuille flow of migrations," *Nature Materials,* vol. 194, pp. 1269-1271, 1962.

80. A. Lutfurakhmanov, "Fluid Dynamics of Material Micro-Deposition: Capillary-Based Droplet Deposition and Aerosol-Based Direct-Write," Doctor of Philosophy, Mechanical Engineering and Applied Mechanics, North Dakota State University, Fargo, 2012.

81. D. S. Dandy and H. A. Dwyer, "A sphere in shear flow at finite Reynolds number: effect of shear on particle lift, drag, and heat transfer," *Journal of Fluid Mechanics,* vol. 216, pp. 381-410, Jul 1990.

82. I. S. Akhatov, J. M. Hoey, O. F. Swenson, and D. L. Schulz, "Aerosol focusing in micro-capillaries: Theory and experiment," *Journal of Aerosol Science,* vol. 39, pp. 691-709, Aug 2008.

83. J. B. McLaughlin, "Inertal migration of a small sphere in linear shear flows," *Journal of Fluid Mechanics,* vol. 224, pp. 261-274, Mar 1991.

84. G. N. Lipatov, T. I. Semenyuk, and S. A. Grinshpun, "Aerosol migration in laminar and transition flows," *Journal of Aerosol Science,* vol. 21, pp. S93-S96, 1990.

85. Y. S. Cheng and B. E. Dahneke, "Properties of continuum source particle beams.2. beams generated in capillary expansions," *Journal of Aerosol Science,* vol. 10, pp. 363-368, 1979.

86. S. Fuerstenau, A. Gomez, and J. F. Delamora, "Visualization of aerodynamically focused subsonic aerosol jets," *Journal of Aerosol Science,* vol. 25, pp. 165-173, Jan 1994.

87. G. W. Israel and Friedlan.Sk, "High-speed beams of small particles," *Journal of Colloid and Interface Science,* vol. 24, pp. 330-&, 1967.

88. G. W. Israël and J. S. Whang, *Dynamical Properties of Aerosol Beams*: Institute for Fluid Dynamics and Applied Mathematics, University of Maryland, 1971.

89. J. J. Stoffels, "A direct inlet for surface ionization mass spectrometry of airborne particles," *International Journal of Mass Spectrometry and Ion Processes,* vol. 40, pp. 223-234, 1981.

90. M. Sinha, C. Giffin, D. Norris, T. Estes, V. Vilker, and S. Friedlander, "Particle analysis by mass spectrometry," *Journal of Colloid and Interface Science,* vol. 87, pp. 140-153, 1982.

91. T. J. Estes, V. L. Vilker, and S. K. Friedlander, "Characteristics of a capillary-generated particle beam," *Journal of Colloid and Interface Science,* vol. 93, pp. 84-94, 1983.

92. O. Kievit, J. C. M. Marijnissen, P. J. T. Verheijen, and B. Scarlett, "Some improvements on the particle beam generator," *Journal of Aerosol Science,* vol. 21, pp. S685-S688, 1990.

93. W. Reents Jr, S. Downey, A. Emerson, A. Mujsce, A. Muller, D. Siconolfi, J. Sinclair, and A. Swanson, "Single particle characterization by time-of-flight mass spectrometry," *Aerosol Science and Technology,* vol. 23, pp. 263-270, 1995.

94. N. P. Rao, J. Navascues, and J. F. De la mora, "Aerodynamic focusing of particles in viscous jets," *Journal of Aerosol Science,* vol. 24, pp. 879-892, Oct 1993.

95. P. Liu, P. J. Ziemann, D. B. Kittelson, and P. H. McMurry, "Generating particle beams of controlled dimensions and divergence: 1. Theory of particle motion in

aerodynamic lenses and nozzle expansions," *Aerosol Science and Technology,* vol. 22, pp. 293-313, Apr 1995.

96. P. Liu, P. J. Ziemann, D. B. Kittelson, and P. H. McMurry, "Generating particle beams of controlled dimensions and divergence: 2. experimental evaluation of particle motion in aerodynamic lenses and nozzle expansions," *Aerosol Science and Technology,* vol. 22, pp. 314-324, Apr 1995.

97. F. Di Fonzo, A. Gidwani, M. H. Fan, D. Neumann, D. I. Iordanoglou, J. V. R. Heberlein, P. H. McMurry, S. L. Girshick, N. Tymiak, W. W. Gerberich, and N. P. Rao, "Focused nanoparticle-beam deposition of patterned microstructures," *Applied Physics Letters,* vol. 77, pp. 910-912, Aug 2000.

98. X. L. Wang and P. H. McMurry, "A design tool for aerodynamic lens systems," *Aerosol Science and Technology,* vol. 40, pp. 320-334, May 2006.

99. X. L. Wang, A. Gidwani, S. L. Girshick, and P. H. McMurry, "Aerodynamic focusing of nanoparticles: II. Numerical simulation of particle motion through aerodynamic lenses," *Aerosol Science and Technology,* vol. 39, pp. 624-636, Jul 2005.

100. M. J. Renn, B. H. King, and M. Essien, "Maskless deposition technology targets passive embedded components," in *Surface Mount Technology Association Pan Pacific Symposium*, 2002.

101. G. N. Lipatov, S. A. Grinshpun, and T. I. Semenyuk, "Properties of crosswise migration of particles in ducts and inner aerosol deposition," *Journal of Aerosol Science,* vol. 20, pp. 935-938, 1989.

102. C. C. Hwang, "Initial-stages of the interaction of a shock-wave with a dust deposit," *International Journal of Multiphase Flow,* vol. 12, pp. 655-666, Jul-Aug 1986.

103. M. S. H. El-Batsh, "Modeling particle deposition on gas turbine blade surfaces."

104. I. E. Barton, "Computation of particle tracks over a backward-facing step," *Journal of Aerosol Science,* vol. 26, pp. 887-901, Sep 1995.

105. G. K. Batchelor, *An introduction to fluid dynamics*: Cambridge university press, 2000.

106. M. J. Robinson, "Experimental Characterization of Aerosol Flow Through Microcapillaries," Master of Science, Mechanical Engineering and Applied Mechanics, North Dakota State University, Fargo, 2012.

107. Z. Mahmud, J. M. Hoey, A. Lutfurakhmanov, J. Daugs, O. F. Swenson, D. L. Schulz, and I. S. Akhatov, "Experimental characterization of aerosol flow through a micro-capillary," in *ASME Conference Proceedings*, Montreal, Canada, 2010, pp. 949-958.

108. M. J. Robinson, Z. Mahmud, O. F. Swenson, and J. M. Hoey, "Development of a Particle Sizing Algorithm for Sub-10 micron Paricles using Shadowgraphy," presented at the ASME International Mechanical Engineering Congress and Exposition, Houston, Texas, USA 2012.

109. J. Hoey, D. Thompson, M. Robinson, Z. Mahmud, O. Swenson, K. Pokhodnya, I. Akhatov, and D. Schulz, "CAB-DW for 5 μm trace-width deposition of solar cell metallization top-contacts," presented at the IEEE Photovoltaic Specialists Conference, Philadelphia, PA USA, 2009.

110. D. L. Schulz, J. M. Hoey, D. Thompson, O. F. Swenson, S. Han, J. Lovaasen, X. Dai, C. Braun, K. Keller, and I. S. Akhatov, "Collimated aerosol beam deposition: Sub-5-mu m resolution of printed actives and passives," *Ieee Transactions on Advanced Packaging,* vol. 33, pp. 421-427, May 2010.

111. J. M. Hoey, M. T. Reich, A. Halvorsen, D. Vaselaar, K. Braaten, M. Maassel, I. S. Akhatov, O. Ghandour, P. Drzaic, and D. L. Schulz, "Rapid prototyping RFID antennas using direct-write," *IEEE Transactions on Advanced Packaging,* vol. 32, pp. 809-815, Nov 2009.

112. A. Yarin, "Drop impact dynamics: splashing, spreading, receding, bouncing…," *Annu. Rev. Fluid Mech.,* vol. 38, pp. 159-192, 2006.

113. G. Cossali, A. Coghe, and M. Marengo, "The impact of a single drop on a wetted solid surface," *Experiments in fluids,* vol. 22, pp. 463-472, 1997.

114. R. Rioboo, M. Marengo, and C. Tropea, "Time evolution of liquid drop impact onto solid, dry surfaces," *Experiments in fluids,* vol. 33, pp. 112-124, Jul 2002.

115. S. Schiaffino and A. A. Sonin, "Molten droplet deposition and solidification at low Weber numbers," *Physics of Fluids,* vol. 9, pp. 3172-3187, Nov 1997.

116. A. Papyrin, V. Kosarev, S. Klinkov, A. Alkhimov, and F. Fomin, *Cold spray technology*: Elsevier Science, 2007.

117. R. G. Maev and V. Leshchynsky, *Introduction to low pressure gas dynamic spray: physics & technology*. Weinheim: Wiley-VCH, 2008.

118. A. Papyrin, "Cold spray technology," *Advanced Materials & Processes,* vol. 159, pp. 49-51, Sep 2001.

119. S. Bhattacharya, "Fluid Mechanics of Micro Cold Spray Direct Write Process," Doctor of Philosophy, Mechanical Engineering and Applied Mechanics, North Dakota State University, Fargo, 2012.

120. D. L. Schulz, C. J. Curtis, and D. S. Ginley, "Surface chemistry of copper nanoparticles and direct spray printing of hybrid particle/metallorganic inks," *Electrochemical and Solid State Letters,* vol. 4, pp. C58-C61, Aug 2001.

121. S. Han, X. Dai, P. Loy, J. Lovaasen, J. Huether, J. M. Hoey, A. Wagner, J. Sandstrom, D. Bunzow, O. F. Swenson, I. S. Akhatov, and D. L. Schulz, "Printed silicon as diode and FET materials - Preliminary results," *Journal of Non-Crystalline Solids,* vol. 354, pp. 2623-2626, May 2008.

122. M. Robinson, J. M. Hoey, D. Thompson, K. Mattson, G. Strommen, S. Ahmad, J. Lovaasen, I. Akhatov, A. Kallmeyer, and D. Schulz, "Cyclohexasilane (Si_6H_{12}) as a precursor to silicon based ring oscillators built with collimated aerosol beam-direct write (CAB-DW^{TM})," in *MRS Spring Meeting*, San Francisco, CA, 2009.

123. J. M. Hoey, J. Fink, M. Page, Q. Wang, I. S. Akhatov, and D. L. Schulz, "Collimated aerosol beam-direct write for solar cell metallization layer," in *MRS Spring Meeting*, San Francisco, CA USA, 2010, p. C9.3.

124. J. Fink, "Fine Line Metallization of Silicon Heterojunction Solar Cells Via Collimated Aerosol Beam Direct Write," Master of Science, Mechanical Engineering, North Dakota State University, Fargo, 2012.

125. E. Centurioni, D. Iencinella, R. Rizzoli, and F. Zignani, "Silicon heterojunction solar cell: A new buffer layer concept with low-temperature epitaxial silicon," *Ieee Transactions on Electron Devices,* vol. 51, pp. 1818-1824, Nov 2004.

126. J. Fink, J. M. Hoey, and D. L. Schulz, "Fine line metallization of silicon solar cells via collimated aerosol beam direct write," presented at the ASME International Mechanical Engineering Congress and Exposition, Houston, Texas, USA, 2012.

APPENDIX. MATLAB BEAM WIDTH CODE

```
clc;
clear all;
close all;
d1=1;%starting distance from nozzle
d2=10;%ending distance from nozzle
ds=1;%step distance
da=0.25;%actual distance i.e. not 1 mm but 1.25 mm
nmax=100;%number of images in each folder
mag=0.426821; % [micron/pixel]
mid=500;%this is the pixel point taken for measurements (500 is default)
cdir=(pwd);%cdir is the current directory of the file
mm=' mm';%this is the designator for the folders i.e. 1mm, 2mm etc.
for dn=1:(1+(d2-d1)/ds)
clear number avewidth stdev centerrange
dns=num2str(d1+dn-1);
slsh='\';
ndir=strcat(cdir,slsh,dns,mm);
cd(ndir);%changes current directory to find the other files
    tiffiles = dir('*.tif');
    numfiles = length(tiffiles);
    mydata=cell(1,numfiles);
    for n=1:nmax %choose how many images you would like to calculate
    I=imread(tiffiles(n).name); %read image
clear f g memory
f=double(I);
[xx,yy]=size(f);
for x=1:xx;
   f(x,:)=f(x,:)-mean(min(f(x,(yy-10):yy-10)));
    f(x,:)=f(x,:)./max(f(x,:));
end
wn=1;
clear width_hm width_e width_e2
width_hm=0;
width_e=0;
width_e2=0;
for Wnumber=[.5 1/exp(1) 1/exp(1)^2];%this is the linewidth function value
clear width1 width2 width3
width1=0;
width2=0;
for t=1:yy;
    g(t)=mean(f((mid-10):(mid+10),t));
end
g=g./max(g);
for x=1:length(g);
```

```
        if g(x)<(Wnumber)
            g(x)=0;
        end
    end
for x=1:1376;
    if g(x)>0;
        width1=x;
    end
end

for x=xx-((0:xx)-1);
    if g(x)>0;
        width2=x;
    end
end
if width2>0 && width1>0%this if statement is in case linewidth not computed
width3=width1-width2;
width(n,wn)=mean(width3)*mag;
center(n,wn)=(width1+width2)/2*mag;
else
width(n,wn)=0;
center(n,wn)=1000;
end
wn=wn+1;
end
% hh=figure('Position',[10 15 800 500]);
% iptsetpref('ImshowBorder','tight');
% imshow(f);hold on
% plot(width1,500, 'rx', 'MarkerSize', 10);
% plot(width2,500, 'rx', 'MarkerSize', 10);
display([(d1+da+dn-1) n])
    end
    %this section find the center of the beam then removed images which
    %are too far away from the center i.e. calculated incorrectly
center=center-center(1,1);
    j=1;
for i=1:n
        if abs(center(i,1))<=10*mag
    width_hm(j)=width(i,1);
    j=j+1;
        end
end
width_hm=transpose(width_hm);

    j=1;
for i=1:n
```

```
        if abs(center(i,2))<=10*mag
    width_e(j)=width(i,2);
    j=j+1;
        end
end
width_e=transpose(width_e);

    j=1;
for i=1:n
        if abs(center(i,3))<=10*mag
    width_e2(j)=width(i,3);
    j=j+1;
        end
end
width_e2=transpose(width_e2);
avewidth=[mean(width_hm) mean(width_e) mean(width_e2)];
stdev=[std(width_hm) std(width_e) std(width_e2)];
number=[length(width_hm) length(width_e) length(width_e2)];
centerrange=range(center);
clear width_hm width_e width_e2 center
output=[number;avewidth;stdev;centerrange];
%output makes a table where first line is number of images
%the second line is the width measurement
%third line is the standard deviation
%fourth line is center range (deviation)
output2(dn,:)=[(d1+da+dn-1) output(2,:) output(3,:) output(4,:)];
%output2 gives results 1) distance from nozzle 2) FWHM width 3) 1/e width
%4) 1/e^2 width 5) FWHM std. dev. 6) 1/e std. dev. 7) 1/e^2 std. dev.
%8) FWHM center 9)1/e center 10) 1/e^2 center
output3(dn,:)=[(d1+da+dn-1) output(1,:)];%number of images/calculation
end
cd(cdir);%changes directory back to the one where m file is located
load handel
sound(y,Fs)%plays music to let you know calculation is done
```